Space-Time Evolution in Relativistic Heavy-Ion Collisions

The work described in this thesis is the result of the common effort of the WA93 collaboration. The WA93 collaboration is an international group consisting of scientists from different institutes and universities. At the time of the experiments described in this thesis the collaboration consisted of the VECC Calcutta, GSI Darmstadt, University of Geneva, KVI Groningen, University of Jammu, University of Lund, Kurchatov Institute Moscow, University of Münster, Oak Ridge National Laboratory, University of Panjab, University of Rajasthan, University of Tennessee, University of Utrecht and Nuclear Institute Warsaw.

The work described in this thesis is part of the research programme of the "Stichting voor Fundamenteel Onderzoek der Materie" (FOM), which is financially supported by the "Stichting voor Nederlands Wetenschappelijk Onderzoek" (NWO).

ISBN 90 367 0549 5

Printed by: Stichting Drukkerij C. Regenboog

Rijksuniversiteit Groningen

Space-Time Evolution in Relativistic Heavy-Ion Collisions

Proefschrift

ter verkrijging van het doctoraat in de
Wiskunde en Natuurwetenschappen
aan de Rijksuniversiteit Groningen
op gezag van de
Rector Magnificus Dr F. van der Woude
in het openbaar te verdedigen op
vrijdag 1 december 1995
des namiddags te 4.00 uur

door

Sander Slegt

geboren op 27 juni 1969
te Rotterdam

1e Promotor: Prof. Dr H. Löhner
2e Promotor: Prof. Dr R.H. Siemssen

Contents

Chapter 1

Introduction

The curiosity of man, about his surroundings and his very existence, has caused him to explore nature. This eagerness to understand nature led the ancient Greeks to the concept of four basic elements, earth, water, fire and air, which was still used in the Middle Ages. After the Middle Ages there was a change of attitude towards practising science. No longer pure logic but also experiments were used to investigate nature. At the moment that the models failed to describe certain phenomena the search for other explanations began.

The same eagerness "to understand" has led to the search for a phase transition of nuclear matter to a gas of its constituent quarks and gluons. The main topic of this thesis will be the study of the space-time evolution of hot and dense nuclear matter created in ultrarelativistic heavy-ion reactions. Knowledge of the space-time evolution of the reaction zone provides insight into the dynamics of nuclear matter under extreme conditions and forms a necessary step for the observation of the phase transition.

1.1 History

It was only in 1911 that Rutherford discovered the core of the atom, which we know as the nucleus. A big step towards a better understanding of matter was made and the new field "Nuclear Physics" was born. In order to study smaller and smaller structures of nuclear matter an even higher resolving power of the analyzing apparatus was strongly needed. Were low energy probes like X-rays sufficient for the study of the shell structure of the atom, higher energy probes were required for the study of the structure of the nucleus. The continuing development of particle accelerators enabled

studies of length scales smaller than the size of the nucleus, which is of the order of several femtometer (1 fm = 10^{-15} m).

With the discovery of the neutron by Chadwick in 1932 it became apparent that the nucleus is built up of protons carrying positive electric charge and neutrons carrying net electric charge zero. More exotic particles like the muons and the π mesons were subsequently found. The observation of these particles was followed by the discovery of other related mesons and an even larger number of baryonic particles related to the protons and neutrons themselves. The systematics of the large number of these hadronic particles, baryons and mesons, raised the question if they are composed of more elementary constituents as was independently suggested by Gell-Mann and Zweig.

First positive evidence for the existence of quarks was found in the late sixties with the discovery of the internal structure of nucleons via deep-inelastic electron-nucleon scattering at the Stanford Linear Accelerator Center. The constituents of hadrons, in particular nucleons are in our current understanding described by quarks and leptons interacting via gluons, $W^{\pm}$- and Z-bosons and photons.

$$\begin{array}{cc} \text{quarks} & \text{leptons} \\ \begin{pmatrix} u & c & t \\ d & s & b \end{pmatrix} & \begin{pmatrix} e & \mu & \tau \\ \nu_e & \nu_\mu & \nu_\tau \end{pmatrix} \end{array} \tag{1.1}$$

There are six flavors of quarks of which the up (u), charm (c) and top (t) quarks have charge $+\frac{2}{3}$ and the down (d), strange (s) and bottom (b) quarks have charge $-\frac{1}{3}$. The quarks can be arranged in doublets or pairs, (u,d), (c,s) and (t,b), with almost equal masses within the doublet. Although the recent discovery of the top quark in 1995 at Fermilab [1, 2] awaits further confirmation there are strong theoretical arguments in favour of its existence. The leptons are arranged in doublets: the electron (e) and the electron-neutrino (ν_e), the muon (μ) and the muon-neutrino (ν_μ), and the tau (τ) and the tau-neutrino (ν_τ). The baryons consist of triplets of quarks whereas the mesons are formed by quark and anti-quark pairs. Before we continue on the theory related to the quark structure of the constituents of nuclear matter let us look thirty years back when this structure was not yet known.

R. Hagedorn (1965) and I. Pomeranchuk (1951) raised the question: "What will happen with nuclear matter in case of increased heating and compression ?" In the field of atomic physics the corresponding answer was known. Both heating and compression lead to phase transitions between the gaseous, liquid and solid states of "atomic matter". Hagedorn, with a

resonance gas model of hadronic matter, and Pomeranchuk, with a model of hadrons occupying a finite volume, came to the remarkable result of a limiting temperature of about 140 MeV, close to the pion mass, for hadronic matter [3]. Energy added in the form of heating or compression only leads to a further increase of the energy density. Hadronic matter could according to their results not exist above the limiting temperature.

During the early phase of the expansion of the universe, the primordial matter must have been very hot and dense. The average temperature of the universe today is 2.7 K. An extrapolation backward in time can be made leading to a temperature of 200 MeV (10^{12} K) at about 20 μs after the Big Bang. Could it be possible that with the expansion and cooling of the universe the primordial matter had made a phase transition to hadronic matter ? Knowledge about the space-time evolution of such a phase transition could contribute to an explanation for the observed large scale inhomogeneities in the universe, like clusters of galaxies. Inhomogeneities in the matter distribution of the universe have been found via very accurate temperature measurements of the background radiation in the universe by the COBE experiment [4].

With the discovery of the internal quark structure of the hadrons only twenty-seven years ago a new field theory: quantum chromodynamics (QCD), describing the strong interactions of quarks and gluons, was developed. This theory possesses remarkable properties both at small and large distances between the quarks and gluons. The quarks and gluons become unbound at small distances and a new phase of quarks and gluons, the quark-gluon plasma (QGP), is expected to develop.

1.2 Quantum Chromodynamics

From the deep-inelastic lepton scattering experiments it was known that quarks have spin $\frac{1}{2}$, i.e. they are fermions. Furthermore, triplets of three identical quarks like the Δ^{++} = (uuu) and the Ω^{-} = (sss) were observed which in the constituent quark model should have all the spins of the three quarks parallel and their relative motion in an s-state. The Pauli principle prohibits such a state unless there is an additional quantum number attached to the quarks. This quantum number was called colour charge. It can have three values which are conveniently called red, green and blue.

As quarks until now have not been observed as free colour-charged particles, the condition that bound quarks should form colour singlets has to be fulfilled. The symmetry group in the three colour dimensions SU(3) fulfills

such demands and it is the basis of the QCD theory. In the theory of QCD the quarks, carrying colour-charge, interact via the emission and absorption of a colour octet of field force carriers, the gluons. This is in analogy to the theory for electromagnetic interactions, quantum electrodynamics (QED). Here the electric charges interact via the emission and absorption of photons. Contrary to the photons in QED, which carry no electric charge, the gluons carry an octet of colour-charges and thus interact both with quarks and other gluons. This self-interaction of the gluons causes the long range force behaviour of the strong interaction. The quarks are bound by a force acting like a rubber band of gluons due to which quarks can not be separated unless another quark-anti-quark-pair is created conserving the colour singlet state of quarks.

1.3 Deconfinement

QCD exhibits two remarkable features at both large and small distances. These properties can be immediately deduced from the quark-quark running coupling constant α_s of QCD

$$\alpha_s(q^2) = \frac{3}{(33 - 2 \cdot N_f) \cdot \ln \frac{q^2}{\Lambda^2}} \tag{1.2}$$

where q is the momentum transfer, N_f the number of quark flavours, and Λ a dimensional scaling parameter.

At small momentum transfer and thus large length scales the coupling constant approaches large values. In this so-called non-perturbative region the behaviour of QCD is explained by colour confinement and implies that observable states of quarks have to appear in colour singlet states as colourless objects.

In case of an increased momentum transfer q^2 and thus small length scales we see that $\alpha_s(q^2) \to 0$. The scale parameter Λ has to be determined from experiments (deep-inelastic lepton scattering) and is determined to be $\Lambda_{QCD} \sim 200$ MeV [5, 6]. So for $q^2 \gg \Lambda^2_{QCD}$ there is weak coupling.

In atomic physics the effect of Debye charge screening is well-known. The Coulomb potential for two charges changes significantly when these charges are placed in an environment with a charge distribution containing both positive and negative charges, e.g. a plasma. The effective Coulomb potential is

$$V(r) = \frac{e}{4 \cdot \pi \cdot \epsilon_0} \cdot \frac{e^{-r/r_D}}{r} \tag{1.3}$$

where r is the distance between the electric charges e and r_D the Debye screening length. In case the Debye length is smaller than the distance between the charges the Coulomb potential is reduced significantly and the charges are no longer bound. Thus a charge insulator material may become a charge conductor.

Could an equivalent phenomenon also occur in QCD ? Then the question of Hagedorn and Pomeranchuk about the behaviour of hadronic matter at high temperatures and nuclear densities could be answered. A new phase of hadronic matter of free quarks and gluons would show up and the problem of the limiting temperature would be explained. Hadronic matter would no longer exist above this critical temperature.

Indeed QCD predicts the existence of a quark-gluon plasma (QGP) at extreme nuclear densities or at extremely high temperatures. Under such circumstances there is weak coupling. The hadronic matter being in the state of a colour insulator becomes under these conditions an ideal colour conducting plasma of quarks and gluons. The long range force becomes Debeye-screened due to collective effects analogous to those in an electromagnetic plasma.

1.4 Theoretical Description of the Quark-Gluon Plasma

The QCD theory predicts a short-lived finite volume of unbound quarks and gluons in case of heating and compression of nuclear matter in nucleus-nucleus collisions. What are the physical quantities, like energy density, pressure and temperature, related to the phase transition ?

No straight-forward answer has been given to this question until now. The QCD force possesses a strong long-range behaviour due to which calculations can not be performed in a perturbative way. Computer simulations of QCD on a 4-dimensional lattice aim to overcome this problem. Another approach is based on a phenomenological treatment of hadronic matter. The QGP is assumed to be an ideal gas of quarks and gluons. Statistical thermodynamics then predicts the properties of such a system. To describe the properties of the QGP the plasma is assumed to be both in thermal and chemical equilibrium. Thermal equilibrium may be obtained if the mean free path of a certain particle species is small with respect to the dimension of the plasma. The condition of chemical equilibrium is met if each species of particles is present according to its relative thermodynamic weight.

1.5 Lattice QCD

The thermodynamical properties of a system consisting of quarks and gluons can not be described analytically because of the strong long-range behaviour of the QCD running coupling constant. Therefore computer simulations are needed to evaluate the partition function. The fields describing the interactions between quarks and gluons are discretized on a lattice in space and time.

Depending on the initial conditions with respect to the number of quark flavours and their respective masses, these calculations predict a phase transition of either first-order, meaning a discontinuity in the energy density, or of second-order, meaning a smooth transition in the energy density with increasing temperature. The critical temperature is found in the range $140 \leq T_c \leq 220$ MeV and a critical energy density $1 \leq \epsilon_c \leq 2$ GeV/fm^3 is predicted [7, 8].

These calculations put heavy demands on computing power. An increase of the lattice slices dramatically increases the computing times. For infinite quark-masses, i.e. pure gauge QCD, a first-order phase transition is predicted. With the increase of the amount of slices in temperature and space the predictions from calculations between 1990 and 1994 for finite quark masses have been both in favour of a first- and second-order phase transition [9]. The latest result favours a second-order phase transition. However, the change of the energy density during the phase transition resembles closely the behaviour of a first-order transition. As long as these complicated calculations have not settled at a firm result, we assume, for simplicity and consistent with many theoretical publications discussing the reaction dynamics, a first-order phase transition.

1.6 The Bag Model

A simple phenomenological model describing the main features of a quark-gluon plasma is related to the MIT bag model [10, 11]. From the grand canonical partition function the energy density and pressure can be calculated in this model. Two extreme situations will be described. In the first situation the chemical potential, μ, will be zero. This means that the number of quarks equals the number of anti-quarks and thus a baryon-free quark-gluon plasma is established. The second situation describes at zero temperature and finite chemical potential a pure baryonic quark-gluon plasma.

Suppose the quark-gluon plasma is an ideal gas in which two quark flavours, u and d, and gluons are present. In this case the number of degrees of freedom for the quarks and the gluons are

- quarks: $N_q = 2(\text{spin}) \cdot 3(\text{colour}) \cdot 2(\text{flavour}) = 12$
- gluons: $N_g = 2(\text{spin}) \cdot 8(\text{colour}) = 16$

The energy density for the gluons is obtained making use of the thermal momentum distribution for bosons

$$\epsilon_g = \frac{N_g \cdot 4 \cdot \pi}{(2 \cdot \pi)^3} \cdot \int p^3 \cdot dp \cdot (e^{p/T} - 1)^{-1} = \frac{N_g \cdot \pi^2 \cdot T^4}{30} \tag{1.4}$$

where p is the momentum of the gluon and T the temperature of the plasma.

For the quarks the rest masses of the u- and d- quarks have been assumed to be zero to facilitate the calculation

$$\epsilon_q = \frac{N_q \cdot 4 \cdot \pi}{(2 \cdot \pi)^3} \cdot \int p^3 \cdot dp \cdot (e^{(p-\mu)/T} + 1)^{-1} \tag{1.5}$$

Here the thermal fermion distribution has been used. This integral can not be solved analytically. However, the energy density for the anti-quarks is given by

$$\epsilon_{\bar{q}} = \frac{N_{\bar{q}} \cdot 4 \cdot \pi}{(2 \cdot \pi)^3} \cdot \int p^3 \cdot dp \cdot (e^{(p+\mu)/T} + 1)^{-1} \tag{1.6}$$

Combining the energy density for quarks and anti-quarks their total energy density can easily be obtained

$$\epsilon_q + \epsilon_{\bar{q}} = N_q \cdot \left(\frac{7 \cdot \pi^2 \cdot T^4}{120} + \frac{\mu^2 \cdot T^2}{4} + \frac{\mu^4}{8 \cdot \pi^2} \right) \tag{1.7}$$

Assume the system is contained in a bag with an outside vacuum pressure B, the so-called bag constant. Taking into account the degrees of freedom for gluons N_g and quarks N_q, the total energy density of the QGP becomes [10]

$$\epsilon_{QGP} = \frac{37 \cdot \pi^2 \cdot T^4}{30} + 3 \cdot \mu^2 \cdot T^2 + \frac{3}{2 \cdot \pi^2} \cdot \mu^4 + B \tag{1.8}$$

In a similar way the pressure can be derived to be

$$P_{QGP} = \frac{37}{90} \cdot \pi^2 \cdot T^4 + \mu^2 \cdot T^2 + \frac{1}{2} \cdot \frac{\mu^4}{\pi^2} - B \tag{1.9}$$

In nucleus-nucleus collisions the quark-gluon phase is entered by both heating and compression of hadronic matter. The energy density and the pressure can be calculated for hot hadronic matter assuming it to be a hot pion gas. The energy density and the pressure of hadronic matter in the form of a pure pion gas can be easily calculated. With $N_\pi = 3$ isospin degrees of freedom of the pions, we obtain:

$$\epsilon_\pi = \frac{N_\pi}{30} \cdot \pi^2 \cdot T^4 \tag{1.10}$$

$$P_\pi = \frac{N_\pi}{90} \cdot \pi^2 \cdot T^4 \tag{1.11}$$

Then the critical temperature T_C at which the phase transition takes place can be derived. Demanding that the pressure of the hadronic phase equals that of the QGP phase at the critical temperature the following relation is obtained

$$T_c = \left(\frac{90 \cdot B}{34 \cdot \pi^2} \right)^{1/4} \tag{1.12}$$

This result applies for zero chemical potential, i.e. for a baryon free quark-gluon plasma. Applying a QCD scale parameter $\Lambda_{QCD} = B^{1/4} = 235$ MeV [7, 10], the critical temperature will be $T_c \approx 170$ MeV. The critical energy density for the quark-gluon plasma is $\epsilon_c \approx 1.7$ GeV/fm^3.

In the situation of a baryonic quark-gluon plasma at zero temperature, analogously to the above, the number density, energy density and pressure can be derived. The Fermi-momentum μ_q at which the pressure of the quark-gluon plasma equals the bag pressure is [10]

$$\mu_q = \left(\frac{24 \cdot \pi^2 \cdot B}{N_q} \right)^{1/4} \tag{1.13}$$

Furthermore, the number density can be derived to be

$$n_q = \frac{N_q \cdot \mu_q^3}{6 \cdot \pi^2} \tag{1.14}$$

which leads to the critical number density for a quark-gluon plasma with a high baryon content of $n_B = 0.72/\text{fm}^3$. This number density should be compared to the nucleon-number density $n_0 = 0.17/\text{fm}^3$ in normal nuclear matter. When the baryon-number density exceeds this nucleon density by a factor of 5 a phase transition to the quark-gluon plasma appears inevitable.

1.7 Experimental Search for the Quark-Gluon Plasma

All our universe is "a result" of the Big Bang. The stars and galaxies in the universe can be observed even with the naked eye. However, (fortunately) the early phases of such a large scale "experiment" can not be repeated on earth.

Nevertheless, with the advent of QCD theory and with its first application to the thermodynamics of strong interactions the quest arose to create hot and dense nuclear matter in small scale systems in the laboratory. A necessary condition is that the created system would be large and long lived enough to study the thermodynamic features of the quark-gluon plasma.

Heavy-ion reactions at ultra-relativistic energies of 10-100 A·GeV appeared to be a suitable tool. In these reactions hot and dense nuclear matter with a volume of 10-1000 fm^3 is created. With the development of heavy-ion injectors to existing high-energy proton accelerators, the Alternating Gradient Synchrotron (AGS) at Brookhaven National Laboratory (BNL) and the Super Proton Synchrotron (SPS) at the Centre Européen pour la Recherche Nucléaire (CERN), the appropriate facilities for ultra-relativistic heavy-ion beams became available in 1986.

With the new accelerators the phase diagram of nuclear matter could be explored in the region where the phase transition to the quark-gluon plasma is expected. In figure 1.1, a sketch of this diagram is shown.

The estimated values of the critical temperature and baryon density originate from the QCD-lattice and phenomenological calculations. The critical energy density of 2 GeV/fm^3 is to be compared to the energy density of ≈ 0.15 GeV/fm^3 for nuclear matter in the ground state and ≈ 0.5 GeV/fm^3 inside a single nucleon. Schematically, the region explored by heavy-ion reactions is shown. Also the transition of the early universe at high temperature and relatively low density and the transition at low temperature and high density, possibly reached in neutron stars, are depicted.

A first round of experiments, with a relatively light-ion beam from the AGS, i.e. silicon beam at 14.6 GeV per nucleon (or A·GeV, A = mass number of the projectile nucleus), and 60-200 A·GeV oxygen and sulphur beams at the SPS, took place during the period 1986-1990. A large stopping of the initial reaction partners in the nucleus-nucleus collisions was observed for these experiments. This proved the possibility of creating hot and dense nuclear matter.

In the period 1990-1993 experiments were done with 14.6 A·GeV gold

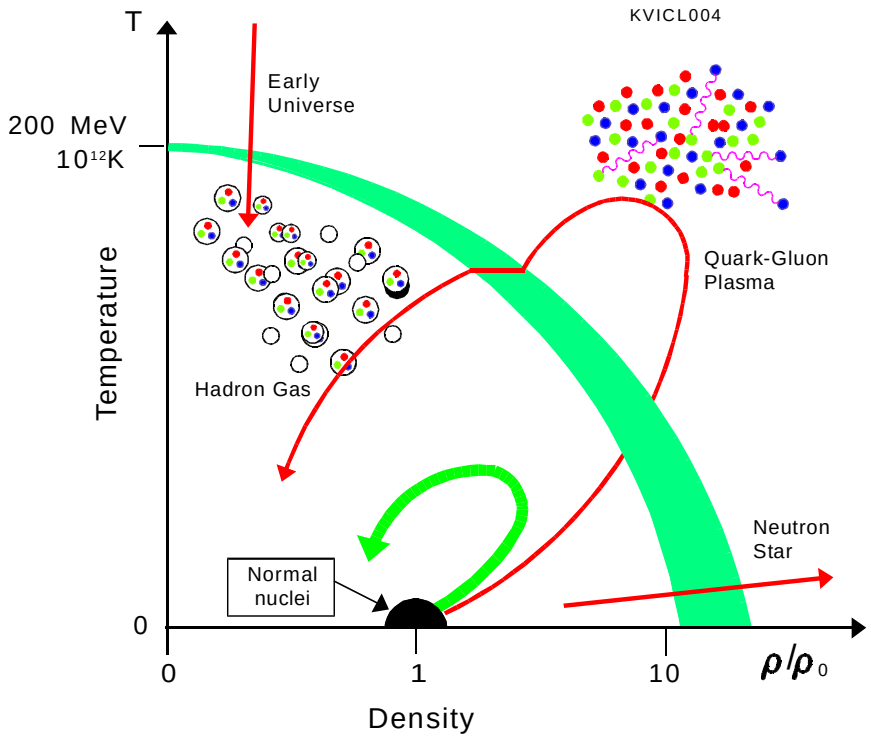

Figure 1.1: *Phase diagram for nuclear matter showing temperature and baryon density relative to normal nuclear matter.*

beams at the AGS and 200 A·GeV sulphur beams at the SPS. In this thesis results are presented from the analysis of 200 A·GeV S+Au reaction. The data were taken in 1992 in the WA93 experiment at CERN. In 1994-1995 the WA93 upgrade, WA98, measured Pb+Pb reactions using the 160 A·GeV lead beam. These data have partly been analysed recently.

In the near future collider experiments, using the Relativistic Heavy-Ion Collider (RHIC) at BNL (2000) and the Large Hadron Collider (LHC) at CERN (2008), will take place. The center of mass (CMS) energy of the reactions, currently $\sqrt{s} = 20$ GeV at CERN, will increase by a factor of 100. See for an overview of these experiments table 1.1. Here, ϵ_i is the expected initial energy density, $\frac{dN}{dY}_{max}$ is the expected number of produced particles at mid-rapidity, section 2.1, and T_i is the expected initial temperature.

The maximum achieved energy density for the current experiments is estimated to be around the calculated critical energy density of $\epsilon_c \approx 2$

Table 1.1: *Parameters and conditions in heavy-ion experiments.*

Start	Machine	Beam	$\sqrt{s}$ $[GeV]$	$\frac{dN}{dY}_{max}$	ϵ_i $[GeV/fm^3]$	T_i $[MeV]$
1986	AGS	^{28}Si	5	110	1.3	160
	SPS	^{32}S	20	220	2.4	190
1993	AGS	^{197}Au	4	390	1.2	160
1994	SPS	^{208}Pb	17	800	2.5	190
2000	RHIC	^{197}Au	200	1500	4.7	220
2008	LHC	^{208}Pb	6300	2500	7.8	250

GeV/fm^3 for the phase transition. The future colliders may well provide a clear observation of the deconfinement phenomenon as the maximum energy density will be several times higher than the achieved densities at the SPS facility so that even the average energy density in these collisions might surpass the critical density.

1.8 Outline of this Thesis

The results from the measurement of the space-time evolution of 200 A·GeV S+Au reactions are presented in this thesis. This work was done within the international WA93 collaboration. The aim of such research, the study of the QGP phase transition, was discussed in the previous sections.

Knowledge of the dynamics of the hot collision zone is essential for an understanding of the measured signals from the hot hadronic matter. The importance of knowing the space-time evolution is stressed in the discussion of the signals from both the quark-gluon plasma and hot hadronic matter in chapter 2. As we will see, none of the proposed signals can be understood properly without a profound knowledge of the space-time evolution of the particle emitting source.

The method of intensity interferometry was used to determine the size and the emission time of the particle emitting source. This method was originally applied by R. Hanbury Brown and R.Q. Twiss [12] to measure the size of stellar objects using photon-photon correlations. It was for the first time applied in the field of nuclear physics by G. Goldhaber et al. to measure the source size for anti-proton annihilation events using pion-pion correlations [13].

The interest in the use of intensity interferometry for ultra-relativistic

heavy-ion collisions arises from the fact that an estimate of the created energy density in the collision can only be obtained by the measurement of both the energy and the source volume. Furthermore, large source lifetimes are predicted in case of QGP formation, which can be indirectly deduced from the measured source sizes.

An extensive description of this method and the used parameterizations can be found in chapter 2.

Momenta of negatively charged particles were measured by the large acceptance spectrometer in the WA93 experimental setup. Groups from the University of Geneva, the University of Lund and the KVI Groningen were mainly involved with this charged-particle spectrometer. The measured momenta are used for the intensity interferometry. The spectrometer consisted of a large dipole magnet and four position-sensitive Multi-Step Avalanche Chambers, which were optically read out. In addition to the charged-particle spectrometer a large photon spectrometer measured the neutral mesons and photons. An overview of the WA93 setup is given in chapter 3. The main emphasis of this thesis lies on the spectrometer for negatively charged particles and a newly developed electronic readout method of the avalanche chambers, as the author was actively involved in the design, building, operation and data analysis of these chambers.

Properties of the charged-particle spectrometer and an outline of the data analysis are presented in chapter 4. The data analysis comprises the alignment of the tracking detectors, the determination of the hit positions of the tracks, the track reconstruction and the momentum reconstruction. Furthermore, knowledge is gained on detector limitations. Successively the two-track separation, the detector efficiencies, the geometrical acceptance, the background contributions and the momentum resolutions of the spectrometer will be discussed.

The physics results concerning the multiplicity spectra of negatively charged particles, the momentum spectra and the intensity interferometry are discussed in detail in chapter 5. This analysis was done for three classes of reactions which were selected according to the estimated impact parameter of the heavy-ion collision ("centrality"), named peripheral, semi-central, and central. Furthermore, the intensity interferometry was applied in multiple dimensions as a function of the transverse momenta of the correlated pion-pairs. Such an analysis probes the expansion of the source in different spatial directions with respect to the beam direction. From the initial conditions in the heavy-ion collisions mainly a longitudinal flow, i.e. in the beam direction, is expected.

In chapter 6 these results are compared with results from other exper-

iments and theoretical models. A theoretical model for one-dimensional longitudinal hydrodynamic expansion is presented. The measured data are compared to this model. From such a comparison the lifetime of the source can be deduced. A summary, with concluding remarks and prospects for further research, is presented in this chapter.

Chapter 2

The Signals of the QGP

The early universe must have passed through a regime of extreme temperature and density. During the expansion of the universe it cooled down. Hadronic matter was formed and with the further expansion and cooling of the system stars and galaxies were formed. The end of the life-cycle of a star can be a neutron star. In the inner core of a neutron star, a very high nuclear density at low temperature is reached. The quark-gluon plasma (QGP) is formed at either extreme densities or temperatures or both, figure 1.1. Such conditions are fulfilled by the early universe and they may also exist in the inner core of a neutron star.

On earth the only method to create and study very hot and dense nuclear matter is by nucleus-nucleus collisions, section 2.1. The nuclear matter in the collision zone is highly compressed and heated up. In this "participant region" of colliding nuclei where baryons interact frequently a QGP can be formed, which will, during the space-time evolution, go through several stages. These stages are in chronological order the creation of the QGP starting with pre-equilibrium processes and its formation by thermalization, the QGP, the mixed phase, the hadron gas and finally free hadrons. Each stage has specific characteristics concerning expected particle productions and lifetime. These signatures of the evolving system are of particular interest for the experimental physicist as they are the only measurable quantities to figure out what happened during the collision. The above-mentioned stages and their signatures will be described in the following sections with specific emphasis on the measurement of the space-time evolution in section 2.8.

2.1 Ultra-relativistic Heavy-Ion Collisions

Heavy-ions, like O, Si, S, Au and Pb, are presently accelerated to ultra-relativistic energies at facilities, such as the AGS (Alternating Gradient Synchrotron) at Brookhaven National Laboratory, New York, and the SPS (Super Proton Synchrotron) at CERN, Geneva, with maximum energies of tens and hundreds of GeV per nucleon, respectively.

In the experiments the heavy-ion collides with a nucleus, within the thin layer of, for example 0.1 mm Au or 1 mm S, target material. The amount of nuclear stopping, defined as the percentage of kinetic energy loss of the projectile nucleons in the nucleus-nucleus collision, is of crucial importance for the increase of energy density and particle density. Initial energy densities of 2.4 GeV/fm^3 are expected at the SPS energies [14]. This is to be compared to an energy density of 0.15 GeV/fm^3 for normal nuclear matter, and to 0.5 GeV/fm^3 inside a nucleon. In figure 2.1 the collision between target and projectile is shown schematically. The nucleons from both the target and the projectile nuclei taking part in the primary collisions are called "participants" whereas the non-interacting nucleons are called "spectators". In order to study and compare the phenomena of the collision the

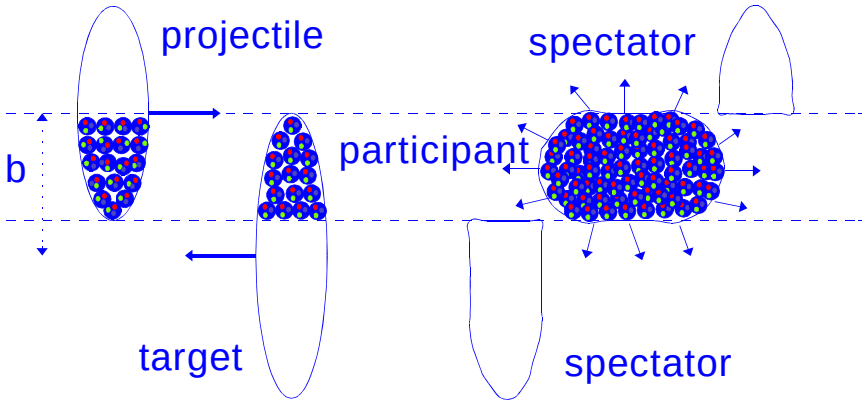

Figure 2.1: *Schematic picture of an ultra-relativistic collision. The situation before the collision is shown on the left; the created region of nuclear matter at high energy density after the collision is shown on the right.*

observables are presented in terms of Lorentz-invariant and additive variables. A commonly used variable for the velocity in the beam (longitudinal-

or z-) direction, is rapidity

$$Y = \frac{1}{2} \cdot \log \frac{E + P_z}{E - P_z} \tag{2.1}$$

where E is the total energy of the particle and P_z the momentum along the beam axis. A longitudinal Lorentz transformation corresponds to a shift in rapidity. Rapidity differences ΔY between particles and the shape of rapidity distributions are preserved. The target rapidity is Y = 0, whereas for 200 A·GeV the beam rapidity is Y $\approx$ 6. The center of the rapidity difference between target and projectile is referred to as "mid-rapidity", Y $\approx$ 3. Here, particles are emitted at an angle of 90° with respect to the nucleon-nucleon CMS system. A further useful variable is the transverse momentum P_T, perpendicular to the beam direction and thus Lorentz-invariant under longitudinal transformations. Also the transverse mass $m_T = \sqrt{P_T^2 + m^2}$, where m is the rest mass of the particle, is used.

Two extreme points of view can be taken for the amount of stopping of the participants in the collision zone, figure 2.2. These points of view are expressed in hydrodynamical models where energy, momentum, entropy and baryon number are conserved in the solution of relativistic hydrodynamic equations. The interacting nuclei are seen as fluids of nuclear matter which are extremely compressed via propagation of shock waves. Because of the dominant longitudinal expansion, due to the initial projectile direction, and slow transverse communication $v_{sound} \sim 0.3 \cdot c$, the equations are usually reduced to the one-dimensional case, assuming a constant transverse expansion.

Fermi-Landau Model:
This model assumes complete stopping of projectile and nuclear matter in the collision. In this case the participating nucleons of both target and projectile come to rest in the region of mid-rapidity. This scenario is called the Fermi-Landau model [15] and leads to particle production and a large energy density around mid-rapidity. The energy E_{FL} left for particle production is

$$E_{FL} = E_{CMS} - E_{rest} = \\ m_N \cdot \sqrt{A_p^2 + A_t^2 + 2 \cdot \gamma_p \cdot A_p \cdot A_t} - m_N \cdot (A_p + A_t) \tag{2.2}$$

where m_N is the rest mass of the nucleon, $\gamma_p = 1/\sqrt{1 - \beta_p^2}$ where $\beta_p = v_p/c$ is the velocity of the projectile, and A_p and A_t are the number of participating nucleons of projectile and target, respectively. The energy

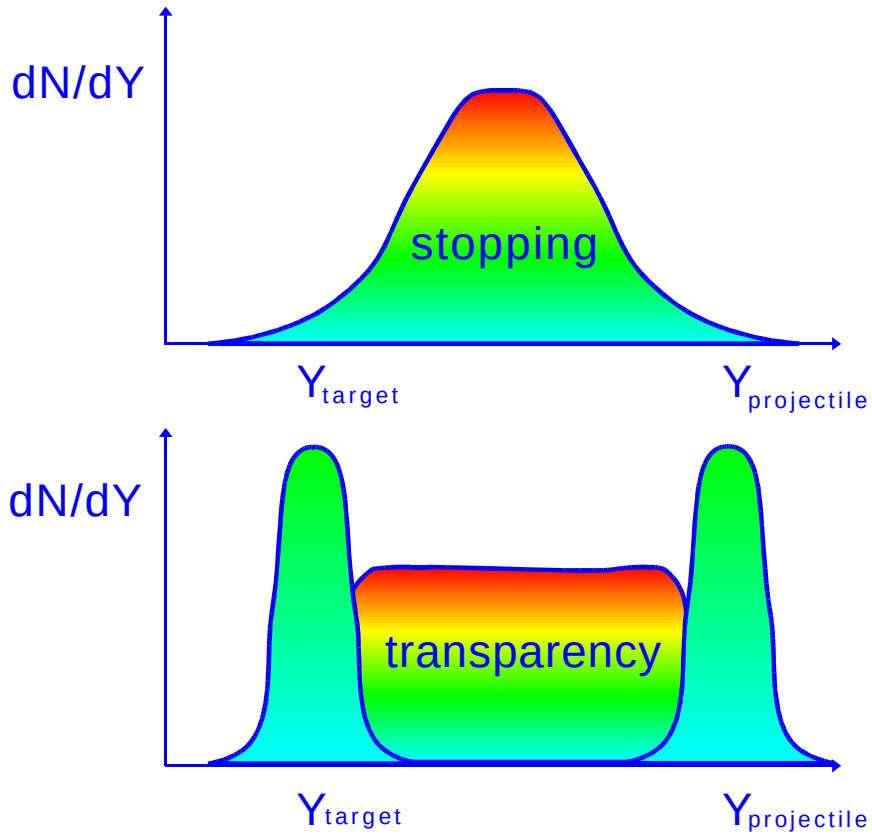

Figure 2.2: *Particle production for two extreme scenarios. The Fermi-Landau model shows complete stopping, upper figure, the Bjorken-McLerran model shows partial transparency, lower figure.*

density is calculated as

$$\epsilon = \frac{p \cdot E_{FL}}{V} \tag{2.3}$$

where p is the fraction of stopping and V is the volume of the region of nuclear matter at high energy density. Lack of knowledge about the amount of stopping and the space-time evolution of the system causes large uncertainties in the estimates of the created energy density.

Bjorken-McLerran Model:
The other scenario is the Bjorken-McLerran model [16]. The collision of the

two nuclei can be described by two thin disks at position $z = 0$. The nucleons in the overlap zone of the colliding nuclei may have several nucleon-nucleon collisions. Each nucleon-nucleon collision is accompanied by a large loss in energy of the collision. Several experiments, e.g. WA80 [17], have observed large stopping of 2 to 4 units in rapidity. However at very high energies, above 100 A·GeV, the nucleons can still have enough momentum to proceed forward and move away from the collision zone. This effect is known as transparency. The energy lost by the nucleons is deposited around $z = 0$. The matter created in this collision zone has a very high energy density and small net baryon content. Until now it is unknown whether the particles which carry the deposited energy will be quarks, gluons or hadrons. The formation time τ_0 at which these particles are formed and equilibrated due to rescattering is an unknown quantity and was estimated by Bjorken at $\tau_0 = 1/\Lambda_{QCD} \sim 1$ fm/c as this process concerns strong interactions.

The initial energy density of a matter element is defined in the frame in which the matter element is at rest, Y = 0. The two nuclei meet at z = 0, where in the center-of-mass frame the matter is at rest. The region of creation of particles is assumed to be homogeneous in rapidity for a longitudinal length Δz around z = 0. Observations at the CERN SPS of the charged particle multiplicity, dN_{ch}/dY = constant at mid-rapidity $Y = 3$, validate this assumption. Most of the emitted N particles will be pions, so that $N \approx \frac{3}{2} \cdot N_{charge}$. The energy E_{BM} contained in the cylinder of interacting matter can be estimated according to

$$E_{BM} = \frac{dE}{dY}|_{Y=0} \cdot \Delta Y = \frac{3}{2} \cdot \frac{dN_{charge}}{dY} \cdot < E_T >_P \cdot \Delta Y \qquad (2.4)$$

where the measured average energy per particle $< E_T >_P \sim$ 500 MeV [5] and $\Delta Y = \Delta z/(c \cdot \tau_0)$. For a central S+Au collision the estimated energy density, using for the sulphur radius $R_S = 1.15 \cdot A_S^{\frac{1}{3}}$, yields

$$\epsilon = \frac{3 \cdot \frac{dN_{charge}}{dY} \cdot < E_T >_P}{2 \cdot \pi \cdot \left(1.15 \cdot A_S^{\frac{1}{3}}\right)^2 \cdot c \cdot \tau_0} \qquad (2.5)$$

The variables used to study the degree of stopping are the total measured transverse energy E_T, section 3.4, and the forward energy E_F, section 3.3. For central 200 A·GeV S+Au collisions an $E_F \sim 1$ TeV was measured [17]. Here, 84 % of the total beam energy was converted into particle production around mid-rapidity. In the Fermi-Landau model [15] the calculated energy densities for beam energies of 10 GeV to 200 GeV per nucleon are in the

region $0.85 < \epsilon < 8.1$ GeV/fm^3. The large uncertainty in these calculations is due to a lack of knowledge about the size of the reaction volume.

2.2 Evolution from Quark Matter to Hadronic Matter

Under the assumption that thermal equilibrium is attained within the formation time τ_0, the time dependence of the temperature can be estimated in a hydrodynamical model. A graph of this evolution is shown in figure 2.3. After a certain initial equilibration time $\tau_i \sim \tau_0$ the quark-gluon plasma is in thermal equilibrium at an initial temperature T_i. The basic idea is that the expansion is very likely to be adiabatic, which means no dissipation will occur during the expansion. Therefore isentropic expansion of the fluid is presumed up to the critical temperature T_c. We assume the expansion to be still adiabatic, i.e. no dissipation will occur due to the transition. Then the temperature in the mixed phase remains constant in an isothermic expansion, and the latent heat is absorbed in the conversion of the degrees of freedom of the quarks and gluons into hadrons with their respective degrees of freedom. At the time τ_h the hadronization is completed and the hadron gas starts to cool down under isentropic expansion up to the time τ_f where the density of the system is low enough for the hadrons to escape. The hadrons freeze out which means they have no more interactions. As mentioned earlier, the variables of interest are the energy density $\epsilon(\tau, Y)$, the pressure $p(\tau, Y)$, the temperature $T(\tau, Y)$ and the entropy density $s(\tau, Y)$, where the proper time $\tau = \sqrt{t^2 - z^2}$ is Lorentz invariant. The energy-momentum tensor is given by

$$T_{\mu\nu} = (\epsilon + p) \cdot u_\mu \cdot u_\nu - g_{\mu\nu} \cdot p \tag{2.6}$$

where u_μ is the four velocity and $g_{\mu\nu}$ is the metric tensor. Under the condition of conservation of energy and momentum, neglecting viscosity and heat conduction, the equation of motion is governed by the equation for perfect fluid dynamics

$$\frac{\delta T_{\mu\nu}}{\delta x_\mu} = 0 \tag{2.7}$$

Assuming longitudinal expansion only, independent of rapidity, the time dependence of the energy density is [8]

$$\frac{d\epsilon}{d\tau} = \frac{-(\epsilon + p)}{\tau} \tag{2.8}$$

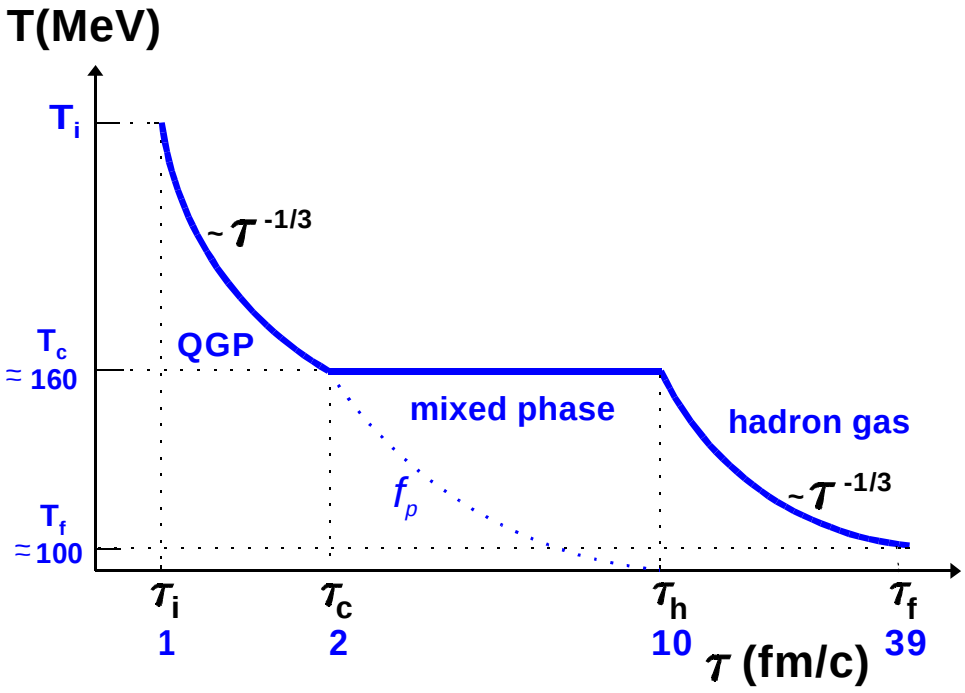

Figure 2.3: *Temperature versus time evolution of the QGP under the assumption of isentropic and isothermic hydrodynamic expansion.*

The equation of state of the plasma can be described by $p = c_s^2 \cdot \epsilon$ if p and ϵ are up to a factor the same function of the temperature T and the quark chemical potential μ. Here $c_s = v_s/c$ with v_s the velocity of sound in the plasma [10]. For an ideal relativistic fluid consisting of massless quarks and gluons one finds $c_s^2 = \frac{1}{3}$. Imposing the initial boundary condition $\epsilon(\tau_i)$ at time τ_i we obtain

$$\epsilon(\tau) = \epsilon(\tau_i) \cdot \left(\frac{\tau_i}{\tau}\right)^{c_s^2+1} \tag{2.9}$$

From now on an ideal relativistic fluid is assumed. Conservation of the total entropy S for a certain region in rapidity yields

$$\frac{dS}{dY} = s(\tau) \cdot dx_T \cdot \tau = const. \tag{2.10}$$

with entropy density $s(\tau)$ and the transverse size dx_T of the expanding cylinder given by the area $\pi \cdot R_A^2$ of the projectile nucleus A. Using the

equation of state for an ideal gas $s \sim T^3$ also $T^3 \cdot \tau = const.$. From this relation the time dependence of the temperature can be derived

$$T(\tau) = T(\tau_i) \cdot \left(\frac{\tau_i}{\tau}\right)^{\frac{1}{3}} \tag{2.11}$$

This equation allows to express the critical time τ_c in terms of initial temperature and the critical temperature

$$\tau_c = \tau_i \cdot \left(\frac{T_i}{T_c}\right)^3 \tag{2.12}$$

During the mixed phase the degrees of freedom of the QGP have to convert to those of the hadron gas under the condition of constant temperature. As the entropy density is $s = dS/dV = (\epsilon + p)/T$, the time dependence of energy density and pressure yields the ratio of the entropy densities

$$\frac{s(\tau)}{s(\tau_c)} = \frac{\epsilon(\tau) + p(\tau)}{T_c} \cdot \frac{T_c}{\epsilon(\tau_c) + p(\tau_c)} = \left(\frac{\tau_c}{\tau}\right)^{\frac{4}{3}} \tag{2.13}$$

The fraction of nuclear matter in the quark-gluon plasma phase is defined by a function $f(\tau)$. Using the above equation and the knowledge about the degrees of freedom in the QGP and hadron gas phase

$$s(\tau) \sim N_{dof}(QGP) \cdot f(\tau) + N_{dof}(hadron) \cdot (1 - f(\tau)) \tag{2.14}$$

the time dependence of the fraction of matter in the quark-gluon plasma phase yields

$$f(\tau) = \frac{1}{r-1} \cdot \left(r \cdot \left(\frac{\tau_c}{\tau}\right)^{\frac{4}{3}} - 1\right) \tag{2.15}$$

where $r = \frac{N_{dof}(QGP)}{N_{dof}(hadron)}$ with N_{dof} the degrees of freedom in the respective phases. Under the most likely assumption of a QGP dominated by light up and down quarks and gluons and a hadron phase with π, η, ρ, and ω mesons, we find $r = \frac{37}{4.6}$. The relation between the critical time and the time of completed hadronization becomes $\tau_h = r^{3/4} \cdot \tau_c$.

Analogous to the isentropic expansion of the QGP the expansion of the hadron gas can be treated with a freeze-out temperature T_f. Using $T_i = 200$ MeV, $\tau_i = 1$ fm/c, $T_c = 160$ MeV and $T_f = 100$ MeV [18] an estimate for the time scale of the expansion can be given. These numbers lead to $\tau_c = 2$ fm/c, $\tau_h = 10$ fm/c and $\tau_f = 39$ fm/c. In case of a higher freeze-out temperature $T_f = 140$ MeV [19] we obtain $\tau_f = 15$ fm/c.

Alternatively, if the hot hadron gas would exist at an initial time $\tau_i = 1$ fm/c with an initial temperature $T_i = 200$ MeV we obtain for a freeze-out temperature $T_f = 100$ MeV a freeze-out time $\tau_f = 8$ fm/c. For $T_f = 140$ MeV we obtain $\tau_f = 3$ fm/c.

Thus considerable differences are expected for the freeze-out time dependent on the initial conditions.

2.3 Pre-Equilibrium and Thermalization

The multiple scattering of the participants will lead to the production of more interacting constituents. Thus there will be an entropy increase and local memory loss. The basic question now is whether the produced system lived long enough to be both in thermal and chemical equilibrium. The former means, that the momenta of the particles are distributed according to a Boltzmann distribution with a certain temperature T, the latter, that the abundance of the different constituent species are given by their relative thermodynamic weight; see section 2.7.

A good test of the pre-equilibrium stage is the measurement of heavy-mass dileptons (M = 5-10 GeV). According to the Heisenberg uncertainty relation their lifetime is short $\Delta\tau = \frac{1}{M} = 0.02 - 0.04\,\mathrm{fm/c}$, so that these particles will probe the pre-equilibrium stage. The interactions of the dilepton pair are based electromagnetic of nature only and will thus not be reduced by the subsequent development of the created system. An enhanced production of dileptons may be caused by hard $q\bar{q}$ scattering.

Another good probe which will also be discussed later as a signature of the QGP is strangeness enhancement; section 2.5. From ratios of measured strange particle yields for p+p and p+A collisions, an enhancement of strangeness and anti-strangeness for nuclear collisions is observed. This indicates an increasing amount of rescattering for the participants and secondaries, which is a prerequisite for thermalization.

Statements on thermal equilibrium need some caution. The reason is that the transverse momentum distributions already follow Boltzmann like behaviour $\sim e^{(-m_T/T)}$, where $m_T = \sqrt{P_T^2 + m^2}$, in p+p collisions. This fact prohibits the straightforward interpretation of an exponential P_T spectrum in nuclear collisions as evidence for thermalization in dense hot matter.

2.4 Direct Photons

The only way to get direct signatures from the QGP is to measure weakly (electromagnetically) interacting probes which have already decoupled from the hot phase of matter. Direct photons and lepton pairs (virtual photons) are such observables [20]. They should emerge as thermal radiation from the heated matter without being altered by final-state processes. In heavy-ion collisions there are various sources for photon production. Hard parton scattering produces high-energy direct photons from hadron-hadron collisions at large momentum transfer . The following elementary processes are involved:

1. QCD annihilation: $q\bar{q} \rightarrow g\gamma$

2. QCD Compton scattering: $qg \rightarrow q\gamma$

The above processes are well understood and can be evaluated by perturbative QCD. One can calculate the invariant inclusive cross-section for hard photons (hard parton scattering) according to

$$E_\gamma \frac{d^3\sigma}{d^3P_\gamma}(A + B \rightarrow \gamma + X) = \int \frac{dx_a}{x_a} \cdot \frac{dx_b}{x_b} \cdot F(a, A, x_a) \cdot F(b, B, x_b) \cdot E_\gamma \frac{d^3\tilde{\sigma}}{d^3P_\gamma} \tag{2.16}$$

where $x_a = P_a/P_A$ and $x_b = P_b/P_B$ are the Feynman momentum fractions of partons a and b, F the structure functions of the scattering hadrons, E_γ the photon energy and $\frac{d^3\tilde{\sigma}}{d^3P_\gamma}$ the cross-section for the above-mentioned elementary processes.

In case the structure functions are known, the photon spectra can be determined. However, the structure functions cannot be calculated theoretically but they are parameterized instead according to deep-inelastic scattering results.

In case of a QGP the elementary processes for thermal photon production are basically the same as those previously mentioned. But no longer can one use the structure functions as was done in the hard-scattering regime. Instead, we have a gas consisting of quarks and gluons. These partons are assumed to be in both thermal and chemical equilibrium. The QCD structure functions have therefore to be replaced by thermal distributions with the chemical potential $\mu = 0$, assuming zero baryon number around mid-rapidity.

If one uses the thermal distribution functions f(p) for the partons the thermal rate R_γ is given by [20]

$$E_\gamma \frac{d^3R_\gamma}{d^3P_\gamma} = \frac{N}{2\cdot(2\cdot\pi)^4} \cdot \int \frac{f(P_1)\cdot d^3\vec{P}_1}{2\cdot E_1} \int \frac{f(P_2)\cdot d^3\vec{P}_2}{2\cdot E_2} \cdot$$
$$\int \frac{(1\pm f(P_3))\cdot d^3\vec{P}_3}{2\cdot E_3} \cdot \delta^4(P_1 + P_2 - P_3 - P_\gamma) \cdot |M_i|^2 \qquad (2.17)$$

The amplitudes $|M_i|^2$ are calculated from the Feynman graphs for the above-mentioned Compton and annihilation processes. The degeneracy factor N takes the number of degrees of freedom of the scattering particles into account, for example colour and spin. The term $((1 \pm f(P_3))$ describes effects of quantum statistics in the final state (+ for bosons and − for fermions).

However, the evaluation of the integration of the above equation is complicated by infrared divergences for small momentum transfer. This problem was in a first attempt bypassed by introducing an infrared cutoff at the current light-quark mass $m_q \approx 5$ MeV [21]. In order to eliminate this divergence correctly, many-body effects must be taken into account. Recently, the resummation method for finite-temperature perturbation theory was applied to real-photon production [22]. An analytic result for the thermal photon rate at temperature T can be obtained for the sum of annihilation and Compton contributions

$$E_\gamma \frac{d^3R_\gamma}{d^3P_\gamma} = C \cdot (\sum_{n_f} e_q^2) \frac{\alpha \cdot \alpha_s}{2 \cdot \pi^2} \cdot T^2 \cdot e^{-E_\gamma/T} \cdot (\kappa_1 + ln\frac{\kappa_2 \cdot E_\gamma}{\alpha_s \cdot T}) \qquad (2.18)$$

with C = 1, $\kappa_1 = 0$ and $\kappa_2 = 0.23$. Various approximations [23, 24, 25] have been used which lead to similar analytic dependences on E_γ and T but differ in the constants κ_1 and κ_2 and the absolute normalization C.

If nuclear collisions lead to the formation of hot hadronic matter, then photon production from the electromagnetic coupling of the interacting mesons, dominantly $\pi^\pm$, needs to be taken into account. Annihilation and compton processes were considered among which $\pi\pi \rightarrow \rho\gamma$ dominates at small photon energies and $\pi\rho \rightarrow \pi\gamma$, with higher available energy due to the ρ-mass at higher energies [22]. With thermal momentum-distribution functions at temperature T the hadronic collisions give rise to similar photon rates as expected from parton interactions at the same temperature. Thus a photon signal is expected even if the plasma phase has not been reached. However, since the hadronic-matter phase is expected to dominate at lower temperature than that of the quark-gluon plasma, the spectral shape of the photon signal needs to be analysed and one should separate the different contributions.

Therefore, in principle measuring the emission rate of photons from parton interactions may provide information on the temperature of the system

created in the heavy-ion collision. But until now we have neglected still a major part, namely photons from decays of neutral mesons abundantly produced in both the mixed and hadronic phase:

$$\begin{array}{lcl} \pi^0 & \rightarrow & \gamma\gamma\ (98.8\%) \\ \eta & \rightarrow & \gamma\gamma\ (38.8\%) \qquad \pi^0\pi^0\pi^0\ (31.9\%) \quad \pi^+\pi^-\pi^0\ (23.6\%) \\ \rho & \rightarrow & \pi^0\pi^0\ (100\%) \\ \omega & \rightarrow & \pi^+\pi^-\pi^0\ (88.8\%) \quad \pi^0\gamma\ (8.5\%) \end{array} \tag{2.19}$$

The decay of the lightest mesons (π^0 and η) dominates the photon production. These sources of photons tend to obscure the signal of interest, the direct thermal photons originating from the QGP.

The total number of produced photons emerges from the space-time integration over de production rates for the different phases [26]

$$E_\gamma \frac{d^3\sigma_\gamma}{d^3P_\gamma} = \int_{\tau_i}^{\tau_f} d\tau \cdot dy \cdot \tau \cdot \pi \cdot R_A^2 \cdot E_\gamma \frac{d^3R_\gamma(T(\tau))}{d^3P_\gamma} \tag{2.20}$$

where R_A is the radius of the projectile nucleus for the case of a central collision. Attempts to calculate the expected number of photons for different scenarios with and without a QGP have been made [18]. However, to draw unambiguous conclusions more knowledge on the space-time evolution is urgently needed.

The summed production yield of all photon processes discussed earlier has been calculated by integration of the space-time evolution for different initial temperatures ($230 < T_i < 330$ MeV). The direct γ/π^0 ratio varies as a function of the transverse momentum. It peaks slightly above P_T = 1 GeV/c here, a considerable yield of $\gamma/\pi^0 \approx 10 - 20$ % from thermal processes of quarks and gluons can be expected. Only via a very good π^0 and η reconstruction [27], see section 3.8, can the direct photons still be separated with a detection limit of $\gamma/\pi^0 \approx 0.05$.

Selections can be made on reaction events with a high ratio of measured photons, see section 3.9, to hadrons, see section 3.6. The photon spectra for such events can then be analysed in more detail according to the above-described method. In case of a low temperature (T $\ll$ 200 MeV) hadron gas no excessive photon production is expected. The ratio is then expected to be

$$\frac{N_\gamma}{N_{charge}} = \frac{N_\gamma(decay)}{N_{charge}} \approx 1 \tag{2.21}$$

since decay photons dominantly originate from $\pi^0 \rightarrow \gamma\gamma$ and $N_{\pi^0} = \frac{1}{2} \cdot (N_{\pi^+} + N_{\pi^-}) = \frac{1}{2} \cdot N_{charge}$, exploiting the isospin symmetry in non-exotic hadronic matter.

In case of either a QGP or a hot hadronic gas an additional number of photons $N_\gamma(thermal)$ are produced by Compton and annihilation processes so that this ratio should change to

$$\frac{N_\gamma}{N_{charge}} = \frac{N_\gamma(decay) + N_\gamma(thermal)}{N_{charge}} > 1 \qquad (2.22)$$

The analysis for the γ/π^0 ratio has been done in the WA80/93 collaboration for central O+Au reactions [17] yielding an upper limit for direct photons of $\gamma/\pi_0 < 0.15$ and for S+Au [27, 28] with an uncertainty of 6-8% and 8-15% for P_T bins below and above 2 GeV/c, respectively. A recent status report and a letter-draft on the re-analysis of the S+Au data [29, 30] predict even a further decrease of the above-quoted upper limit for direct photon production. The NA45-CERES collaboration [31, 32] measured an insignificant excess of $\gamma/\pi_0 = 0.08 \pm 0.11$. Due to the still large uncertainties as compared to the weak photon signal, in the results from the data analysis and the theoretical models, conclusive quantitative comparisons can not yet be made.

2.5 Strangeness Enhancement

Strange quarks s and $\bar{s}$ are thermally produced in equal abundance. Due to the initial conditions in the heavy-ion collision, non strange quarks will be more abundantly available than non strange anti-quarks. For the $\bar{s}$ quarks this opens the possibility to form the mesons $K^+ = u\bar{s}$, $K^0 = d\bar{s}$ and $\phi = s\bar{s}$, while for the s quarks the cross-section to form hyperons, like for example the $\Lambda = uds$, is larger. Of course, the creation of the Λ is due to the multiple particle interaction less likely than the K^+ and K^0 creation. The creation of K^- $(s\bar{u})$ and $\bar{K^0}$ $(s\bar{d})$ and $\bar{\Lambda}$ $(\bar{u}\bar{d}\bar{s})$ will be, due to the lack of anti-quarks, less likely than the K^+ and K^0 production. Thus an enhancement of K^+ and K^0 yields may be expected. The ratio of K^+/K^- yields for example should be larger than 1. A strong rapidity dependence, as the energy density is maximal at mid-rapidity, of these ratios (K^+/π^+,K^-/π^-, K^+/K^-) should reveal the thermal origin of strange quarks.

Strangeness enhancement can also be described within a hadron gas model by the rescattering process $\pi^+\pi^- \rightarrow K\bar{K}$, and lowered effective kaon masses [33] at high density. Both on the experimental and theoretical side still much work has to be done to clarify the situation.

Strange matter [34] is another signature of the QGP. The $\bar{s}$-quarks will be removed easily according to the above-described fusion processes in contrast to the s-quark. This might lead to an s-quark enriched lump of nuclear matter after hadronization. Recalling that the quark charges are $Q_s = -\frac{1}{3}$, $Q_u = +\frac{2}{3}$ and $Q_d = -\frac{1}{3}$, these lumps of heavy nuclear matter are expected to have large A and almost zero Z. Interesting cosmological questions arise concerning the stability of these lumps and their possible contribution to the dark matter in the universe.

2.6 J/Ψ Suppression

As already mentioned, after the QGP formation the system will expand and cool down by emitting baryons and mesons. It is expected that in the early pre-thermal stages of the collision, heavier quark-flavour mesons $c\bar{c}$ and $b\bar{b}$ can be created via dominantly gluon fusion and $q\bar{q}$ fusion [14, 35, 36]. The ground state for the $c\bar{c}$ meson is at $M_{J/\Psi} = 3.1$ GeV with excitations to $\Psi^{'} = 3.7$ GeV and $\chi_c = 3.5$ GeV. Whereas the $b\bar{b}$ meson ground state is $M_\Upsilon = 9.6$ GeV, with excitation to $\Upsilon^{'} = 10.0$ GeV and $\chi_b = 9.9$ GeV. A fraction of these heavy meson resonances decays, for example 12 % of the J/Ψ and 5 % of the Υ mesons, in dileptons. In the absence of a medium the binding potential for heavy mesons is given by

$$V(r) = \sigma \cdot r - \frac{\alpha}{r} \tag{2.23}$$

where σ denotes the string tension and r the separation between quark and antiquark; the term (α/r) describes the Coulomb part of the potential as well as transverse string vibrations [14]. In the QGP medium the presence of other colour charges will lead to a screening of the colour force between the heavy charmonium- and bottomium-quarks. The long-range Coulomb-like part of the potential V(r) for the heavy mesons will be modified to the short-range Yukawa potential whereas the string-tension part approaches a constant value

$$V(r, r_D) = \sigma \cdot r \left(\frac{1 - e^{-r/r_D}}{r/r_D} \right) - \frac{\alpha \cdot e^{-r/r_D}}{r} \tag{2.24}$$

When the Debye radius r_D, introduced by Debye to describe charge screening in solid-state physics, gets smaller than the effective radius r between the quark-antiquark pair, the meson will break up. In table 2.1 an overview of the masses, M, and the binding radii, r, for the respective heavy mesons

and the necessary energy densities to dissolve them, ϵ_d, is presented [14]. In a study of the invariant-mass spectrum of lepton pairs the comparison

Table 2.1: *Masses, binding radii and dissolving energy densities for the respective heavy mesons.*

State:	J/Ψ	Ψ'	χ_c	Υ	Υ'	χ_b
M (GeV)	3.1	3.7	3.5	9.6	10.0	9.9
r (fm)	0.22	0.44	0.35	0.12	0.25	0.20
ϵ_d (GeV/fm^3)	1.9	1.0	1.0	47.1	1.6	1.0

of p+p collisions, where one does not expect the formation of a QGP, with A+A collisions where one does expect a QGP, should reveal a difference in the production rate of J/Ψ mesons. The explanation is that due to colour screening the J/Ψ mesons will "melt" in the hot dense medium due to a deconfinement of the charmed quark pairs $c\bar{c}$. One has, however, to be aware of background processes like the $q\bar{q}$-fusion mechanism in hard collisions. This so-called "Drell-Yan" process produces a continuum below the J/Ψ invariant-mass peak in the dilepton mass spectrum. In case such a mechanism is identical for the non-QGP and QGP scenario one can safely normalize to it. This assumption relies on the $q\bar{q}$ momentum distribution to be identical in both cases.

According to the Feynman rules the cross-section for the Drell-Yan process follows $\sigma \sim M^{-4}$. The signal-to-background ratio should improve for the heaviest mesons and better probes are therefore Υ and Υ'.

The observed J/Ψ suppression [37] can also be explained by collective nuclear effects [35, 38]. There is the initial state suppression effect due to gluon shadowing, which is already present in p+A collisions. The gluon structure functions differ for larger A. The gluon shadowing in the A+A collisions is corrected for by applying measured correction terms in p+A collisions.

Furthermore one has to be aware that:

- J/Ψ mesons are formed in the very early phase of the collision.
- J/Ψ mesons will not be in thermal equilibrium with other mesons (for T = 200 MeV we obtain $e^{-\frac{M_{J/\Psi}}{T}} \approx 10^{-7}$). An extra production of $c\bar{c}$ pairs in the QGP can thus be excluded.

- The formation time for the process $c\bar{c} \rightarrow J/\Psi$ is smaller than 1 fm/c so these mesons are already present when hot matter appears.

During the hadronization phase charmed quarks may form D and $\bar{D}$ mesons. Another absorption effect may play a crucial role. The J/Ψ meson can get struck by constituent quarks and break up to form D and $\bar{D}$. The survival probabilities for the J/Ψ in the medium can be calculated from the mean free path $S \sim e^{-\frac{L}{\lambda}}$, L is the dimension of the system, $\lambda = \frac{1}{n_0 \cdot \sigma_{J/\Psi}}$ the mean free path where $\sigma_{J/\Psi}$ is the interaction cross-section and n_0 the particle density of the constituents. Integration over the time t_0 of thermalization up to freeze-out time t_f for the mainly longitudinally expanding system yields

$$S = e^{-n_0 \cdot t_o \int_{t_0}^{t_f} dt \cdot \sigma_{J/\Psi}(t)/t} \simeq e^{-n_0 \cdot t_0 \cdot \sigma_{J/\Psi} \cdot ln(t_f/t_0)} \tag{2.25}$$

Such calculations can for superdense hadronic matter reproduce the measured absorption. Again we see that knowledge on the space-time evolution of the expanding system is absolutely necessary. For a conclusive spectral analysis one needs J/Ψ, $\Psi^{'}$, χ_c, Υ, $\Upsilon^{'}$, χ_b production rates and measurements of the Drell-Yan continuum for p+p, p+A and A+B collisions together with measurements of the space-time evolution for the respective collisions.

2.7 Mixed Phase, Hadron Gas, Free Hadrons

While the hot and dense matter created in the collision expands the energy density and temperature will decrease as described in section 2.2. At the critical temperature the system enters a mixed phase of a QGP and hadron gas. The abundant degrees of freedom of the quarks and gluons in the QGP are transferred to the degrees of freedom of the created hadrons at a fixed temperature. An enhanced rapidity density $\frac{dN}{dY}$ of produced particles at mid-rapidity with a fixed average transverse momentum $< P_T >$ is expected as the energy density is proportional to $\frac{dN}{dY}$ and the temperature proportional to $< P_T >$, section 2.1. In case the critical energy density is exceeded the QGP regime is entered and the temperature expressed by $< P_T >$ will rise.

In the hadron gas phase the temperature will drop further until the mean free path of the hadrons exceeds the dynamical size of the system. The hadrons in this case see a transparent medium and will freeze out. In a simple way the size R_f of the system at the moment of freeze-out can be calculated by assuming the mean free path to be equal to the effective

radius of the expanding system, $\lambda = \frac{1}{n \cdot \sigma} = R_f$, with the particle density $n = \frac{dN}{dY} / (\frac{4 \cdot \pi}{3} \cdot R_f^3)$, yielding

$$R_f = \sqrt{\frac{3}{4 \cdot \pi} \cdot \frac{dN}{dY} \cdot \sigma} \tag{2.26}$$

The cross-section σ depends on both the temperature and the particle species [39]. Strange particles, which have a smaller cross-section with respect to non-strange particles, will freeze out at an earlier stage than non-strange particles $R_f^{strange} < R_f^{non-strange}$.

Another model assumes the particles to freeze out at a constant particle density $n = const.$. This approach leads to

$$R_f \sim \left(\frac{dN}{dY} \right)^{1/3} \tag{2.27}$$

Radii measured by various experiments seem to favour a constant freeze-out density [40, 41], see also section 6.3.

Summarizing the previous sections we notice that basically three different types of measurements are needed:

- Particle ratios, which give information on the chemical composition and equilibrium of the system.
- Momentum distributions of particles, which give information on the temperature and the amount of collective expansion of the system.
- Space-time evolution of the system, which gives information on the source dynamics and is a prerequisite for the understanding of the measurements on the particle ratios and momentum distributions.

The space-time evolution can be examined by studying the relative momentum correlations of identical particles. This analysis is of crucial importance as we have seen that most signals depend on the space-time evolution. In the next section an extensive description of the method and recent developments will be given.

2.8 Intensity Interferometry

A well-known aspect of waves, either mechanical, for example in a rope, or electromagnetic, for example in a cavity, is that they can interfere with each other resulting in a characteristic interference pattern. Such a pattern can be

observed by eye in the Young Interferometer. Here, one photon "interferes with itself" as the wave packets of the photon field may traverse both slits. The amplitudes for the different paths sum up and, using a coherent light source, the intensity pattern shows a regular static structure. The regular structure can only be observed in case of a coherent source as otherwise the pattern would continuously vary in space and time and the interference structure would be washed out.

In the measurements of stellar sizes a new type of interferometry based on the incoherence of the source was used for the first time by correlating the intensities of measured photons [12, 42]. Hanbury Brown and Twiss called it intensity interferometry or second-order interferometry. The HBT effect was later also applied in nuclear physics [13, 43] to measure the size of the reaction zone. The step from correlating identical bosons like photons to pions was made. The big difference between the astronomical application and the application in nuclear physics is that in the former situation one observes a large static object with a relatively small detector system whereas in the latter case one observes a small dynamic object with a relatively large detector system.

In this section the theory and application of intensity interferometry will be discussed. In the previous sections the importance of knowing the space-time structure of the interacting system has been explained. A lot of data has already been taken for several different colliding systems, p+p, p+A, A+B, and a variety of beam energies. Results from these experiments will be compared to the new results from S+Au reaction in the WA93 experiment in chapter 6.

2.8.1 Theory of Intensity Interferometry

The theoretical background of intensity interferometry is reported comprehensively in several review articles [8, 44, 45, 46, 47, 48]. In the following the basic concept of intensity interferometry is described. An extensive derivation is given in [8].

Contrary to the amplitude interferometry, the intensity interferometry is based on an incoherent source. This means that the phases $\phi(\mathbf{x})$ of the N particle production points at $\mathbf{x} = (\boldsymbol{x}, t)$ are fully random with respect to eachother. For such a chaotic source we obtain

$$\sum_{l=1}^{N} e^{i \cdot \phi_l(\mathbf{x})} = 0 \tag{2.28}$$

First consider the production and detection of one single particle as shown

in figure 2.4. The single-particle wave amplitude can be derived. Suppose

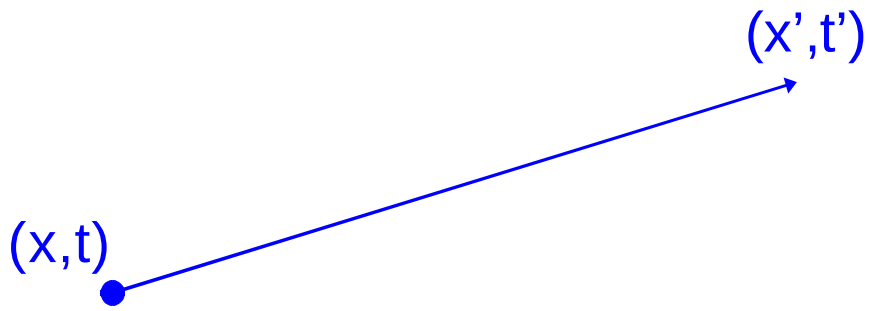

Figure 2.4: *Detection of a single particle from a production point* $\mathbf{x} = (x, t)$ *at a detector point* $\mathbf{x}' = (x', t')$.

the particle is produced at point $\mathbf{x} = (x, t)$ and detected at point $\mathbf{x}' = (x', t')$. Travelling over the path length $(\mathbf{x} - \mathbf{x}')$ leads in the plane wave approximation to a phase shift

$$e^{i \cdot \mathbf{p} \cdot (\mathbf{x} - \mathbf{x}')} \tag{2.29}$$

The amplitude $\tilde{A}$ for the detection of the particle from a single production point with production amplitude $A(\mathbf{p}, \mathbf{x})$ is

$$\tilde{A} = A(\mathbf{p}, \mathbf{x}) \cdot e^{i \cdot \mathbf{p} \cdot (\mathbf{x} - \mathbf{x}')} \cdot e^{i \cdot \phi(\mathbf{x})} \tag{2.30}$$

Now consider the case of a static source, figure 2.5, with many possible production points of the detected particle. Due to the uncertainty in the exact production point, as the detector has a limited accuracy, the detected amplitude of the particle at $\mathbf{x}'$ is the sum over all l production points $\mathbf{x}$ with respective production amplitudes $A_l(\mathbf{p}, \mathbf{x})$ and production phases $e^{i \cdot \phi_l(\mathbf{x})}$. The total detected amplitude wave-function is expressed by

$$\Psi(\mathbf{x}') = \sum_l A_l(\mathbf{p}, \mathbf{x}) \cdot e^{i \cdot \mathbf{p} \cdot (\mathbf{x} - \mathbf{x}')} e^{i \cdot \phi_l(\mathbf{x})} \tag{2.31}$$

Using a density distribution function $\rho(\mathbf{x})$ for the production points the above sum for the detected amplitude wave-function can be replaced by an integral

$$\Psi(\mathbf{x}') = \int \mathbf{dx} \cdot \rho(\mathbf{x}) \cdot A(\mathbf{p}, \mathbf{x}) \cdot e^{i \cdot \phi(\mathbf{x})} \cdot e^{i \cdot \mathbf{p} \cdot (\mathbf{x} - \mathbf{x}')} \tag{2.32}$$

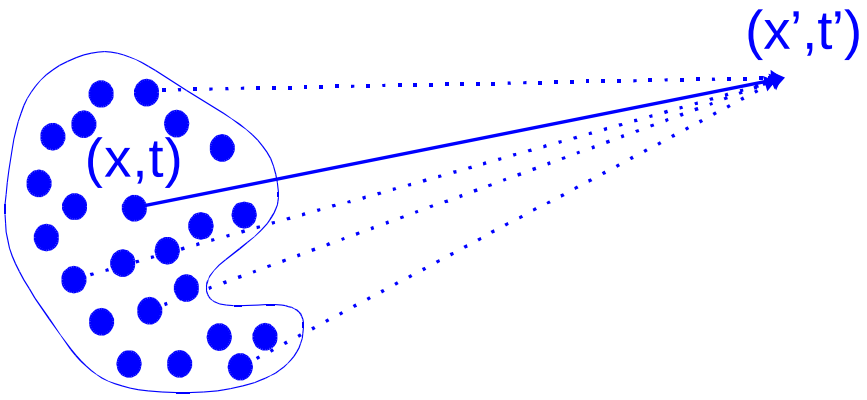

Figure 2.5: *Static source, each point* $\mathbf{x} = (x,t)$ *may have produced the particle detected at point* $\mathbf{x}' = (x',t')$.

The probability of detecting a single particle at $\mathbf{x}'$ is expressed in the single-particle distribution function $P(\mathbf{p})$ and is given by the absolute square of the total probability amplitude

$$P(\mathbf{p}) = |\Psi(\mathbf{x}')|^2 = \int \mathbf{dx} \cdot \rho(\mathbf{x}) \cdot A^2(\mathbf{p},\mathbf{x}) \tag{2.33}$$

In a similar way the two-particle probability function will be derived below; see figure 2.6. Here, the particles are assumed to be identical pions originating from production points $\mathbf{x_1} = (x_1,t_1)$ and $\mathbf{x_2} = (x_2,t_2)$. Respecting the symmetrization for bosons (and in a similar way the anti-symmetrization for fermions) the two-particle amplitude is

$$\begin{aligned} \Psi_{12}(\mathbf{x_1'},\mathbf{x_2'}) &= \tfrac{1}{\sqrt{2}} \cdot \\ \big(\; & A(\mathbf{p_1},\mathbf{x_1}) \cdot e^{i\cdot\phi(\mathbf{x_1})} \cdot e^{i\cdot\mathbf{p_1}\cdot(\mathbf{x_1}-\mathbf{x_1'})} \cdot A(\mathbf{p_2},\mathbf{x_2}) \cdot e^{i\cdot\phi(\mathbf{x_2})} \cdot e^{i\cdot\mathbf{p_2}\cdot(\mathbf{x_2}-\mathbf{x_2'})} \; + \\ & A(\mathbf{p_2},\mathbf{x_1}) \cdot e^{i\cdot\phi(\mathbf{x_1})} \cdot e^{i\cdot\mathbf{p_2}\cdot(\mathbf{x_1}-\mathbf{x_2'})} \cdot A(\mathbf{p_1},\mathbf{x_2}) \cdot e^{i\cdot\phi(\mathbf{x_2})} \cdot e^{i\cdot\mathbf{p_1}\cdot(\mathbf{x_2}-\mathbf{x_1'})} \; \big) \end{aligned} \tag{2.34}$$

Again the measurement of two pions from a static chaotic source leads to a sum over all possible production points. Using the density distributions the two-particle probability function $P(\mathbf{p_1},\mathbf{p_2})$ is

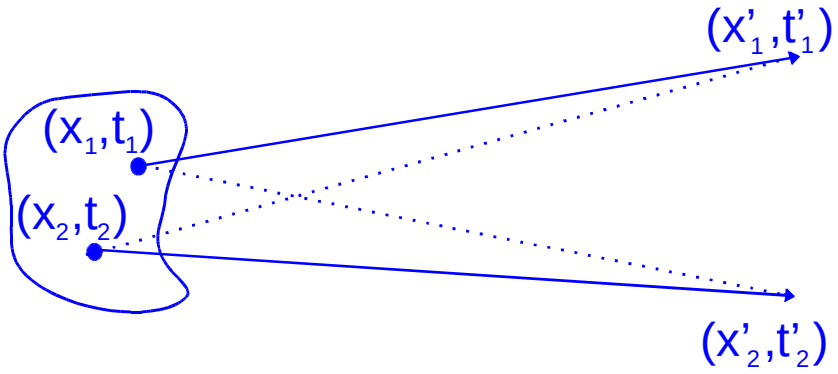

Figure 2.6: *The detected identical pions at* $\mathbf{x_1'} = (x_1', t_1')$ *and* $\mathbf{x_2'} = (x_2', t_2')$ *with respective momenta* $\mathbf{p_1}$ *and* $\mathbf{p_2}$ *may have come from* $\mathbf{x_1} = (x_1, t_1)$ *and* $\mathbf{x_2} = (x_2, t_2)$*, respectively, or vice versa.*

$$\begin{aligned} \int\int \mathbf{dx_1} \cdot \mathbf{dx_2} \cdot \rho(\mathbf{x_1}) \cdot \rho(\mathbf{x_2}) \cdot |\Psi_{12}(\mathbf{x_1'}, \mathbf{x_2'})|^2 \quad &= \\ \int \mathbf{dx_1} \cdot \rho(\mathbf{x_1}) \cdot A^2(\mathbf{p_1}, \mathbf{x_1}) \cdot \int \mathbf{dx_2} \cdot \rho(\mathbf{x_2}) \cdot A^2(\mathbf{p_2}, \mathbf{x_2}) \quad &+ \\ \int \mathbf{dx_1} \cdot \rho(\mathbf{x_1}) \cdot A(\mathbf{p_1}, \mathbf{x_1}) \cdot A(\mathbf{p_2}, \mathbf{x_1}) \cdot e^{i \cdot (\mathbf{p_1} - \mathbf{p_2}) \cdot \mathbf{x_1}} \quad &\cdot \\ \int \mathbf{dx_2} \cdot \rho(\mathbf{x_2}) \cdot A(\mathbf{p_2}, \mathbf{x_2}) \cdot A(\mathbf{p_1}, \mathbf{x_2}) \cdot e^{i \cdot (\mathbf{p_2} - \mathbf{p_1}) \cdot \mathbf{x_2}} \end{aligned} \tag{2.35}$$

Using the derived relation for the single-particle probability the two-particle probability can be written as

$$\begin{aligned} P(\mathbf{p_1}, \mathbf{p_2}) = P(\mathbf{p_1}) \cdot P(\mathbf{p_2}) + \\ |\int \mathbf{dx} \cdot \rho(\mathbf{x}) \cdot A(\mathbf{p_1}, \mathbf{x}) \cdot A(\mathbf{p_2}, \mathbf{x}) \cdot e^{i \cdot (\mathbf{p_1} - \mathbf{p_2}) \cdot \mathbf{x}}|^2 \end{aligned} \tag{2.36}$$

An effective source density distribution can be defined

$$\rho_{eff}(\mathbf{x}) = \rho(\mathbf{x}) \cdot \frac{A(\mathbf{p_1}, \mathbf{x}) \cdot A(\mathbf{p_2}, \mathbf{x})}{\sqrt{P(\mathbf{p_1})} \cdot \sqrt{P(\mathbf{p_2})}} \tag{2.37}$$

A measurement of the ratio of the two-particle probability to the single-particle probabilities yields a function depending on the Fourier transform of the effective source density distribution $\tilde{\rho}_{eff}(\mathbf{q})$, expressed in terms of the function $C(\mathbf{p_1}, \mathbf{p_2})$, where $\mathbf{q} = \mathbf{p_1} - \mathbf{p_2}$ is the relative four-momentum

difference

$$C(\mathbf{p_1},\mathbf{p_2}) = \frac{P(\mathbf{p_1},\mathbf{p_2})}{P(\mathbf{p_1})\cdot P(\mathbf{p_2})} =$$
$$1 + |\int \mathbf{dx}\cdot\rho_{eff}(\mathbf{x})\cdot e^{i\cdot\mathbf{q}\cdot\mathbf{x}}|^2 = 1 + |\tilde{\rho}_{eff}(\mathbf{q})|^2 \tag{2.38}$$

In case the production amplitudes do not depend on their respective production points the Fourier transform of the source distribution is measured, as then $\rho_{eff}(\mathbf{x}) = \rho(\mathbf{x})$. For static-source distributions this is likely to be the case.

However, in high-energy physics dynamic-source distributions are measured. Most likely the production amplitudes of the rapidly expanding systems only have similar momentum distributions in case their production points are close in both space and time. The integral will thus be non-vanishing for close production points. This strong phase-space relation leads on the one hand to the difficult situation that HBT measurements will only probe a limited region of the source. This results in an effective source size R_{eff} smaller than the "true" source size R: $R_{eff} < R$ [8]. On the other hand, this dependence on the momentum distribution can be exploited to study the dynamic-source size by making selections in momentum space [49, 50].

2.8.2 Parameterization of the Measured Correlation Functions

The correlation function $C(\mathbf{p_1},\mathbf{p_2})$, as derived in the previous subsection for identical pions, shows that the density distribution of the particle-emitting region determines the dependence on the relative four-momentum. Lack of knowledge of the shape of the source density distribution has led to the simple assumption of a static gaussian distribution

$$\rho(\vec{r},t) = \frac{1}{\pi^2\cdot R^3\cdot\Delta\tau}\cdot e^{-\frac{r^2}{R^2}-\frac{t^2}{\Delta\tau^2}} \tag{2.39}$$

where R and $\Delta\tau$ are the radius and lifetime of the source, respectively. The Fourier transform of the gaussian distribution reads

$$\tilde{\rho}(q,q_0) = e^{-\frac{q^2\cdot R^2}{4}-\frac{q_0^2\cdot\Delta\tau^2}{4}} \tag{2.40}$$

so that the correlation function can be written as

$$C(\mathbf{p_1},\mathbf{p_2}) = 1 + e^{-\frac{q^2\cdot R^2}{2}-\frac{q_0^2\cdot\tau^2}{2}} \tag{2.41}$$

where $q = |\vec{p}_1 - \vec{p}_2|$ and $q_0 = |E_1 - E_2|$ and the relative four-momentum $\mathbf{q} = (\vec{q}, q_0)$. Such parameterizations can further be expanded in the spatial dimensions. Note that $q_0 = \vec{q} \cdot \vec{\beta}$ with $\vec{\beta} = (\vec{p}_1 + \vec{p}_2)/(E_1 + E_2)$ the velocity of the pion pair. Suppose the correlation function is studied in the longitudinal center of mass frame of the pion pair. Two orthogonal directions, one parallel to the transverse direction of the pion pair, "outward direction", and one perpendicular to this direction, "sideward direction", can be defined; see figure 2.7.

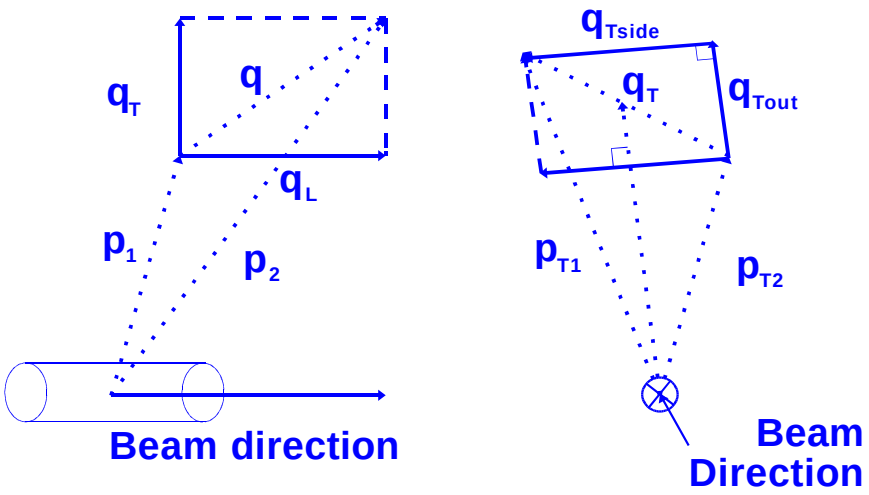

Figure 2.7: *The relative momentum can be split up in components in the beam direction (q_L) and transverse to the beam direction (q_T). The transverse component can further be split in the direction of the average p_T of the pion pair (q_{Tout}) and perpendicular to this direction (q_{Tside}).*

This enables a parameterization

$$C(\mathbf{p_1}, \mathbf{p_2}) = 1 + e^{-\frac{(q_{Tout} \cdot R_{Tout})^2 + (q_{Tside} \cdot R_{Tside})^2 + (q_L \cdot R_L)^2}{2}} \tag{2.42}$$

where the relative momenta are, $q_{Tout} = \frac{(\vec{q} \cdot \vec{\beta})}{|\vec{\beta}|}$ in the outward direction, $q_{Tside} = \frac{|\vec{q} \times \vec{\beta}|}{|\vec{\beta}|}$ in the sideward direction and q_L in the longitudinal direction. Since the longitudinal velocity of the pion pair $\beta_L = 0$ in the longitudinal center-of-mass system and q_{Tside} is orthogonal to the transverse velocity β_T

of the pion pair we derive $q_0 = \vec{q} \cdot \vec{\beta} = q_{Tout} \cdot \beta_T$. Therefore, the outward radius R_{Tout} and the sideward radius R_{Tside} are related by the lifetime $\Delta\tau$ of the emitting source

$$R_{Tout}^2 = R_{Tside}^2 + (\beta_T \cdot \Delta\tau)^2 \tag{2.43}$$

The long lifetime of the mixed phase, see section 2.2, may reveal itself in a large difference between R_{Tout} and R_{Tside}. Another often used parameterization is a gaussian as a function of the invariant relative four-momentum $q_{inv} = \sqrt{q^2 - q_0^2}$

$$C(\mathbf{p_1}, \mathbf{p_2}) = 1 + e^{-\frac{(q_{inv} \cdot R_{inv})^2}{2}} \tag{2.44}$$

The interpretation of the corresponding four-dimensional radius R_{inv} is not straightforward. Usually the study of the invariant radius is used for comparison between experiments. The later introduced correlation strength allows to judge the quality of the data. Care should be taken in the direct comparison of the results on the radii derived by different experimental groups, as the parameterization may differ for the quoted radii in the factor of 2 in the denominator of the Gaussian. The above derived parameterizations are used in this thesis and for example also by the NA35 [51] collaboration.

2.8.3 Corrections to the Correlation Functions

The parameterizations described in subsection 2.8.2 are applicable for an ideal incoherent static-source distribution. As mentioned in subsection 2.8.1, the interaction zone in heavy-ion collisions may be rapidly expanding. We further assume the studied correlated particles to be pions. Thus the radii $R(\mathbf{p_1}, \mathbf{p_2})$ are a function of the momenta of the pion pairs. Furthermore, for the case of a fully coherent source it can be proven [8, 48, 52] that $C(\mathbf{p_1}, \mathbf{p_2}) \equiv 1$ for bosons. The correlation function has no dependence on the source density distribution. In order to interpolate between these two extreme cases the chaoticity parameter λ is introduced

$$C(\mathbf{p_1}, \mathbf{p_2}) = 1 + \lambda \cdot |\tilde{\rho}(\mathbf{q})|^2 \tag{2.45}$$

Here, λ represents the partial incoherence of the source. It has been pointed out in [53] that a correct formulation for partial incoherence should be based on a parameter $c = n_{chaotic}/n$. This is the ratio of the number of chaotically emitted pions, $n_{chaotic}$, to the total number of emitted pions, n. Such a formulation results in

$$C(\mathbf{p_1}, \mathbf{p_2}) = 1 + 2 \cdot c \cdot (1 - c) \cdot |\tilde{\rho}(\mathbf{q})| + c^2 \cdot |\tilde{\rho}(\mathbf{q})|^2 \tag{2.46}$$

The extended equation using the incoherence parameter is not used in this thesis as it suggests an experimental sensitivity to the incoherence which is not realistic. Processes like strong final-state interactions, Coulomb repulsion, resonance decays and experimental background obscure the measured correlation strength and radii. The residual correlation strength is believed to be accurately expressed by the parameter λ. However, for a given analytical function used to parameterize the experimental correlation function, the radii and λ are not independently determined [54]. Therefore when comparing radii the correlation strength needs to be compared simultaneously.

For pions the strong interaction can be assumed weak enough to be neglected. However, recently [55] it was stated that the standard calculation leading to the Gamov factor should be significantly corrected in the region of small relative momenta due to final-state strong interactions. In this thesis, the standard Gamov factor is used to be compatible with the results from other experiments. The standard Coulomb-corrected correlation coefficient can be obtained [46] as follows

$$C^{coulomb}(\mathbf{p_1}, \mathbf{p_2}) = G(\mathbf{p_1}, \mathbf{p_2}) \cdot C(\mathbf{p_1}, \mathbf{p_2}) \tag{2.47}$$

where $G(\mathbf{p_1}, \mathbf{p_2})$ is the Gamov factor defined as

$$G(\mathbf{p_1}, \mathbf{p_2}) = \frac{2\pi \cdot \eta}{e^{2 \cdot \pi \cdot \eta} - 1} \tag{2.48}$$

with $\eta = (\alpha \cdot m)/(|\mathbf{p_1} - \mathbf{p_2}|$ the Sommerfeld factor, α the fine-structure constant and m the mass of the particles the correlation of which is studied. In the presented results in chapter 5 the Coulomb correction is always taken into account.

2.9 Summary

The concept of using heavy-ion collisions to create hot and dense hadronic matter was introduced. Two extreme models, that of complete stopping and that of partial transparency were presented. Independent of these models the temperature-time evolution of the dense matter can be calculated using longitudinal hydrodynamic expansion. The lifetime in case of a QGP phase was shown to be about five times larger than for the case of a hot hadron gas phase. Such a long lifetime should manifest itself in large source sizes at freeze-out.

Several possible signals from the QGP have been described. These signals were also discussed for the case of a hot hadron gas. Up to now no

experiment has been able to verify the existence of the QGP. However, several of the proposed signatures, strangeness enhancement and J/Ψ suppression, have been observed. These measurements can be both described in the framework of the QGP and the hot hadron-gas phase.

Better knowledge of the space-time evolution, as all these signals are space and time dependent, could enable us to draw unambiguous conclusions from such measurements. The intensity interferometry was shown to provide the means to measure the space-time evolution of the source distribution function. Due to effects like the source dynamics and possible coherence and background processes, the conclusions drawn from the measured correlation function on the extracted source radii must be considered with care, regarding the obtained correlation strength and the conditions, e.g. experimental acceptance and background, under which the data were taken.

If such a careful analysis is performed it should in principle be possible to distinguish between a QGP and a hot hadron gas already from the measured space-time distribution. In this thesis such an analysis is presented for 200 A·GeV S+Au reaction.

Chapter 3

The WA93 Experimental Setup

In this chapter an overview of the experimental setup and its arrangement in the SPS heavy-ion beam-line will be given. The layout of the experimental setup is shown in figure 3.1. The 200 A·GeV sulphur beam enters the beam counter (start detectors) from the left. The target foil, either sulphur or gold, was placed at the entrance of the large dipole magnet. The negatively charged particles, from a nuclear reaction, are bent by the dipole magnet into the acceptance of a tracking system consisting of four position sensitive Multi Step Avalanche Chambers. At the entrance of the magnet a Silicon Drift Detector measures the rapidity distribution of traversing charged particles. Further to the right neutral mesons and photons are measured by the Photon Multiplicity Detector (PMD) and the Lead-Glass Spectrometer. Two layers of Streamer-Tube Detectors measure the position of traversing charged particles in front of the Lead-Glass Spectrometer and serve as a charged particle veto for the Lead-Glass Spectrometer. Behind the photon spectrometer two calorimeters are situated. The Mid-rapidity Calorimeter measures the transverse energy from the nuclear reaction whereas the Zero-Degree Calorimeter measures the forward directed energy. These two calorimeters define together with the start detectors the reaction trigger and the centrality of the collision. First of all the Trigger System, section 3.5, defining the centrality of the heavy-ion collision, is discussed. The trigger system consists of the Beam Counter, section 3.2, and calorimeters. The calorimeters measure the energy of particles in the beam, section 3.3, and transverse to the beam direction, section 3.4.

The main interest of the WA93 experiment [5, 56, 57] is the measurement

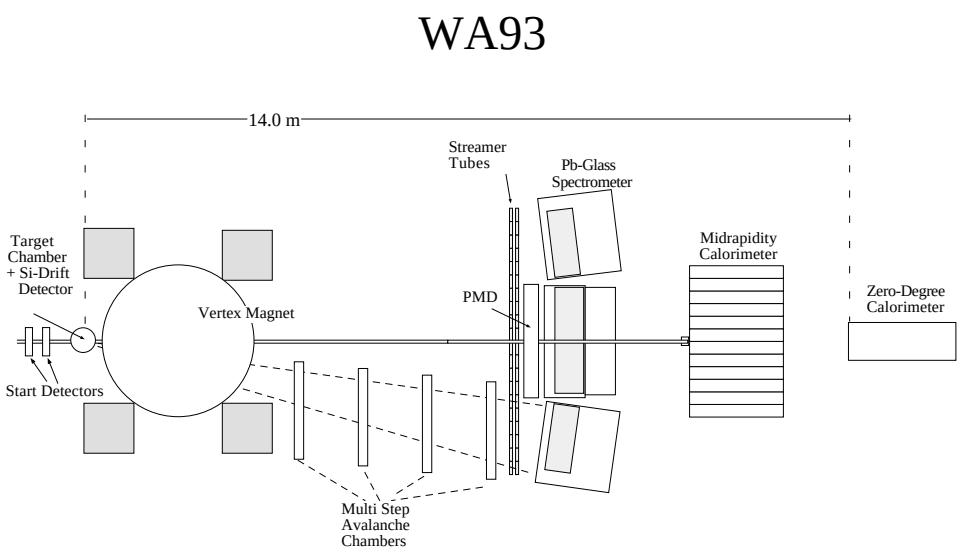

Figure 3.1: *Schematic layout of the WA93 experiment.*

of direct photons. A photon spectrometer consisting of a large array of lead-glass modules, Lead-Glass Spectrometer, section 3.8, and a Photon-Multiplicity Detector, section 3.9, are used to measure the neutral mesons and photons.

Special emphasis will be put on the Charged-Particle Spectrometer; see section 3.10. As has been shown in section 2.4 the measurement of the space-time evolution is a prerequisite for an understanding of the measured direct photon spectra. The charged-particle spectrometer provides the means to do negatively charged-particle intensity interferometry; see section 2.8. It consists of the dipole magnet Goliath and four large-acceptance Multi-Step Avalanche Chambers (MSAC). An extensive description of the design, building, operational requirements, principal of operation, and optical readout of the chambers will be given as the author was actively involved in these subjects.

A new development in which the author took part, enabling direct read-out of the charge at the back of the chamber, is presented in section 3.12. For this purpose a charge-sensitive chip and a fast read-out system, based on Digital Signal Processors, were developed.

The schematic layout of the Data-Acquisition System with special emphasis on the MSAC chambers can be found in section 3.11.

3.1 Production of the CERN Heavy-Ion Beam

To reach the beam energy of 200 A·GeV for sulphur particles and 160 A·GeV for lead particles the atoms are first ionized partially to a high charge state in an ECR-ion source and subsequently linearly accelerated in a 50 MeV LINAC. After the LINAC the ions enter fully ionized the 800 MeV Booster machine, after which they are further accelerated in the 28 GeV Proton Synchrotron (PS) (200 m diameter). Finally the ions enter the Super Proton Synchrotron (SPS) (2.2 km diameter) and get accelerated up to 200 (160) A·GeV, before being extracted into the heavy-ion beam-line leading to the West Area where the WA93 experiment is installed. A complete cycle of accelerating the beam particles and extracting them takes about 19 seconds. During 5 seconds the beam is extracted while for about 2 to 3 seconds during this period a sufficiently constant beam intensity is maintained.

3.2 Beam Counter

The beam counter consists of a halo wall, two quartz-Cherenkov counters and a scintillator paddle. It determines whether a beam particle approaching the target had already undergone interactions upstream producing secondary particles.

The beam from the SPS may have had interactions with rest gas atoms in the vacuum of the beam-line during the transport over a distance of 1 km. The halo wall in this case will mostly register muons. The scintillators in the halo wall are combined in OR-mode $S_{innerhalo}$ and form an inhibit in the off-line analysis package; see section 4.2.

On their way to the target the beam particles pass two quartz-Cherenkov counters viewed by photomultipliers. The presence and charge of the particles can be determined from the energy of the emitted Cherenkov radiation that is proportional to

$$\frac{dE}{dx} = \frac{4 \cdot \pi^2 \cdot Z^2 \cdot e^2}{c^2} \int_{\nu_{min}}^{\nu_{max}} (1 - \frac{1}{\beta^2 \cdot n^2}) \cdot \nu \cdot d\nu \qquad (3.1)$$

where β is the velocity of the particle, n the index of refraction and ν the frequency of the emitted Cherenkov light. The risetime of the photomultiplier signals is fast, in the order of several nano-seconds. The narrow pulse width of the signal allows to count the individual particles in the beam flux of $\sim 10^6 - 10^7$ Hz. Two thresholds are set for the Cherenkov counters. A lower threshold S_{low} is set just above the noise level and an upper threshold

S_{high} is set just above the expected signal in order to prevent pile up arising from several beam particles entering the setup.

In order to check the positioning of the beam, a scintillator paddle of the dimension 64×50 mm^2 and 5 mm thick, with a 3 mm diameter hole, was placed 0.36 m downstream. In case of a signal, $S_{littleveto}$, in the paddle, due to a reaction in the start counters upstream or a bad beam positioning on the target, the beam trigger was inhibited. The validity of a beam particle exactly centered on the target was logically defined as

$$S_{validbeam} = (S^1_{low}.\overline{S^1_{high}})(S^2_{low}.\overline{S^2_{high}}).\overline{S_{littleveto}}.\overline{S_{inner\,halo}} \qquad (3.2)$$

The targets used were 0.25 g/cm^2 thick Au or S foils. As the flux of the beam was about $1.5 \cdot 10^6$ particles per spill, and the effective spill length is two seconds, the luminosity of the beam is $L = 6 \cdot 10^{26}$ cm^{-2}s^{-1}. The nuclear interaction cross-section for S + Au collisions is 3360 mb. Thus, an interaction rate of about 2000 reactions per second was measured during this experiment.

3.3 Zero-Degree Calorimeter

The Zero-Degree Calorimeter (ZDC) is designed to determine the energy loss of the incident beam particles by measuring the energy near a polar angle $\theta = 0°$. The ZDC has a sandwich-like structure of 60×60 cm^2 area uranium and scintillator plates. The calorimeter is located at 13.85 m from the target and has a length of 190 cm. The ZDC detects all particles coming from the target at very small angles, $\theta < 0.3° \cong \eta > 6$, where $\eta = -ln\tan(\theta/2)$ is the pseudo-rapidity. The detector consists of an electromagnetic part of 17 cm depth, equivalent to 20.5 radiation lengths (X_o), and a 172 cm long hadronic part, equivalent to 9.6 absorption lengths. Both the electromagnetic and hadronic energy can be measured using uranium and scintillator plates. The scintillator plates are read out via wavelength-shifter plates and light guides with 16 photomultipliers. The pulse height spectra of the ADC's were calibrated to the beam energy by adjusting the voltage of the 16 photomultiplier bases. They are summed and sent to a discriminator providing two logic signals, Z_{low} if a large amount of beam energy is missing, Z_{high} if the full beam energy is detected. The fast ZDC signal is combined with the Beam Counter, see section 3.2, and MIRAC, see section 3.4, to form the WA93 Trigger, see section 3.5.

3.4 MIRAC Calorimeter

The MId-RApidity Calorimeter (MIRAC) measures the transverse electromagnetic and hadronic energy in the kinematic region of mid-rapidity defined as half the beam rapidity. It is located at 11.25 m from the target and measures from $\eta = 6$ up to $\eta = 3$. It consists of four 1.32×1.20 m^2 blocks with a central hole of 10.5×10.5 cm^2. The electromagnetic part has a length of 5.6 radiation lengths or 0.6 hadron absorber lengths, made up by a stack of absorption and scintillator plates. Each block consists of 6×6 towers where each tower has an area of 20×20 cm^2. The towers are read out via wavelength shifting plates and light guides by photomultipliers. Using the calibration factor and position of a tower the transverse energy $E_T = E \sin\theta$ of the traversing particles can be measured for each event. The summation and angular weighting of the transverse energy is done for all measured particles in one event by hardware. The summed MIRAC transverse energy signal can be used for on-line trigger purposes. The energy resolution was $11\,\%/\sqrt{E(GeV)}$ for the electromagnetic part and $34\,\%/\sqrt{E(GeV)}$ for the hadronic part. The four inner towers, surrounding the beam pipe, were not used since frequently a signal above the highest energy threshold, most likely due to spectator particles from the beam, occurred. Three logic signals, M_{low}, M_{high}, and $M_{peripheral}$, are generated from the sum of the photomultiplier ADC signals. A signal M_{low} means very little energy measured in the MIRAC, M_{high} the opposite. The $M_{peripheral}$ was chosen to cover the intermediate region in transverse energy. The centrality of a collision is characterised by these three logical signals together with the ZDC, see section 3.3, and the beam counter, see section 3.2, and is expressed in the trigger signal, see section 3.5.

3.5 Trigger

The trigger signal characterizing the centrality of a collision is a combination of the logic signals from the beam counter, ZDC and MIRAC. The correlation between the measured ZDC and MIRAC energies is shown in figure 3.2. Measuring large transverse energy in the MIRAC and little forward energy in the ZDC corresponds to a central event. The necessity to study whether the reaction was central or peripheral arises from the fact that the quark-gluon plasma is expected to be observed most likely for central events. Here, large collision zones are created. The peripheral events correspond to well-known hadron-hadron collisions. The rate of events from the various trigger

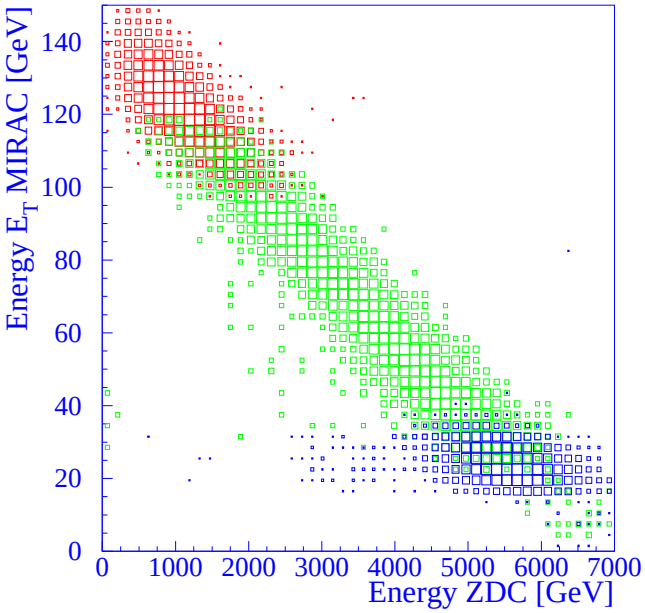

Figure 3.2: *Transverse energy measured in the MIRAC versus the forward energy in the ZDC for 200 GeV/nucleon S+Au reactions.*

Table 3.1: *Trigger definitions.*

Trigger Class	Trigger definition
E_THigh	$S_{validbeam} \cdot M_{high} \cdot M_{peripheral} \cdot M_{low}$
Minimum Bias	$S_{validbeam} \cdot M_{low}$
Semi Central	$S_{validbeam} \cdot \overline{M_{high}} \cdot M_{peripheral} \cdot M_{low}$
E_TPeripheral	$S_{validbeam} \cdot Z_{low} \cdot \overline{M_{peripheral}} \cdot M_{low}$
Beam	$S_{validbeam} \cdot Z_{high} \cdot \overline{M_{high}} \cdot \overline{M_{peripheral} M_{low}}$

classes E_THigh : E_TPeripheral : Semi Central : Beam = 1 : 1 : 3 : 2000 as determined from the composition of the least biased sample of reaction events (Minimum Bias). Using down-scaling factors for the various triggers the ratio of data taken for the respective triggers is 7 : 3 : 3 : 1. So roughly 50 % of the registered data are central events. The ZDC signal was removed in the on-line trigger analysis. Since the measured beam energy by the ZDC for the beam trigger started to degrade in the course of the experiment most

likely due to radiation damage of the ZDC. Further rejection criteria in the off-line analysis led to the following estimate of 1992 data, presented in table 3.2.

Table 3.2: *Number of events taken for the magnetic dipole field setting on or off.*

	S+Au Field On	S+Au Field Off	S+S Field On
E_TPeripheral	$1.0 \cdot 10^6$	$0.2 \cdot 10^6$	$56 \cdot 10^3$
Semi Central	$0.5 \cdot 10^6$	$83 \cdot 10^3$	$30 \cdot 10^3$
E_THigh	$1.2 \cdot 10^6$	$0.26 \cdot 10^6$	$70 \cdot 10^3$

3.6 Si-Drift Detector

In order to measure the charged-particle multiplicity and rapidity distributions a Si-Drift detector was implemented in the WA93 experiment. The pseudo-rapidity interval covered by this detector was that of the photon-multiplicity detector discussed in section 3.9. This coverage is required to obtain the N_γ/N_{ch} ratios, see section 2.4.

In the WA93 experiment a 320 μm thick circular detector with a 64 mm diameter, a central hole of 16 mm and 360 anode pads at the circumference was used. In Si-drift detectors [57, 58, 59] the negative electrical charge, caused by traversing ionizing particles, is transported over drift distances of several cm. An array of reverse biased p-strips on both sides of the high-resistivity n-type silicon fully depletes the bulk and maintains a gutter-like potential. The ionization-electrons created by charged particles are driven parallel to the surface towards the collecting anodes on the edge of the detector. Here, external amplifiers pickup the signal and transfer it to a gaussian shaper unit and flash ADC's for further processing. Since the drift velocity of the Si-wafer is known the position of the charged particles can be determined with a 20 μm resolution.

3.7 Streamer-Tube Detector

A large array of streamer tubes [57, 60] serves as a thin and efficient detector and provides a charged-particle veto signal for the lead-glass detector,

section 3.8, which measures photons.

The detector consists of two planes of streamer tubes STD_1 and STD_2 at a distance of 9.22 m and 9.38 m, respectively, from the target. A streamer-tube detector is made of arrays of PVC tubes with a square cross-section of 9×9 mm^2. In the center of the PVC tube a silver plated anode wire of 100 μm diameter is kept at a voltage of about 4750 volt. The tubes are flushed with a gas mixture of 30:70 % Argon-Isobutane at 1.2 bar.

In case a charged particle passes through a tube, electrons will be liberated and an avalanche will evolve close to the wire. The field will be distorted close to the wire and electrons can recombine under photon emission. Away from the wire this radiation will free electrons in the tube. The electrons will also take part in the avalanche in case they are close to the wire, otherwise recombinations take place. The extending ion cloud, called "streamer", may reach up to the cathode walls and is self-quenching due to the weaker field far from the wire. The walls of the tube are covered with a graphite layer in order to prevent electrons from being liberated from the walls that will cause multiple streamers. The streamer tubes are read out capacitively. The surface area of the streamer-tube planes is covered by 21 $\times$ 21 cm^2 sized printed circuit boards carrying 40 or 160 conducting pads facing the tubes. The 160-pad boards are used in the high multiplicity area, close to mid-rapidity, while the 40-pad boards are used in the outer regions of the STD planes. The two STD planes together contain about 40.000 pads.

3.8 Lead-Glass Spectrometer

One of the proposed interesting signals from the quark-gluon plasma is the observation of direct photons. In order to distinguish this signal from the enormous background coming from neutral meson decay (mostly π^0 and η) a high reconstruction efficiency is needed. This requires a photon detector with very good energy resolution and high granularity.

In WA93 three detectors with high position resolution were placed in a U shaped form. One was SAPHIR (Single-Arm Photon detector for Heavy-Ion Reactions) which had already been used in the WA80 experiment. It consists of 1278 $SF5$ lead-glass blocks of a length of 460 mm and an area of 35×35 mm^2 . The length is approximately equal to 18 electromagnetic radiation lengths and about 1 hadronic interaction length. Photomultipliers read out the modules at the back. The two other detectors TOWER1 and TOWER2 are positioned vertically on each side of SAPHIR. They cover $2.1 < \eta < 2.9$ in pseudo-rapidity at 10.06 m from the target. The towers

consist of 1260 modules of TF_1 lead glass each $4.0 \times 4.0 \times 40$ cm^3 in size. The length of 40 cm corresponds to 14.4 electromagnetic radiation lengths and about 1 hadronic absorption length ($\lambda_{SF5} = 46$ cm and $\lambda_{TF_1} = 38$ cm). Due to the limited absorption length $\approx 37\,\%$ hadrons cause a highly irregular shower, 63 % of the hadrons deposit energy according to a minimum-ionizing particle.

The energy resolutions of SAPHIR, TOWER1 and TOWER2 are similar and amount to $0.4\,\% + 6\,\%/\sqrt{E(GeV)}$.

The gain of the photomultipliers is monitored by a laser reference system. The laser itself is monitored using a reference photomultiplier calibrated by a ^{241}Am doped NaI crystal. The relative gain stability is better than 1 %.

3.9 Photon-Multiplicity Detector

The Photon-Multiplicity Detector (PMD) aims to select events with a high photon content. By a simultaneous measurement of the charged particle multiplicity, using the Si-drift detector, and of the photon multiplicity, the ratio of the number of photons over the number of charged particles can be studied, see section 2.4. An increased ratio might signal the formation of hot interacting hadronic matter or even the formation of the QGP.

The PMD, with a size of 200×160 cm^2 and located at 10.06 m from the target is a pre-shower device. Its angular coverage is $1^\circ < \theta < 6^\circ$. A conversion layer of 2 cm lead equivalent to 3.8 radiation lengths is used. This thickness has been chosen to optimize photon efficiency and minimize hadronic interactions.

The electrons are detected in the beginning of the shower by scintillating pads glued in closed-packet arrays on the converter sheet. For the inner area of 60×60 cm^2, with a central hole of 10×10 cm^2 to let the beam pass through, a pad size of 15×15 mm^2 is used, the remainder has 25×25 mm^2 pads. The signal of each pad is guided using a wavelength shifting fibre to a CCD (Charge Coupled Device) camera equipped with an image intensifier.

The 7600 pads are grouped in quadrants. A quadrant is read out by 1900 pads, yielding for each pad about 10-15 pixels at the CCD level. The CCD camera has a resolution of 145×218 pixels.

3.10 Charged-Particle Spectrometer

The charged-particle spectrometer was incorporated in the WA93 setup to study in detail through intensity interferometry the space-time evolution

of the hot hadronic system produced in the heavy-ion collision. Therefore the acceptance was chosen, together with that of the photon spectrometer, around mid-rapidity [61, 62, 63, 64].

The charged-particle spectrometer employs the large dipole magnet Goliath, with a 1.6 m pole gap and a 2 Tm bending power. The pole diameter is 2.2 m. The horizontally bent charged particle tracks are detected in four Multi-Step Avalanche Chambers (MSAC), each having a 1.2×1.6 m^2 sensitive area. The coordinate system for the WA93 experiment is defined as follows. The beam direction corresponds to the z-axis, the normal to the z-axis in horizontal direction corresponds to the x-axis and the vertical direction corresponds to the y-coordinate. The chambers are positioned, using the primary ionization gap as plane of reference and the z-coordinate, at z_1 = 425.6 cm, z_2 = 564.0 cm, z_3 = 689.4 cm and z_4 = 814.5 cm from the target. Each chamber covers $\pm$ 60 cm in the vertical and 160 cm in the horizontal direction. The sensitive areas of the four chambers closest to the beam line start at x_1 = 31.2 cm, x_2 = 40.5 cm, x_3 = 50.7 cm, and x_4 = 60.5 cm, respectively. The magnetic field strength was measured for a grid of spatial positions between and near the magnet poles. Further details are given in section 4.2.2. A measurement of the position of each track in the chambers and thus the direction of the tracks together with the knowledge of the magnetic field allows for the reconstruction of the momenta, see section 4.5, of negative charged particles.

The spectrometer has to fulfill several requirements. First of all it has to operate in a high-multiplicity environment, with 40 to 100 charged particles per m^2. A large acceptance of 1.5 units of rapidity around mid-rapidity was required. To be able to do intensity interferometry a high momentum resolution was needed. Furthermore, the system had to be of a light construction, in order not to disturb the photon measurements.

A magnetic spectrometer using MSAC chambers largely fulfills these demands. Particle identification, e.g. using a time-of-flight detector, was not implemented in the WA93 experiment. The upgrade WA98 has such a device. Therefore, the measurement of negatively charged particles was chosen in order to keep the amount of background tracks for the $\pi^-\pi^-$-correlations as low as possible. This is so because the yield of other negatively charged particles is small as compared with π^- whereas in case of positive charged particles there is a considerable admixture of protons to the yield of π^+. The MSAC chambers are gaseous ionization detectors [65, 66, 67]. In general, ionization detectors are based on the principle that incident radiation ionizes the compound which can be a gas, a fluid or a solid. The ionization is read out usually after amplification [68]. Gas-ionization detectors are widely

used in medicine, astrophysics and biology [69]. The MSAC chamber uses a gas-mixture of Neon and Tri-Ethyl-Amine (TEA), a photo-emissive gas, under atmospheric pressure [70, 71, 72, 73], allowing optical read out of this detector.

In the following subsections the design characteristics, the construction, section 3.10.1, and the optical read-out, section 3.10.2, will be discussed. Furthermore, the monitoring and operation, section 3.10.3, of these detectors will be outlined.

3.10.1 Construction and Principle of Operation

The Multi-Step Avalanche Chambers in the WA93 setup consisted of a sandwich of 18 1.2×1.6 m^2 frames. These detectors were developed by and built at the University of Geneva, Switzerland [61, 62, 63]. In fact a MSAC is a stack of three Parallel-Plate Avalanche Chambers (PPAC). One MSAC has twelve electrodes which are called meshes, as schematically shown in figure 3.3. A mesh consists of crossed stainless steel wires, equally spaced at a distance of 500 μm and each having a 50 μm diameter. The frames are made of a very light composite of vetronite, honeycomb and foam. Using this composite, the frames have a total thickness corresponding to only 10 % of a radiation length and the meshes have in total 0.7 % radiation length.

The frames span the meshes with a tension of 15-50 kg/m. Such a tension is needed because the parallelism of the electrodes is a critical factor for the operation of the PPAC. It should be better than 20 μm for the 4 mm amplification gaps. Special care is taken to prevent sparking at the edges of the chambers where the electromagnetic field is not homogeneous. A 0.5 mm thin vetronite strip protruding 5 mm inside the chamber volume is used. To secure the wanted parallelism ceramic spacers with the same geometry have been used.

When a charged particle passes through the first gap of the MSAC mesh 1 and 2, primary ionization is produced, see figure 3.3.

The Coulomb interaction between the electromagnetic field of the particle and the gas atoms is the dominant process for the ionization. The average energy loss of a charged particle crossing a thin medium is described by the Bethe-Bloch formula [68]. The particles crossing the MSAC chambers are mostly minimum-ionizing-particles (MIP). The energy loss in Neon gas would be 2.71 keV cm^{-1}. The thickness of the first ionization gap is 11 mm, leading to an average energy loss of the MIPs is 3.0 keV. In a thin layer of material, like the Neon gas in the first ionization gap, the total energy-loss distribution of a traversing charged particle is determined by a small amount

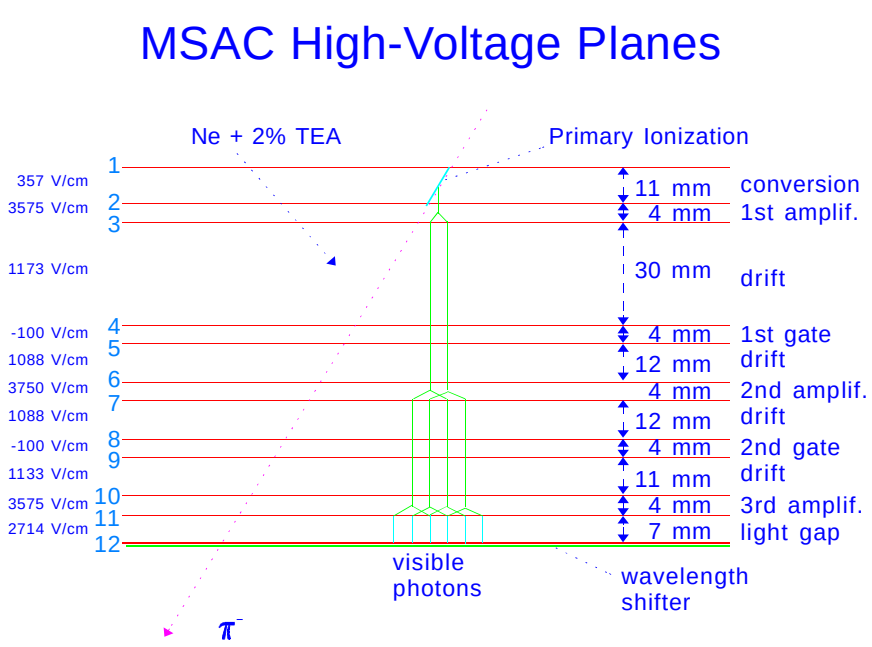

Figure 3.3: *Side view of the meshes in a MSAC chamber.*

of interactions. The interaction of the charged particles is characterized by large fluctuations in a wide range of energy transfer. The energy loss distribution of the hits in the gap can theoretically be described by a Landau distribution [68]. The Landau distribution is asymmetric and has a high energy tail, caused by close collisions between the crossing charged particles and the gas electrons. The amount of primary ionization can largely fluctuate due to this distribution. The average amount of energy lost for 1 ion-electron pair is 36 eV for Ne. Therefore, about $3000/36 = 80$ ion-electron pairs will be created on average.

The small electron cloud drifts under the influence of the applied E-field into the amplification gap of 4 mm. In this first-stage amplification the number of electrons is increased by a factor of $10^4 - 10^5$. This multiplication in gas detectors occurs, when the primary ionization electrons gain sufficient energy from the accelerating field to further ionize the gas atoms and is described by

$$M = \frac{e^{\alpha \cdot d}}{1 - \gamma \cdot (e^{\alpha \cdot d} - 1)} \tag{3.3}$$

where $\alpha(p, T, E)$ is the Townsend coefficient which depends on the pressure p, the temperature T, and the average ionization energy E of the gas. The factor γ takes into account the effect of positive ions hitting the cathode wire and creating electrons due to the photoelectric effect, and is usually small. Although the multiplication, as described by the above formula, seems to rise without limit, in reality at multiplications of 10^8 breakdowns due to the creation of a plasma column occur.

The electron cloud passes into a drift gap. Diffusion of the electrons in this gap, reducing the charge density, prevents breakdown in further stages. Furthermore, the image is stored, using the typical electron drift time of about 1 μs, allowing the trigger logic to decide, whether or not to open the 4 mm gate gap. Normally the gate gap is biased by a reverse voltage of 50 V. The trigger generates with a delay of 0.7 μs and gate width of 800 ns a 300 V opening pulse for the gate gap (the drift speed of electrons is 3.2 $cm/\mu s$ in saturation).

The operation of the MSAC in trigger mode has the advantage that unnecessary discharges, e.g. due to cosmic radiation, do not occur. This prevents positive-charge buildup and, with respect to the mentioned subject of sparking, improves the performance. After the first gate the electrons enter a 12 mm drift gap with drift time $\approx 0.5 - 1.0\ \mu s$. The transfer into these weaker fields leads to an electron loss by a factor $E_{ampl}/E_{drift} \approx 5$. Another 4 mm amplification gap, a 12 mm drift gap and a 4 mm gate gap follow. This second gate is triggered 1.6 μs after the event and has a gate width of 800 ns. Another 11 mm drift gap and 4 mm amplification gap follow. Directly after this amplification gap the 7 mm light gap has been placed to maximize the number of emitted photons by excited TEA molecules [70, 71, 72, 73]. TEA is a very good quencher due to 2 electrons which are easily excited and de-excite by emitting UV light. Both excitation and recombination and thus light emission do not occur in intense electric fields. The main four orders of magnitude of the light intensity originate from the light gap where the electric field is lower. Here, the mechanism of excitation of TEA gas molecules prevails over ionization of the Ne gas atoms. To adapt the emitted light spectrum, peaked at 280 nm, to the sensitivity peaked at 400 nm of the CCD-camera a 1 mm thick wavelength shifter absorbs the UV light and re-emits it in the blue range of the spectrum. The number of isotropically emitted photons is about 10^6. The photons are reflected, via aluminized mylar foil mirrors, positioned at 45° with respect to the chamber surface, into the solid angle of the CCD cameras.

The MSAC chambers are constantly flushed with a mixture of Neon and TEA. TEA is a poisonous gas and highly inflammable. It is kept liquid at 0°

C. The refilling of TEA takes place under strong security precautions. Both rubber gloves and gas masks have to be worn. By bubbling Neon through the TEA liquid a mixture of Neon and 2% TEA is fed into the chambers.

Each chamber has an entrance and an exit window consisting of two 50 μm thick mylar foils 10 mm apart with a constant Ar gas flow in between. This shielding prevents air from entering the chamber, which would disable proper operation.

3.10.2 Optical Readout

Signals from each chamber are optically read out by two image intensified CCD cameras. In front of the CCD chip of 288×385 pixels, each having 6 intensity-bits, two image intensifiers amplify the light signal. The first image intensifier is a micro-channel plate, where light falling on a S25 photocathode is converted into electrons. Each 18 mm long micro-channel is a metal coated glass channel placed under an angle with respect to the applied $E-$field of 9 kV. The electrons will, by bouncing through a channel, multiply by liberating electrons from the metal coating. The electrons are directed to a fast phosphor screen. The emitted photons enter a de-magnifying electrostatic image intensifier used as an active taper, to reduce the image by a factor 1.7. The emitted light shines on the CCD Image Sensor. This analog circuit converts the optical image into electronic output. Each element (pixel) consists of a voltage gated np-junction (Photo MOS/ Photo Diode). The light will create electron-hole pairs in the p-type material. The electrons travel to the n-type material under the applied gate-voltage. Here, the accumulated photo-charges are stored after which these charges are read out as a voltage signal which is amplified and finally digitized. The CCD data, containing 18 bit position and 6-bit ADC value information, are stored using 24-bit words into Memory-CCD processors. Each MCCD processor has 2 memories, A and B, each of 1 Mb size. Certain thresholds (pedestal values) for the pictures are set (ADC level, maximum number of pixels) to reduce the final data rate. The filtered information is stored through a VSB bus into FIC 8230 processors (operating under OS9); see section 3.11 and figure 3.4. Between the effective spills the data are accessed via VME by the main acquisition system. The allowed event rate is 50 Hz.

3.10.3 The Light Monitoring System

Like all detectors the MSAC chambers have operation limitations. First of all, they are influenced by weather conditions. The atmospheric pressure

and temperature have an effect on the electron multiplication. Moisture in the air causes gas ionization on the edges of the chambers. A third tendency of the chambers is to have complete breakdown, i.e. sparking.

The light output of the chambers is automatically controlled by the following monitoring system. A ^{90}Sr (Strontium) β^- source (0.5 MeV and 2.1 MeV) is placed on one side of the chamber. Each time that a scintillator equipped with a trigger photomultiplier on the other side of the chamber measures an electron, another photomultiplier measures the light output of the chamber. If the light output changes with respect to the reference gain, the voltage across the three amplification gaps, which is typically about 1420 V, is automatically adjusted. The gas breakdown, called corona, due to moisture causes currents to be drawn from the high voltage (HV) supply. This degrades the performance of the chambers and might ruin the chambers, due to fire hazard. This effect disappears by lowering the HV or shutting down the chamber. Giving the chamber an extra layer of insulating paint does only solve the problem temporarily. In the follow-up experiment WA98 the coronas have not been observed.

Sparking of MSAC chambers is an effect which has been known for a number of years. It degrades their performance enormously, because after each breakdown the HV has to run up to its previous value. The dead-time due to this effect was about 500 ms. By the application of zener-diodes the dead-time could be reduced to about 200 – 250 ms. The zener-diodes drain the excessive charge each time there is a spark, thus facilitating the recovery of the HV-level. Sparking for MSAC's is related to the very high electron density in an avalanche. The multiplication is of the order 10^8. This is the region where breakdown is known to occur. Most likely highly ionizing particles or fluctuations of the primary ionization, due to the Landau distribution, cause the electron densities to exceed the breakdown limit. The high electron density causes a plasma column that locally increases the field. Breakdown due to VUV emission, related to recombination of fragmented hydrocarbons, does not seem to be important for PPAC chambers. The VUV light is known to ionize the gas locally. This kind of ionization is also a function of the electric field, as has been observed for multi-wire and proportional chambers [72, 74].

In the MSAC monitoring system a "spark photomultiplier" measuring the light flash warns the operator to adjust the voltage in case of excessive sparking. The maximum tolerable amount of sparking in the WA93 experiment, for a particle flux of about 40 particles per chamber, was set to about 10 % sparking probability per chamber per burst of about 100 events.

3.11 Data-Acquisition System

The signals from the detectors are digitized in the experiment for each event in modules residing in CAMAC, Fastbus and VME. The modules are communicating in a VME multiprocessing system running the OS9 operating system. One CPU, an ELTEC E6, acts as the main event builder and synchronizes the readout of the others. In case of a period of no effective spill or a full memory module, the data from the 10 E6 and 3 CES FIC8232 are fetched by the event builder and written to video 8 mm tapes, with a capacity of 2 Gb using Exabyte 8500 tape drives. The respective CPU's perform pedestal subtraction and zero suppression in order to reduce the data stream. A schematic drawing of the MSAC data-acquisition system is shown in figure 3.4. The whole process is monitored by the online program

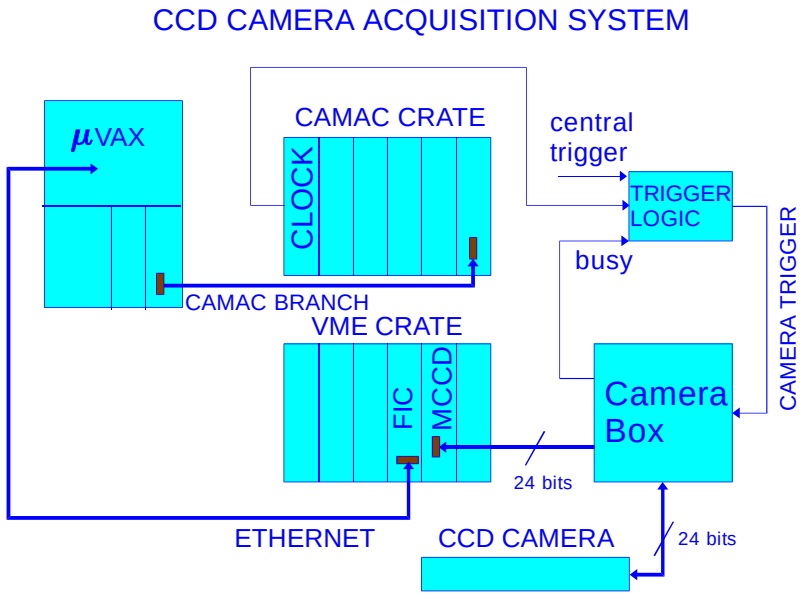

Figure 3.4: *Data-acquisition system for the MSAC chambers. From the FIC the data is transported to the event builder in the main data-acquisition system.*

MONA running on a VAX host computer. From here the process of data

taking can be altered, stopped and started. Warnings from the respective modules are displayed in case user intervention is needed. Using an Ethernet connection to the main event builder, the data stored in a ring buffer can be partially retrieved to workstations. Spectra are studied here to insure that the detectors are functioning properly.

3.12 PAD Chamber

The CCD camera readout system was found to have several severe limitations:

- The MSAC chambers have to yield about 10^7 electrons in order to achieve a large enough light output of 10^7 photons detectable by the CCD cameras. Breakdown due to the Landau tail of the distribution for the electron yield is likely to occur.
- Sparking yields a dead time of the high voltage system of about 250 ms, thus reducing the efficiency of the tracking system.
- The CCD cameras operate at the limit of their sensitivity. There are indications that on the outer parts of the chambers the cameras are less efficient.
- The CCD cameras are limited in their readout speed to 50 Hz and can not keep up with the 1000 Hz data taking rate of the other detectors in the experiment.
- There are indications that satellite hits, see section 4.3, can be related to either the behaviour of the CCD chip or multiple avalanches in the MSAC chamber.

An improved readout method was developed for the WA98 setup. The method consists of directly measuring the charge resulting from the avalanche multiplication. Copper elements, pads of 1×16 mm^2, are used to cover the back plane of the MSAC with 1.2×0.8 m^2 surface. The resulting amount of 57360 pads are read out at high speed allowing the data to be present in VME after 1 ms.

A special chip with 16 pad inputs was designed; see figure 3.5. The chip contains 16 charge-integrating amplifiers (0.5 V/pC). The amplifiers are gated by a 100 ns trigger and feed their output to both an analog 16 fold multiplexer and a summed trigger. A non-linear amplifier, gain = 6, feeds the outputs to a flash ADC. The converted signals are stored into

7-bits wide and 16 words deep FIFO buffer (6-bits data + 1 parity bit). The total time to convert all 16 channels is designed to be 16 times 2 μs. Subsequently the digitized signal data will be shifted via a bus line between the connected FIFO's into the memory of a Digital Signal Processor (DSP 2101) at the clock speed of 12.5 MHz. In the chip design the digitized part

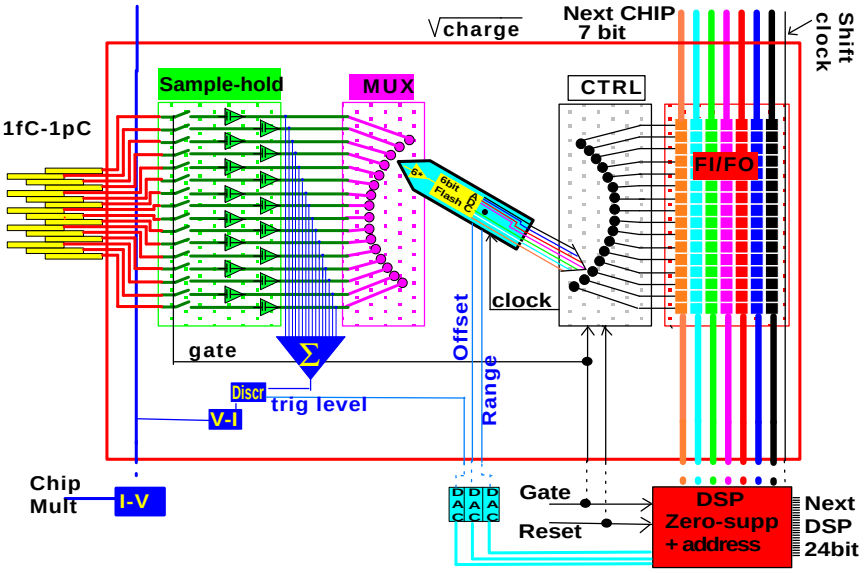

Figure 3.5: *Layout of charge-sensitive chip, with the analog part at the left and the digital part at the right. The analog signal is converted by a 6-bits flash ADC in the middle.*

has been separated from the analog part. The chip surface area is $\approx$ 14 mm^2 which is $\approx$ 6% of the total PAD area. The dissipation will be 25 mW of which the analog part contributes 20 mW and the digital part 5 mW. The maximum temperature under which the chip can operate is 80 °C. An estimate of the temperature, using Stefan-Boltzmann black-body radiation temperature, assuming the heat, dissipated by the chips to be uniformly spread over the PAD plane, yields 36.2 °C. This temperature rise has been experimentally verified.

The construction of the PAD chamber consists of two stages of amplification, having a similar design as the MSAC chamber, with the addition of a special drift gap and Faraday cage for the PAD plane. The PAD chamber,

see figure 3.6, has a size of 1200 mm by 800 mm (inner dimensions). The PAD plane is covered by 25 boards, 48 mm wide and 800 mm long. Each board has 3 chains of 48 chips each reading 16 horizontally staggered pads. Each chain of 768 pads is read out by 1 DSP (total number of DSP's 75). The vertical bus contains 7 data bits, reset and clock signals, analog ADC levels and the gate signal. The DSP will perform zero suppression. It is

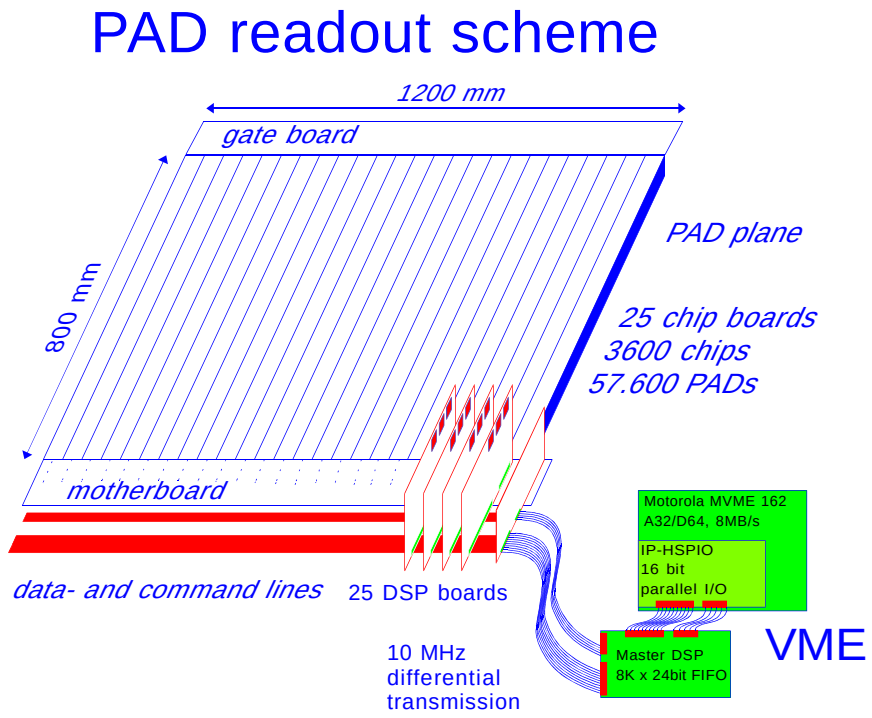

Figure 3.6: *Layout of the pad chamber. The twenty-five chip boards are read by twenty-five DSP boards mounted on the mother board.*

expected that at most an occupancy of 4 % of the total amount of pads will be measured. This data is shifted to a FIFO buffer on the DSP board and in case all data have been processed the DSP signals that it is ready. If all the DSP's have signaled to be ready the transceiver card on the mother board, containing all the DSP's board, shifts the data from the 75 DSP's to the VME board containing an 8 Kb (24 bit) FIFO buffer, a master DSP and a VME processor. As long as the FIFO on VME has enough memory space

the transceiver keeps sending the data. When all the data have been read-out the VME processor starts a DMA transfer to a VME memory module containing a Motorola processor. The main event builder running on an E7 processor can fetch them whenever this memory module is running out of space. The performance of a test PAD readout system has been measured [75] yielding a lower limit of 94 % efficiency of the chamber.

3.13 Summary

In the previous sections the WA93 setup has been described. The basic aim of the WA93 experiment is the measurement of the direct photons together with knowledge of the space-time evolution from the measurement of negatively charged particles. The experiment was developed and performed by an international collaboration of institutes. Each institute was involved with one or several of the detectors. The author was, as a member of the KVI Groningen team together with the teams from the University of Lund and the University of Geneva, particularly involved with the charged-particle spectrometer. The MSAC chambers were developed and built by the University of Geneva. Participation in the construction, testing and operation of these chambers gave particular insight into the performance characteristics of these sensitive devices. The sparking problem for the WA93 experiment could partly be solved by the implementation of zener diodes.

The development and testing of the prototype PAD chamber for the WA98 experiment was done together with the University of Lund and involving the companies CTI Groningen for the development of the DSP readout and Sicon Linköping for the design of the VLSI chip. The DSP readout was extensively tested at the KVI. Especially initial malfunctioning problems of the VLSI chip were investigated at the KVI and solved.

Chapter 4

Preprocessing Charged-Particle Spectrometer Data

In this chapter the characteristics of the charged-particle spectrometer and the steps towards extracting the proper data are described. First a transformation from the CCD pixel-frame to the WA93 lab-frame has to be made, see section 4.1, for the alignment of the chambers. In section 4.2, an outline of the necessary software tools is given to study the raw data and to calculate the properties of this tracking system. Selections on cluster-size and cluster-amplitude are made in section 4.3. Proper cuts will be determined to reject tracks which are due to random combinatorics. Furthermore, the detector property of producing satellite clusters surrounding the true particle hit is described, and a method is given to handle this problem. Clusters which pass the above criteria are used as input to the tracking algorithm, as will be discussed in section 4.4. Using a sophisticated "binary-linking" method and restrictive cuts, the particle tracks are reconstructed. Knowing the position and direction of the track the respective momentum components can be retrieved, as shown in section 4.5 on the momentum reconstruction. Here simulations are described which were done to parameterize the momentum components as a function of the position and direction of the track. On their way through the tracking system tracks may undergo several interactions. Extensive Monte-Carlo simulations based on raw data from the event-generator VENUS [76], based on a string-fragmentation model, were done to estimate the momentum resolution of the charged-particle spectrometer. These simulations will be discussed in section 4.6 on the determination

of the momentum resolution. Not all particle tracks are recognized due to the limited efficiency of the chambers. An efficiency estimate based on the raw data was implemented in the simulation code in order to correct the measured single-particle spectra, as shown in section 4.7 on the efficiency calculations. The geometry of the tracking system influences the shape of the measured single-particle spectra. Simulations were done using as input a homogeneous population of phase space in rapidity and transverse momentum in order to correct for this effect, as will be discussed in section 4.8 on the acceptance simulations. Part of the reconstructed tracks are background tracks, consisting of reconstructed tracks not related to negative-pion tracks. Section 4.9 deals with these background calculations. This background distribution has two components, a physical and a random combinatorial one. The physical component, as the tracking system has no π^- particle identification, consists of a fraction of the tracks made by electrons, muons, kaons and anti-protons. Studying central VENUS events an estimate of these fractions can be given. Using correlated hits in three or four chambers, random tracks not related to proper tracks are made. A knowledge of their distribution and their fraction of single-particle spectra is absolutely necessary for the data extraction.

4.1 Alignment of Chambers

A correct alignment of the individual chambers is crucial for proper track measurements. Uncertainties in the positioning directly affect the momentum resolution of the detector [77].

The CCD-pixel information has to be uniquely mapped to the laboratory coordinate system. The track-reconstruction algorithm and the momentum-reconstruction method use these WA93 coordinates as reference frame. Therefore a transformation function for each of the 7 cameras, incorporating their relative position with respect to the chambers, has to be found. The alignment is based on 60 reflecting fiducial marks distributed over the chamber surface attached to the spacers. The position of the spacers in lab coordinates is known exactly within 0.1 mm. The fiducial position is measured as follows. Intense blue light is shone on the chambers. The light reflecting from the 1 cm $\oslash$ fiducial marks is detected by the CCD camera. A filter of factor 4000 consisting of a layer of glass (factor 2) a layer of gelatine (factor 10) a layer of glass (factor 100) and another layer of glass (factor 2) prevents the sensitive cameras from being damaged by this intense calibration light. The accumulated set of 2-dimensional CCD-frame

coordinates (X_{CCD},Y_{CCD}) is parameterized for each camera i ($1 \leq i \leq 7$) according to

$$X_{LAB}(i) = A(i) + B(i) \cdot X_{CCD} + C(i) \cdot Y_{CCD} \quad (4.1)$$

$$Y_{LAB}(i) = D(i) + E(i) \cdot Y_{CCD} + F(i) \cdot X_{CCD} \quad (4.2)$$

in order to obtain the lab coordinates (X_{LAB},Y_{LAB}). Data have been accumulated both for field on and off as the magnetic field slightly distorts the image of the CCD cameras, although the cameras were shielded using mu-metal. Unfortunately due to difficult illumination conditions for the complete chamber surface not all the fiducials were detected by the cameras. Usually about 30 to 50 % of the fiducials were found. The reasons for this are the positioning of the fiducials behind the wavelength shifter and the loss of sensitivity of the cameras on the edges. The symmetric spacing of the fiducials made the pattern recognition, uniquely linking CCD points to respective lab points, difficult.

The fiducial marks were roughly identified in a 20×20 pixels window. Some of the selected points were either not corresponding to a fiducial mark or their estimated maximum was several pixels ($\approx$ 1cm) from the correct position. However, knowing the spacing of the fiducials the identified fiducial marks were used as input to check every likely position for fiducial peaks in the 288×385 pixel plot. Via this method extra fiducial points could safely be added. The exact position was found by fitting a two-dimensional function containing a background level, a linear term and a gaussian term, see figure 4.1.

The traced points are then used as input to the fitting routine which maps them making use of a linear equation. The position can be determined with an accuracy of about 3 mm which corresponds to an angular uncertainty of about 0.7 mrad with respect to the target. Worst-case identification of pixels on the edge of view of the cameras may be about 1 cm off.

The cameras were subsequently aligned with respect to the chamber planes. Comparing the alignment results from different cameras for straight particle tracks passing through several chambers revealed a residual maximum linear misalignment of 1 cm, which was corrected based on the analysis of straight particle tracks measured with the magnetic field off. The fourth chamber (at the largest distance) was used as a reference plane. In this way the influence of a possible misalignment of this chamber is minimized due to the long lever arm. The target position and a track point in the fourth chamber define a straight line through the remaining three chambers. The distance between this line and clusters nearby shows the effect of the misalignment.

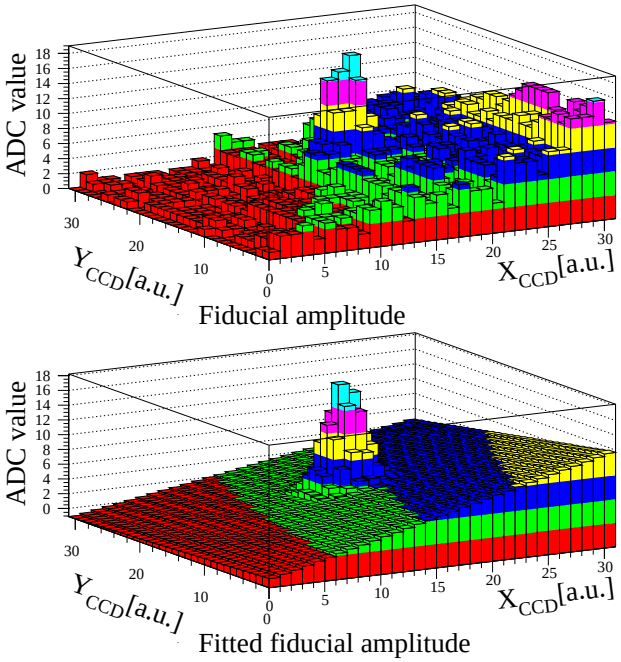

Figure 4.1: *Fiducial fitting. The upper figure shows the measured signal height ADC of a fiducial mark in the CCD-pixel frame (X_{CCD}, Y_{CCD}). The lower figure shows the result of the two-dimensional fit to this measured signal height.*

Background subtraction was done using event mixing. From figure 4.2 showing the final alignment in the horizontal x direction for camera 1 an accuracy of $\sigma \approx 0.6$ cm is determined. A further fine-tuning using raw data, where the positions of the spacers are seen as inefficient areas for particle tracks, yielded a final set of parameters. The position of the tracks at the target for field off is shown in figure 4.3, see also [62]. The spatial resolution was estimated from the distribution of the distance of tracks to nearby clusters and yielded 3.4 mm.

4.2 The Analysis and Simulation Packages

In this section a description of the analysis package and the simulation package for the WA93 setup will be given. The analysis packages were written in FORTRAN in a PATCHY [78] format. The code consists of patches and

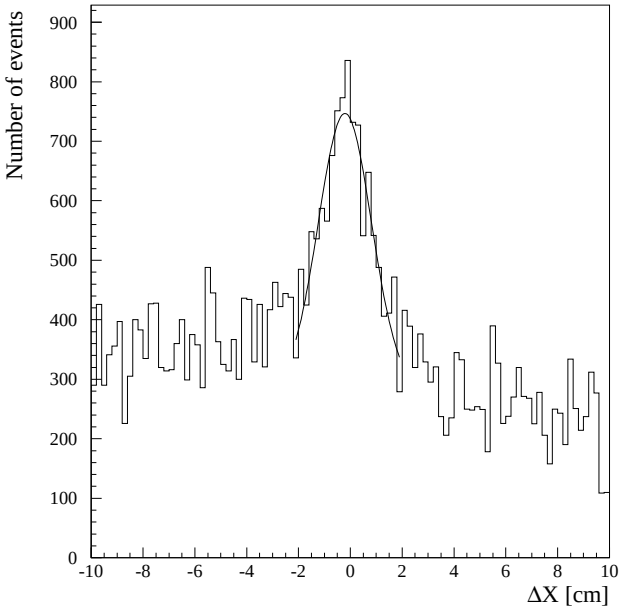

Figure 4.2: *Alignment of camera 1 with magnetic field on.*

decks. Patches contain the code for the respective detectors whereas decks are the subroutines for a specific detector. The power of PATCHY lies in the fact that each user can replace in a separate file, called "cradle", parts of the code for test purposes. In case the tests were successful a new version was distributed among the groups constituting the WA93 collaboration. Graphic representation of the data was enabled using HBOOK [79] and PAW [80]. Histograms and Ntuples, N-dimensional arrays of data, are "booked" and "filled" using HBOOK routines. In PAW these histograms can be displayed and, in case of Ntuples, selections can be made. An overview of the inputs and outputs of the analysis and simulation codes is given in figure 4.4.

4.2.1 WA93 Analysis Package

The raw experimental data were stored on "exabyte" tapes. In the off-line analysis the different detectors can be activated for a specialized analysis of particular detector groups. In a first stage data are retrieved and operations like removing noise, clustering, and tracking are performed. In the second-stage the physics observables, like angles and momenta, are calculated and stored in a Data Summary Tape format. These DST's are used for the final

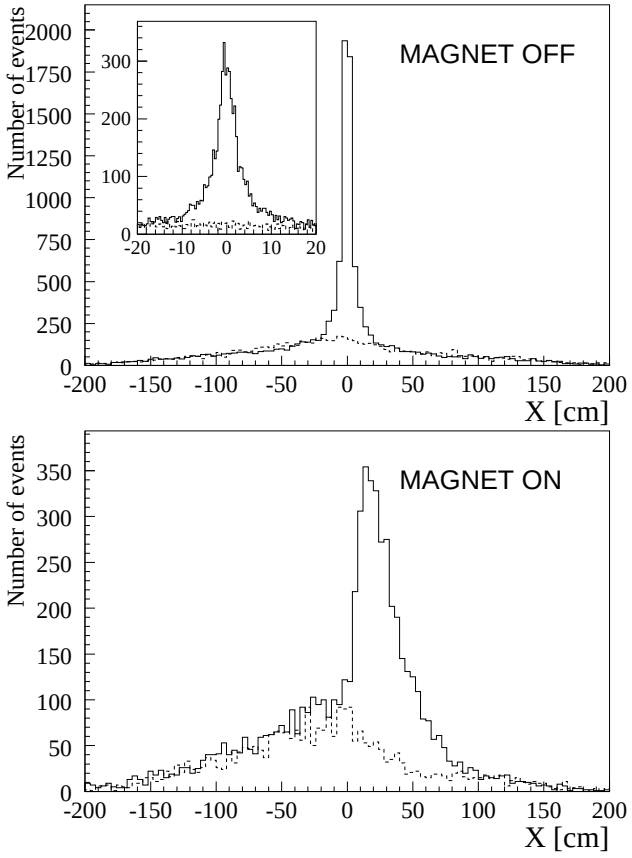

Figure 4.3: *Track distribution in the horizontal plane at the target position ($z = 0$). The dotted lines show the calculated background contribution due to random combinatorics.*

physics analysis, see figure 4.4.

For the MSAC chambers the data are retrieved in routine E3DECO. The parameter cuts for the clustering are specified in routine E3INIT. Using the alignment parameters defined in routine E3PARM, reconstructed hits are mapped to the WA93 lab-system and written to DST data banks. At the stage of tracking they are retrieved in routine EAHITS. Track segments are combined to form three or four chamber tracks in routines EASEGM and EATSEL. Constructed tracks are written in the DST tracking banks. In the second-stage analysis these tracks are used as input for the momentum reconstruction routine EAGETP($x_2, y_2, x_3, y_3, P, P_x, P_y, P_z$), see figure 4.12.

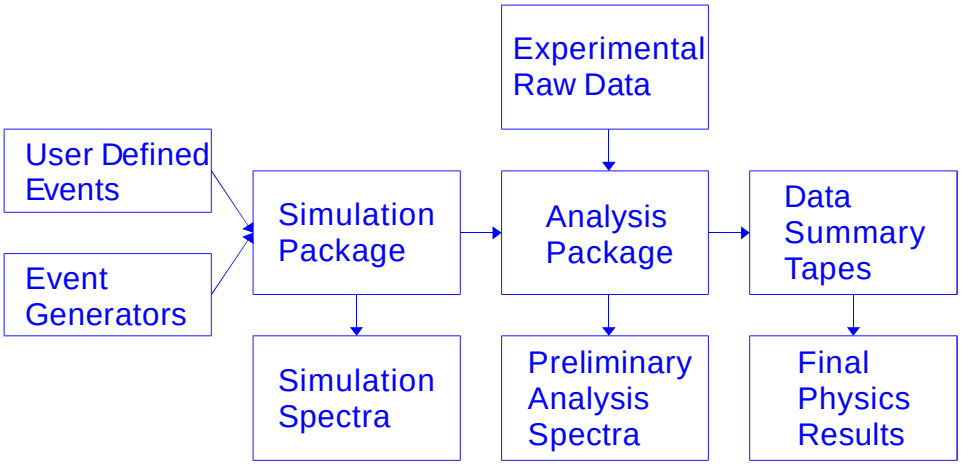

Figure 4.4: *Overview of inputs and outputs to the analysis and simulation codes.*

This routine gives according to the previously described method the momentum and its directional components. The reconstructed momenta are written to a file in DST format for further analysis.

4.2.2 WA93 Simulation Package

The simulation code for the WA93 setup was based on GEANT [81]. The geometry and material contents of each detector were specified in detail and GEANT contains sets of parameters to calculate electromagnetic and hadronic interactions for a broad spectrum of energies and particles.

As input to a GEANT simulation of the setup either event generators (VENUS [76], RQMD [82], FRITIOF [83]) or user-defined events are used. These mentioned event generators are based on string fragmentation models. Interactions between two nucleons occur whenever they come closer than some minimal distance. The result of the interaction is a longitudinally oriented object called a 'string'. The string may be formed either via momentum exchange, FRITIOF and RQMD employ this mechanism, or via colour exchange, VENUS employs this mechanism. The resulting strings are quite similar. After a certain time the strings fragment. The interaction of the produced particles is then closely tied to the concept of a "formation time'. During this time the particles can not interact. Whereas VENUS includes constant cross-sections for quark-hadron and hadron-hadron inter-

actions, RQMD employs the cross-sections and decay probabilities of the produced particles. Many of the calculated observables from the various models are very similar.

A typical central S + Au event is shown for negatively charged particles in the charged-particle spectrometer in figure 4.5. Particle densities can be

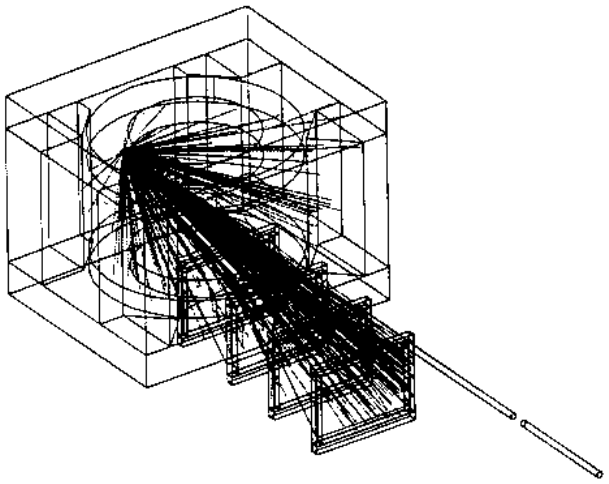

Figure 4.5: *VENUS simulation of a central S + Au collision for negatively charged particles in the WA93 charged-particle spectrometer.*

estimated and the design or position of a detector can be tailored accordingly before the experiment is carried out. Treating the simulated hit positions as experimental raw data the analysis code can be checked for correctness. Also the momentum resolution, acceptance, efficiency correction and background contamination for the detector system can be calculated. In the simulation the magnetic field setting of Goliath can be switched on and off.

As the Goliath magnetic field is not strictly a homogeneous field, it was imperative to measure the three magnetic field components. In July 1991 the field distribution corresponding to an average $\int \vec{B} \cdot \vec{dl} = 2$ Tm was mapped. The pole width as defined by the outer diameter of the coils is 240 cm and the pole gap is 160 cm. The current is fed through a lower Cu coil of 216 turns and an upper Al coil of 216 turns. The maximum currents that can be used are 3300 A and 4800 A for the Al and Cu coil, respectively. The settings for the 2 Tm field were 2827 A and 4448 A,

respectively. The magnetic field was mapped using a field probe with 4×3 Hall-plates mounted such that the three components were measured at four points simultaneously. The cell size in x, y and z was 4 cm, 4 cm and 2 cm, respectively. Both the main field and the fringe field, outside the magnet, were measured.

A fast three-dimensional linear interpolation method using the stored field map as input was implemented for the GEANT simulation. The one-dimensional case is depicted in figure 4.6. The task is to determine the function value for the variable x, knowing the function values at the neighboring positions x_i and x_{i+1}

$$f(x) = f(x_i + p \cdot h) = (1-p) \cdot f(x_i) + p \cdot f(x_{i+1}) \tag{4.3}$$

where $p = \frac{x - x_i}{x_{i+1} - x_i}$. In the three dimensional case we get

$$\begin{aligned} f(x,y,z) = \quad & (1-p)\cdot(1-q)\cdot(1-r)\cdot f_{000} + p\cdot(1-q)\cdot(1-r)\cdot f_{100} \\ & +(1-p)\cdot q\cdot(1-r)\cdot f_{010} + (1-p)\cdot(1-q)\cdot r\cdot f_{001} \\ & +p\cdot q\cdot(1-r)\cdot f_{110} + p\cdot(1-q)\cdot r\cdot f_{101} \\ & +(1-p)\cdot q\cdot r\cdot f_{011} + p\cdot q\cdot r\cdot f_{111} \end{aligned} \tag{4.4}$$

Using the above formula the respective magnetic field components $B_x(x,y,z)$, $B_y(x,y,z)$ and $B_z(x,y,z)$ can be rapidly approximated. An enormous number of about 300.000 field points has been acquired. The data analysis would be very slow in case the tracks are traced for each event back to the target using the above interpolation algorithm for the magnetic field. Therefore it was decided to parameterize the momentum components of tracks using the hit position and direction of the tracks. Thus only a limited number of interpolations was necessary, see section 4.5 on the momentum reconstruction.

4.3 Cluster Analysis

Clustering of the signal heights measured by detector modules is common practise in the field of nuclear physics [84]. Energy, position and kind of particle may be measured. Sometimes only one of these is of interest. The trade off between demands on good energy resolution and good position resolution determines the detector design. For the MSAC chambers a good position resolution is required. Particle identification based on the total amount of charge in the electron-avalanche in the chamber is ruled out due to the Landau distribution of the energy loss; see section 3.10.1. The WA98

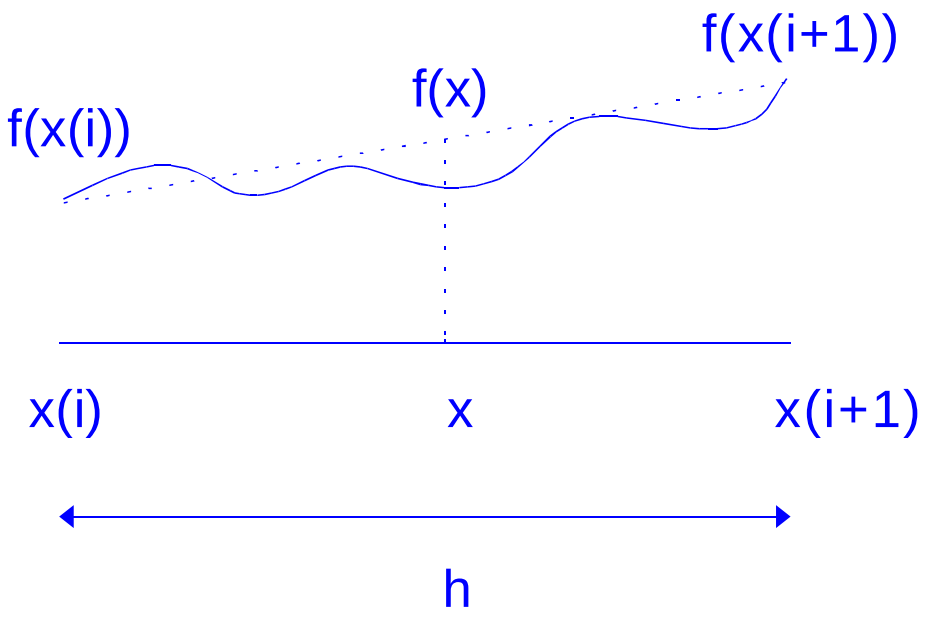

Figure 4.6: *One-dimensional linear interpolation.*

upgrade, however, allows particle identification by measuring the time of flight.

The 288×385 pixels of the CCD cameras contain 6 bit ADC information and represent each a 3×3 mm^2 surface element of a MSAC chamber. The applied clustering method is based on an ADC-weighted nearest neighbourhood method:

$$\bar{X} = \frac{\sum_{i=1}^{N} A_i \cdot X_i}{\sum_{i=1}^{N} A_i} \tag{4.5}$$

$$\sigma_X^2 = \frac{\sum_{i=1}^{N} (X_i - \bar{X})^2}{N-1} \tag{4.6}$$

where X_i is the horizontal position of pixel i in the WA93 frame, N is the number of pixels in the cluster, A_i the ADC-signal height of a pixel and σ_X the width of the cluster. Analogously the average vertical position $\bar{Y}$ and width σ_Y can be defined. The information of the number of pixels, the total cluster ADC-sum and its width are later used to determine, whether or not to use this cluster. The cuts for the clustering are chosen such as to

minimize the number of background hits and still keep a reasonable tracking efficiency. Unfortunately it was not possible to set a straightforward threshold on the ADC-signal height due to the earlier-mentioned problems like sparking, corona's and gain fluctuations. However, a constant threshold of 4 was set for the pixel ADC-signal height to be sure to cut out noise, since the pixel ADC's are already corrected for their specific pedestal value set in the MCCD, see section 3.10.2. In order to study only events where the chamber had recovered from a spark, the dead time of 250 ms of the HV power supply was taken into account after such an event, using the available information on the spill clock in the data analysis.

Adjusting the minimum number of pixels per cluster clearly showed that the width of the track distribution for field-off data narrowed significantly when demanding more than 3 pixels per cluster; see figure 4.3. Furthermore, a minimum value of 19 was set for the summed ADC of a cluster. These values were chosen in order to reduce the combinatorial background in the tracking.

The reconstructed hits are mapped to the WA93 lab system using the alignment parameters. As this concerns a linear transformation the order of clustering and mapping is of no concern. Using the thus-obtained set of clusters it was found that satellite clusters show up. These may be created by either stray electrons or photons from the primary avalanche or from a back-splash of electrons in the CCD camera chip. Satellites dramatically enhance the number of found clusters and therefore lead to random tracks. The size and ADC-values of the satellite clusters is not different from typical true clusters; see figure 4.7. Therefore it was decided to study the extent of this effect, i.e. the distance from a track up to which the enhancement of accompanying tracks can be seen; see figures 4.8 and 4.9.

The two-track distance was determined using the measured events and an event mixing procedure. Up to a distance of 8 cm the effect of satellites was noticed. In the correlation studies this value was taken as the minimum distance for two tracks to be valid.

4.4 Tracking

In high-energy and nuclear physics the detection of the paths of many charged particles in devices like bubble, streamer, time-projection and MSAC chambers is a common problem [77, 85, 86]. In the MSAC tracking system multiplicities of up to several hundreds of clusters per chamber are measured. A fast tracking routine was needed which limited the number of

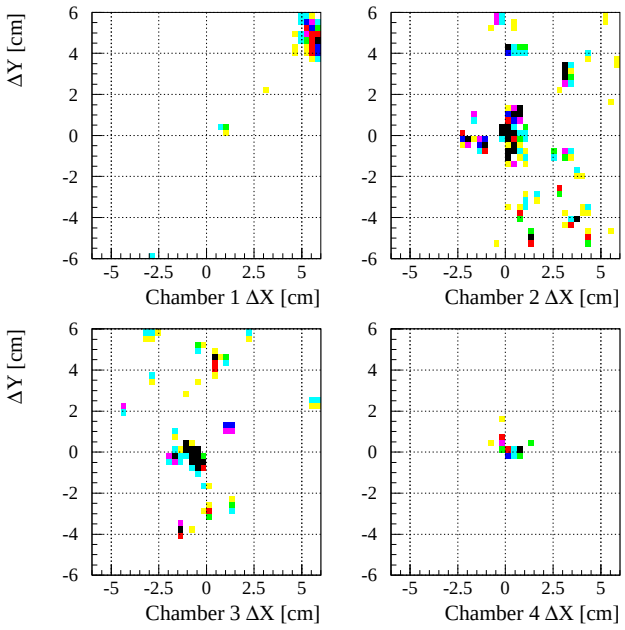

Figure 4.7: *Clusters at the position of a track at (0,0).*

combinatorial tracks.

At the stage of track reconstruction in the data-analysis package the information about the position, the number of pixels, and the total ADC pulse height and width of the hits is retrieved. The hits are then combined for the four chambers according to a "binary linking" method which is explained below [87]. Track segments are set up for all combinations of two-cluster points in two different chambers. The track segments were required to fulfill the criterium of pointing back to the target position within $\pm$ 5 cm in the y direction otherwise these segments are ignored. The track segments are combined to tracks using three or four chambers in case the tracks, consisting of the combination of, respectively, two or three segments, fulfill the following criteria. The tracks have to point to the target within $\pm$ 2.5 cm in the y direction. Note that even without interactions, like multiple scattering, the particle tracks will no longer point exactly to y = 0 due to their curvature in the magnet. A broadening of the effective target size by about 1 cm was estimated from simulations. Furthermore, the tracks have to fulfill a χ^2 per degree of freedom of less than 2.5. In this procedure each hit is weighted

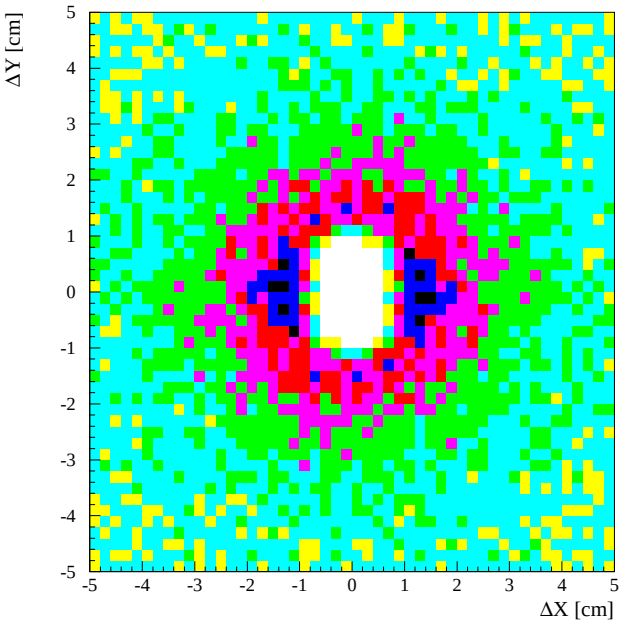

Figure 4.8: *Two-cluster distance. A dark ring structure originating from the satellite enhancement can be recognized. The white region represents the closest distance between the clusters due to the limited pixel and cluster size.*

according to

$$w_{x/y} = \sqrt{\frac{ADC_{TOT}}{\sigma^2_{x/y} \cdot 30}} \tag{4.7}$$

where ADC_{TOT} is the ADC signal summed over one cluster, in order to favour narrow high-intensity clusters. Constructed tracks are written into the DST tracking banks.

4.5 Momentum Reconstruction

In this section the method of the used momentum reconstruction will be described. The reason for choosing a parameterization of the momentum components as a function of position and direction of the tracks was based on the need for having a fast reconstruction algorithm. Tracing back each

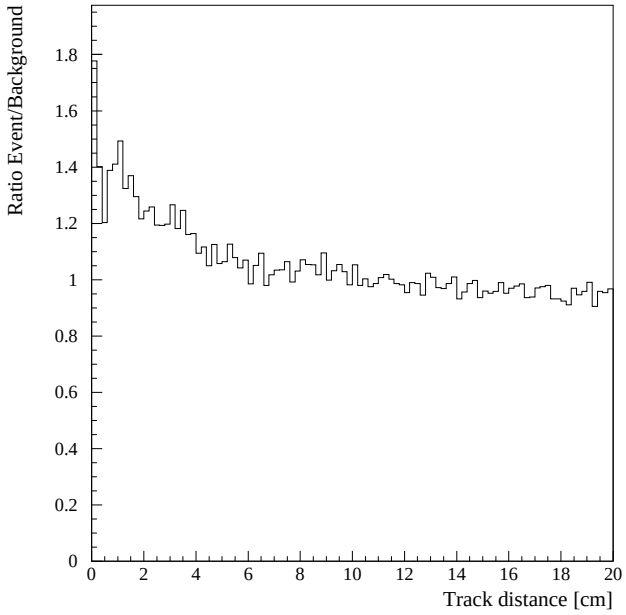

Figure 4.9: *Spatial correlation of adjacent tracks showing the satellite enhancement.*

individual track using the interpolation of the measured field map repeatedly would be a too time-consuming procedure for the data analysis. The requirement for the fast parameterization is a good momentum resolution over the momentum range of interest. The application of Tchebysheff polynomials provides a proper solution as described in the next subsection.

4.5.1 Tchebysheff Parameterization

Tchebysheff polynomials [88] have several useful properties yielding the best possible parameterization over the full range of a certain quantity. These polynomials are defined as

$$T_n(\xi_x) = \cos\left(n \cdot \arccos \xi_x\right) \tag{4.8}$$

where $\xi_x \epsilon [-1, 1]$ and the polynomials have the recursion property

$$T_{n+1}(\xi_x) = 2 \cdot \xi_x \cdot T_n(\xi_x) - T_{n-1} \tag{4.9}$$

The roots of a polynomial $T_n(\xi_x)$ are defined for $i = 1...n$ as

$$\xi_{x_i} = \cos \frac{(2 \cdot i - 1) \cdot \pi}{2 \cdot n} \tag{4.10}$$

Thus, the roots exhibit a closer spacing near $\xi_x = -1$ and $\xi_x = 1$ than for the middle of the interval $[-1, 1]$. Tchebysheff polynomials are orthogonal, which is a useful property

$$\sum_{i=1}^{n} T_j(\xi_{x_i}) \cdot T_k(\xi_{x_i}) = \begin{cases} 0 & j \neq k \neq 0 \\ \frac{1}{2} \cdot n & j = k \neq 0 \\ n & j = k = 0 \end{cases} \tag{4.11}$$

In case a function $f(x)$ of the variable x, is expanded in terms of Tchebysheff polynomials, first the range of the variable $x \, \epsilon \, [a, b]$ has to be mapped onto $\xi_x \, \epsilon \, [-1, 1]$. This yields $x = \frac{a+b}{2} + \frac{b-a}{2} \cdot \xi_x$. In case the function is expanded up to the order N we get

$$f(x) = \sum_{L=0}^{N} c_L \cdot T_L(\xi_x) \tag{4.12}$$

The reason for the use of the Tchebysheff expansion is that these polynomials have the minimum maximum norm ϵ over the range of parameterization compared to any other parameterization of the order N; see figure 4.10. For example in comparison with a Taylor approximation:

- Tchebysheff error: $\epsilon \approx \frac{(x-x_1)\cdot(x-x_2)...(x-x_n)\cdot f^{n'}(x)}{n!}$
- Taylor error: $\epsilon \approx \frac{(x-x_1)^n \cdot f^{n'}(x)}{n!}$

It can be shown [88] that the support points ξ_{x_i} have to be chosen according to the roots of the used polynomials in order to get the smallest possible norm and the best sampling in a wide range of interpolation.

4.5.2 Calculation of Tchebysheff Coefficients

Before the expansion of the momentum components is discussed some necessary definitions have to be given. In figure 4.11 the definition of the respective angles, dip (d), horizontal (h), phi (ϕ) and theta (θ) has been explained for the WA93 lab frame. The following transformation relations hold:

$$\begin{aligned} \tan\phi &= \frac{\tan d}{\sin h} & \cos\theta &= \cos d \cdot \cos h \\ \sin d &= \sin\phi \cdot \sin\theta & \tan h &= \cos\phi \cdot \tan\theta \end{aligned} \tag{4.13}$$

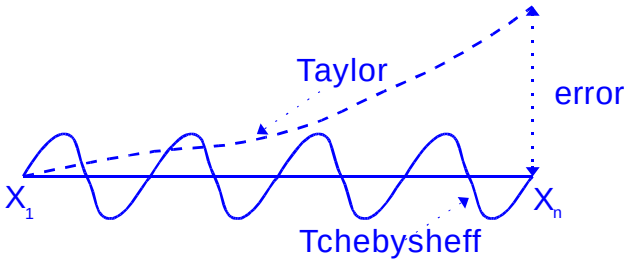

Figure 4.10: *Error using Tchebysheff and Taylor approximation.*

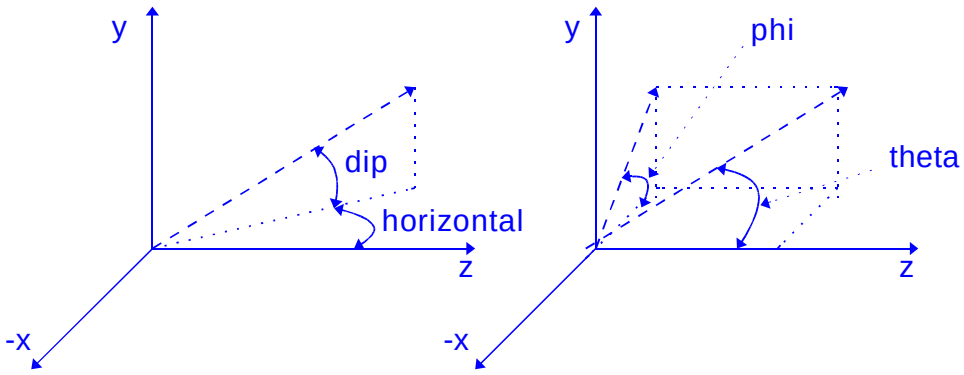

Figure 4.11: *WA93 lab-system displaying dip (d), horizontal (h), phi (ϕ) and theta (θ) angles.*

In order to calculate the magnitude and the angular components of the momentum vector $\vec{P}$ of a particle from its curvature in a magnetic field, one needs to determine five spatial variables. As the particles should originate in the target spot, assuming $x = 0$ and $y = 0$, two of these variables are fixed. So the momentum-vector is described by three variables. The variables are shown in figure 4.12 and determine the hit position of a particle track in a plane defined by the geometry of the third chamber and the angle of incidence at this plane. These variables are sampled according to Tchebysheff roots: 9 points ξ_{x_0} mapping $x_0 \epsilon [2.5, 80]$ cm, 9 points ξ_{x_3} mapping $x_3 \epsilon [-52, -210]$ cm and 8 points ξ_{y_3} mapping $y_3 \epsilon [-60.0, 60.0]$ cm. The limits of the roots ξ_{x_3} and ξ_{y_3} were chosen according to the acceptance of the tracking system and the value of the roots ξ_{x_0} according to the momentum

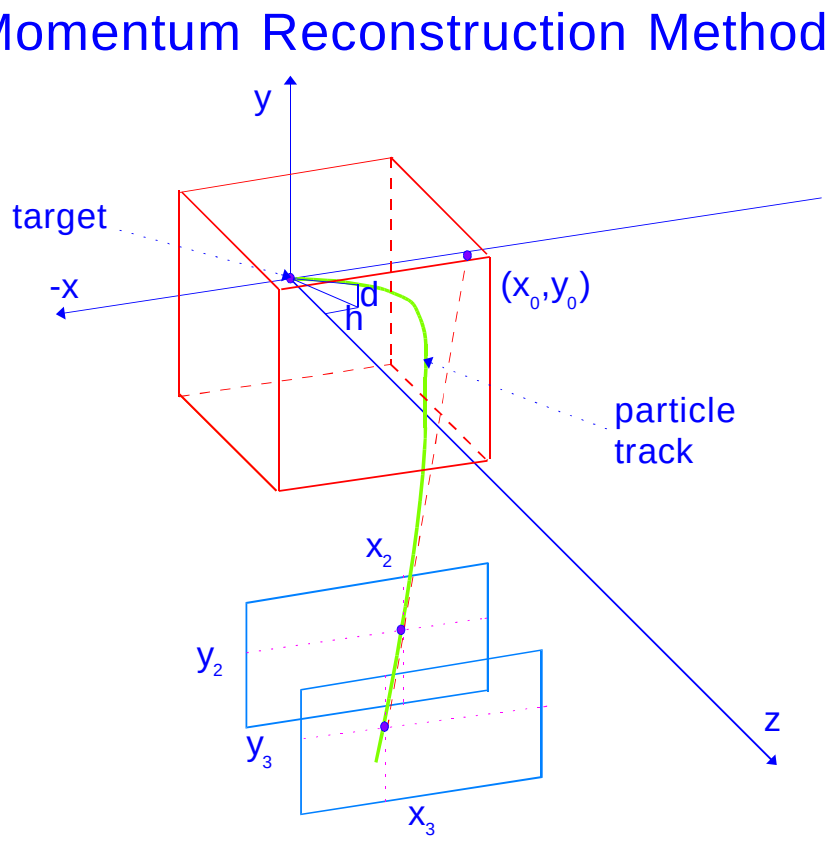

Figure 4.12: *Sampled variables x_0, x_3 and y_3.*

range of interest $1.5 < P < 40$ GeV/c. In order to calculate the momentum components, the reciprocal of the momentum value, as it behaves almost linear with x_0, the dip angle and the horizontal angle are parameterized:

$$1/P = f(x_0, x_3, y_3) \tag{4.14}$$

$$dip = g(x_0, x_3, y_3) \tag{4.15}$$

$$horizontal = h(x_0, x_3, y_3) \tag{4.16}$$

The total number of root points to be generated is $8 \cdot 9 \cdot 9 = 648$. Knowing from simulations the linear dependence between $1/P$ and x_0 and further roughly knowing the momentum kick (0.6 GeV/c) of the magnet an estimate for the starting value of the momentum components can be made. In an

iterative procedure tracks are tracked through the magnetic field using the above-described trilinear interpolation until the specified points (x_0, x_3, y_3) are hit within a user specified accuracy of 0.01cm. Finally a unique set of 648 coordinates $(1/P$,*dip*,*open*,ξ_{x_0},ξ_{x_3}, $\xi_{y_3})$ is obtained. Now one can make use of the orthogonality properties of the polynomials and stepwise calculate the Tchebysheff coefficients for the $1/P$ value, dip and horizontal angles, respectively. For example:

$$1/P = f(x_0) = \sum_{L=0}^{N_{x_0}} c_L \cdot T_L(\xi_{x_0}) \tag{4.17}$$

$$c_K = \frac{\sum_{i=1}^{N_{x_{0i}}} f(x_{0i}) \cdot T_K(\xi_{x_{0i}})}{(N_{x_0}+1) \cdot \frac{1}{2} \cdot N_{x_{0i}}} \tag{4.18}$$

Here N_{x_0} is the order of the polynomial expansion and $N_{x_{0i}}$ the number of Tchebysheff root points. The above-defined coefficients c_K are still depending on the remaining variables (x_3, y_3) so that

$$c_K = f(x_3, y_3) = \sum_{M=0}^{N_{x_3}} \sum_{N=0}^{N_{y_3}} c_{KMN} \cdot T_M(\xi_{x_3}) \cdot T_N(\xi_{y_3}) \tag{4.19}$$

Again, analogous to the one-dimensional case one can project the coefficients yielding

$$c_{KPQ} = \frac{\sum_{j=1}^{N_{x_{3j}}} \sum_{k=1}^{N_{y_{3k}}} c_K \cdot T_P(\xi_{x_{3j}}) \cdot T_Q(\xi_{y_{3k}})}{(N_{x_3}+1) \cdot (N_{y_3}+1) \cdot \frac{1}{2} \cdot N_{x_{3j}} \cdot \frac{1}{2} \cdot N_{y_{3k}}} \tag{4.20}$$

The orders are $N_{y_3} = 7$, $N_{x_3} = 8$ and $N_{x_0} = 8$. The order in y_3 is one lower, as the function in y is even because of mirror symmetry in the zx plane, and the error is defined as

$$\epsilon(x) = \sum_{K=N+1}^{\inf} c_K \cdot T_K(x) \approx c_{N+1} \cdot T_{N+1}(x) \tag{4.21}$$

As it concerns an even function now, the next coefficient c_{N+2} is not zero.

The dip angle and the opening angle have been expanded in a similar way. The only restrictions in the expansions were that the total order of the used polynomials should be less than or equal to 14. This total order suffices for a good description of the momentum components and reduces the number of coefficients.

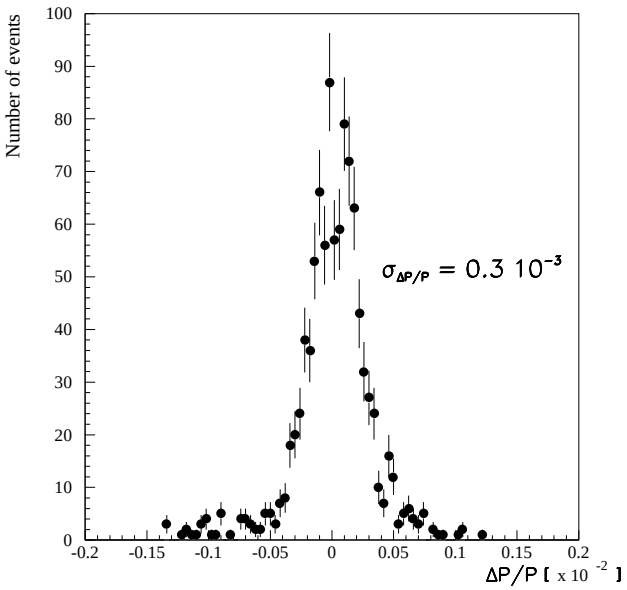

Figure 4.13: *Momentum resolution using the Tchebysheff reconstruction method for random tracks.*

The resolution of the parameterization can be tested using a simulation in which tracks with random momentum components are used. A comparison between the input values $\vec{P}$ and the reconstructed values $\vec{P}'$ of these components yields information on the achieved parameterization momentum resolution $\Delta\vec{P} = \vec{P} - \vec{P}'$. The resolution for the three variables is: $\Delta P/P \approx 0.3\,10^{-3}$, see figure 4.13, $\Delta d/d \approx 0.5\,10^{-3}$ and $\Delta h/h \approx 0.5\,10^{-3}$. The results are satisfactory, as they are by more than one order of magnitude better than the finally obtained momentum resolution. The latter is influenced by particle interactions, e.g. multiple scattering, and limited position resolution, as will be shown in the next section.

4.6 Determination of Momentum Resolution

In the ideal case of a perfect detector and ignoring interactions of the particles of interest with any material between the points of creation and detection we should be able to determine the particle momenta with a resolution as given by the Tchebysheff based reconstruction method.

In section 4.5 these results were presented. However, in reality the events

consist of a high multiplicity of charged particles which may have interactions with the target material, the air, the Si-Drift vertex detector, the yoke of the magnet, the beam pipe, and the wire meshes of the MSAC detectors. This leads to scattered, stopped and created particles which will limit the correct track reconstruction. Furthermore, the MSAC detectors have a limited position resolution.

One should know the influence of all possible disturbing effects to obtain a realistic error of the measured data and a good estimate of the momentum resolution. The binning of the respective momentum and relative-momentum spectra is chosen according to their related momentum resolution. The HBT correlation plots of figure 4.14 show that the relative momentum resolution Q automatically determines the resolving power in the source radius R. Under the assumption of $C_2(\vec{P_1}, \vec{P_2}) = 1 + e^{-\frac{Q_{inv}^2 \cdot R^2}{2}}$ a graph for different source radii can be made. It is obvious that in case

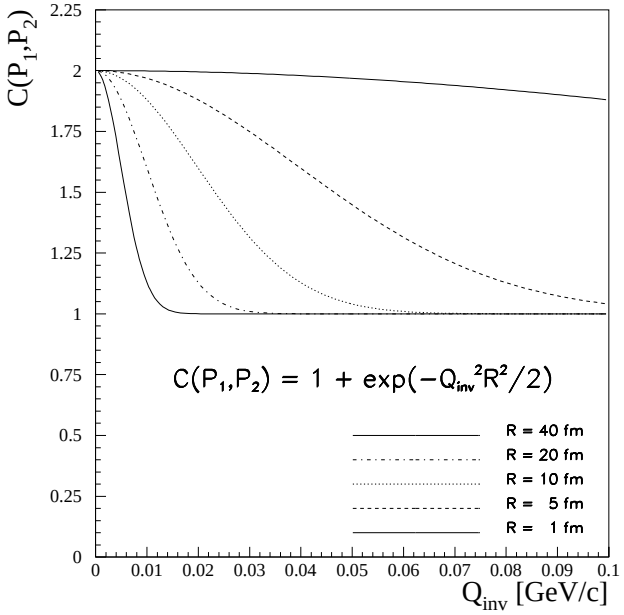

Figure 4.14: *The correlation function for different radii of the source.*

of a Q-resolution of 10 MeV radii of the order of 20 fm and above can not be measured [5]. This is important for future designs of experiments going

from S+Au and Pb+Pb at the SPS to Pb+Pb at the Large Hadron Collider at CERN (LHC) where larger radii are expected to be observed.

In order to obtain a realistic result for the momentum resolution the GEANT package with input events generated by the VENUS string model was used. The VENUS events were calculated for 200 GeV per nucleon S+Au reactions for impact parameters ranging from 0 to 1.0 fm. These are very central and thus high multiplicity events. This situation was chosen as the worst case in order to include the possibility of reconstructing fake tracks. Further, in GEANT the complete setup was defined. Interactions like δ-ray production, hadronic interactions, energy loss, multiple scattering and decay [81, 89], were taken into account.

Multiple scattering causes the major part in the track deviations. Molière scattering was used as the particles may have plural scattering and then molière scattering gives the best description over the whole range of scattering angles. However, running gaussian scattering didn't affect the results. Each VENUS generated event was simulated through the WA93 setup using GEANT. The output consisted of the original momentum components of the particle and the hits in four MSAC planes $(P_x, P_y, P_z, x_i, y_i)$, $1 \leq i \leq 4$, plus an additional track label number. The output was written in the format of raw data and served as input to the analysis package. The simulated data were processed as if coming from the stage after clustering the ADC pixels, i.e. the hits level. Using a gaussian smearing with $\sigma = 3.4$ mm, as observed in the experiment, the simulated hits were distorted to take into account the position resolution due to the clustering of pixels.

The positions of the tracks in x and y in the second and third chamber were used as input to the momentum reconstruction routine. This yields the reconstructed set of momentum components per event $(P_x^{'}, P_y^{'}, P_z^{'})$ and the track label. Subsequently for each reconstructed track the difference between the original and the reconstructed momentum was analyzed.

This procedure resulted in a momentum resolution $\frac{\Delta P}{P} = (0.6 + 0.16 \cdot P(GeV/c))\%$ as shown in figure 4.15. The resolution in the momentum differences is presented in figures 4.16-4.20. For small momentum differences we derive a resolution of 10 MeV/c for Q_{inv}, Q_T, Q_{Tout} and Q_{Tside}; see section 2.8.2 for definition, whereas for Q_L the resolution is 20 MeV/c. In the correlation analysis these values are used as the minimum bin size.

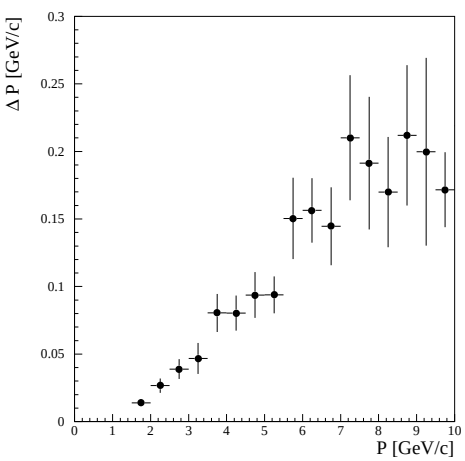

Figure 4.15: *Resolution for momentum P.*

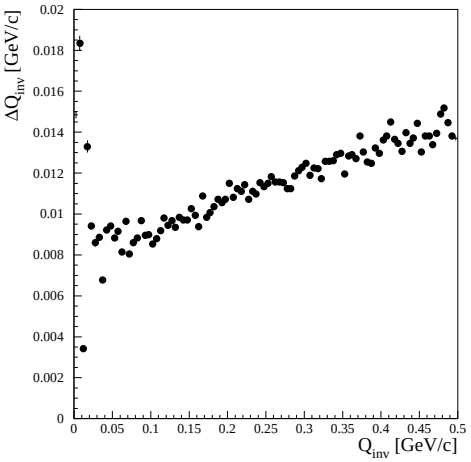

Figure 4.16: *Resolution for momentum difference Q_{inv}.*

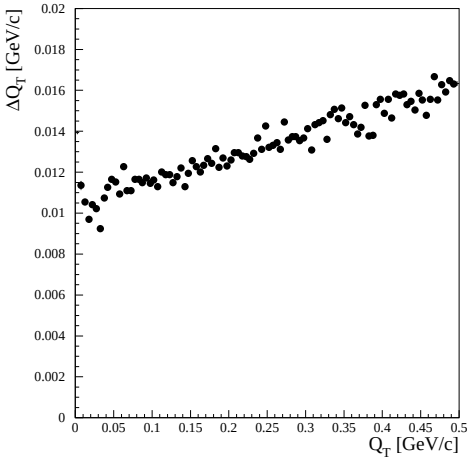

Figure 4.17: *Resolution for momentum difference Q_T.*

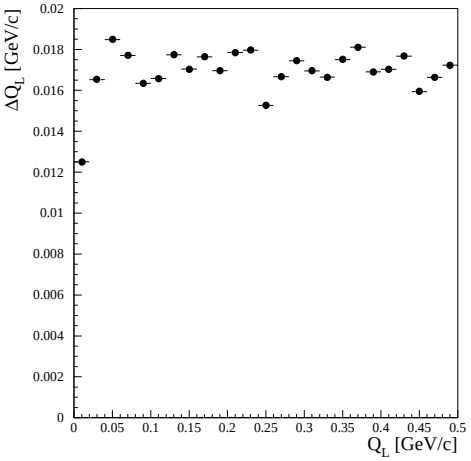

Figure 4.18: *Resolution for momentum difference Q_L.*

4.7 Efficiency Calculations

From efficiency measurements using a ^{90}Sr source the efficiency of the MSAC was estimated to be about 95 %. However, these detectors have not been calibrated in a test beam at the WA93 setup to check this value. Therefore, measured S + Au data were used to determine the efficiency in a high track multiplicity environment. Two methods were applied to derive numbers for

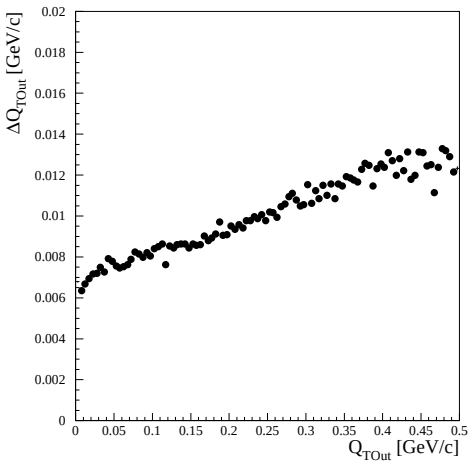

Figure 4.19: *Resolution for momentum difference Q_{Tout}.*

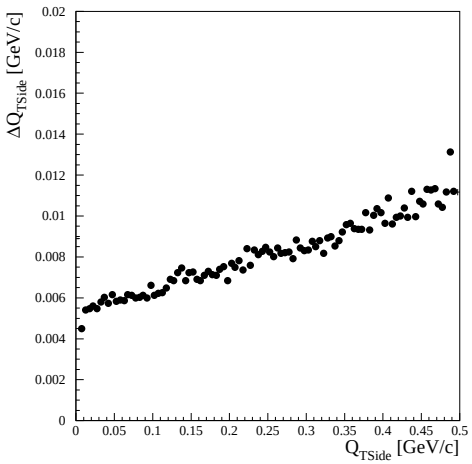

Figure 4.20: *Resolution for momentum difference Q_{Tside}.*

both the global and the local efficiency. The global efficiency stands for the overall efficiency of the chamber. For the local-efficiency calculation the chamber has been subdivided in equal areas. The finally produced local-efficiency map is included in a simulation in order to calculate a correction spectrum for the measured single-particle spectra.

The acceptance region of the charged-particle spectrometer is largely covered by the charged-particle veto consisting of two layers of streamer tube detectors (STD), [56, 60]. The information on the position of fired STD pads and the hits in the MSAC chambers, was used for field-off runs to get a global efficiency estimate. The tracks consisted of STD hits within the STD position resolution. As an efficiency for the STD of 83 % has been reported [60] only $\approx$ 70 % of true tracks are left over. These tracks have to fulfill the criterium of hits within a radius of 2 cm in three MSAC chambers. In the fourth remaining chamber for which the efficiency is calculated a hit has to be found within a variable size window in order to declare this chamber efficient. Mixed events are used to correct for accidental hits in this window. An artificial enhancement of the calculated efficiency due to satellites is prevented by counting in case of several hits within the window only once. The efficiency is calculated according to:

$$\epsilon(ch) = \frac{N_{eff}(ch) - N_{bck}(ch)}{N_{tracks}(ch)} \tag{4.22}$$

where $N_{eff}(ch)$ is the number of hits found for the defined tracks $N_{tracks}(ch)$ and $N_{bck}(ch)$ the number of background hits found by the event-mixing

method. A variation of the window size between 2 and 6 cm yields the values shown in table 4.1. As can be seen the efficiencies have a maximum

Table 4.1: *Calculated global efficiencies.*

ϵ_1 chamber 1	ϵ_2 chamber 2	ϵ_3 chamber 3	ϵ_4 chamber 4	window $[cm]$
0.44 ± 0.02	0.58 ± 0.03	0.53 ± 0.03	0.36 ± 0.02	2.0
0.48 ± 0.02	0.63 ± 0.03	0.58 ± 0.03	0.37 ± 0.02	4.0
0.46 ± 0.02	0.62 ± 0.03	0.57 ± 0.03	0.38 ± 0.02	6.0

for a window of about 4 cm and tend to decrease for both larger and smaller windows. The decrease in efficiency for an increase of the window size can be explained by the fact that finally always a background hit will be found. In the case of decreasing the window size the single-track resolution causes the loss in efficiency. The overall track efficiency can be calculated using the derived global chamber efficiencies. Tracks are made by a combination of hits in either three or four chambers, so called 3-chamber tracks or by the more severe condition of a combination of hits in four chambers, so called 4-chamber tracks. In case of 3-chamber tracks the track efficiency ϵ_{34} is defined by

$$\epsilon_{34} = \epsilon_1 \cdot \epsilon_2 \cdot \epsilon_3 \cdot (1 - \epsilon_4) + \epsilon_1 \cdot \epsilon_2 \cdot (1 - \epsilon_3) \cdot \epsilon_4 + \epsilon_1 \cdot (1 - \epsilon_2) \cdot \epsilon_3 \cdot \epsilon_4 + (1 - \epsilon_1) \cdot \epsilon_2 \cdot \epsilon_3 \cdot \epsilon_4 + \epsilon_1 \cdot \epsilon_2 \cdot \epsilon_3 \cdot \epsilon_4 \qquad (4.23)$$

thus $\epsilon_{34} = 33 \pm 3\%$. In the case of only 4-chamber tracks the track efficiency $\epsilon = \epsilon_1 \cdot \epsilon_2 \cdot \epsilon_3 \cdot \epsilon_4 = 6.5 \pm 0.6\%$.

The local efficiency of each chamber was calculated by using the hit information of the remaining chambers to define tracks. A grid of 5×6 local areas of 24 cm (y) $\times$ $24\frac{2}{3}$ cm (x) were defined for each chamber. Hits were searched in a square of 4×4 cm^2 around the defined tracks and background hits were acquired using a region of equal area outside this square. The global chamber efficiency derived from the average of the found local chamber efficiencies is $\epsilon_1 = 45.0 \pm 0.4\%$, $\epsilon_2 = 64.1 \pm 0.4\%$, $\epsilon_3 = 62.9 \pm 0.4\%$ and $\epsilon_4 = 32.6 \pm 0.4\%$. These values are close to those from table 4.1. The track efficiency for 3-chamber tracks is then $\epsilon_{34} = 32 \pm 1\%$ and the 4-chamber track efficiency $\epsilon = 5.9 \pm 0.1\%$.

4.8 Acceptance Simulations

The charged-particle spectrometer measures momenta for a limited region in phase space of the total amount of emitted negatively charged particles. Furthermore, the MSAC detectors as discussed in the previous section are not 100% efficient.

The acceptance of an arbitrary detector is limited both by a geometry and by efficiency. Only in case a detector has full 4π coverage and infinitely small, fully-efficient detectors, acceptance corrections will not be necessary. In order to get a correction spectrum for acceptance of the charged-particle spectrometer the Lorentz-invariant variable, transverse momentum P_T and the Lorentz-additive variable rapidity Y, are used.

The GEANT package was used for the acceptance simulations. Here the geometry and magnetic field of the spectrometer are defined. Events with a flat input spectrum in P_T versus Y were used as input to the simulation. The particles π^- were given a flat distribution in momentum $1.5 < P < 40$ GeV/c, a flat distribution in the azimuthal angle $-180^\circ < \phi < 180^\circ$. A limited range in θ, the angle with respect to the beam axis, was chosen $0^\circ < \theta < 20^\circ$ with a particle distribution flat in $\cos\theta$. Care was taken to check that the input spectrum covered more than the region of interest for the measured data. The number of particles per event was 300, yielding about 30 tracks in the MSAC's. Switching all interactions and decays off, 100.000 events were simulated using the mapped Goliath magnetic field. The particles are within the geometrical acceptance in case the tracks pass through 3 or 4 chambers and point at the target in $|y| < 2.5$ and $2.5 < x_0 < 80$ cm. The geometrical acceptance for exactly 4 chambers was also calculated. The ratios of the geometrically accepted and the input tracks are shown in figure 4.21 for the 3-chamber tracks. Analogous plots were made for 4-chamber tracks. Division of the measured spectra by these spectra corrects for the limited geometrical acceptance. The efficiency correction was determined using the previously calculated local-efficiency map and the hits from the above simulation. A Monte-Carlo calculation was done for each hit using the current local-efficiency probability in the specific chamber. The tracking and reconstruction routines hereafter try to reconstruct the track. The ratios of these efficiency-distorted reconstructed tracks by the geometrically accepted tracks were calculated for the 3-chamber tracks and the 4-chamber tracks. The result for 3-chamber tracks is shown in figure 4.21.

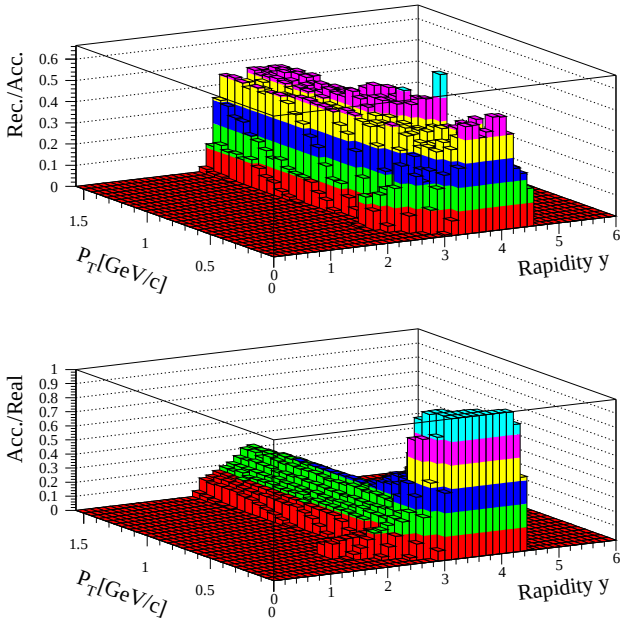

Figure 4.21: *Efficiency (upper) and geometrical (lower) correction spectra for 3-chamber tracks.*

4.9 Background Calculations

The contributions of two background components to the measured negatively charged-particle spectra are discussed in this section. The corrections are essential for a correct interpretation of the measured single-particle distributions and the results from intensity interferometry. Background may influence the multiplicity of tracks, the apparent temperature slopes of P_T spectra and the chaoticity parameter of the two-particle correlation function.

Simulations were done to estimate the possible contribution of various negatively charged-particle species to the measured transverse momentum spectrum. The background dependence on the transverse momentum is studied as no variation in background on the accepted rapidity is observed. This approach is well suited for the study of the P_T spectra and the analysis of correlation functions as a function of P_T.

A second background component arises due to accidentally reconstructed tracks. The contribution to the transverse momentum spectrum as a function of the number of used chambers to build the tracks will be discussed.

4.9.1 Ratios of Negatively Charged Particles

In order to get an estimate of the species of negatively charged particles contributing to the transverse-momentum spectrum simulations were done using central S+Au collisions in the impact parameter range 0. to 1.0 fm produced by the VENUS model [90]. The results calculated in this way are of course model dependent. However, VENUS describes measured spectra well and deep insight is gained into the properties of the charged-particle spectrometer. The GEANT-based simulation package was used including all possible interactions (e.g. δ-rays, conversion, decays, bremsstrahlung, pair production) and the setup consisting of target, Si-Drift detector, Goliath magnet and MSAC chambers. Hits for the different particle species were identified in the MSAC chambers and used as input for the track reconstruction in the analysis program. Although a large fraction $\approx 60\%$ of the negative pions decays before hitting all the chambers more than 97 % of the related negative muon tracks can be reconstructed. The ratios thus calculated are presented in figures 4.22, 4.23, 4.24 and 4.25.

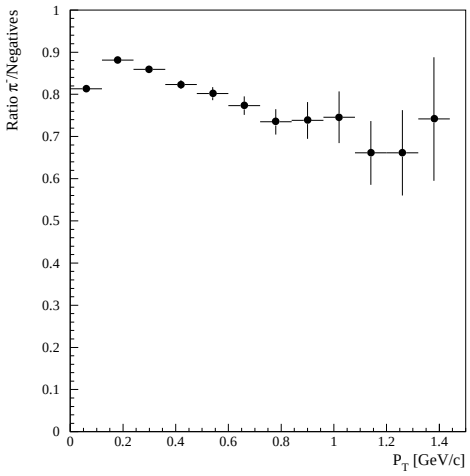

Figure 4.22: *Ratio of reconstructed pions to negatively charged particles as a function of the transverse momentum.*

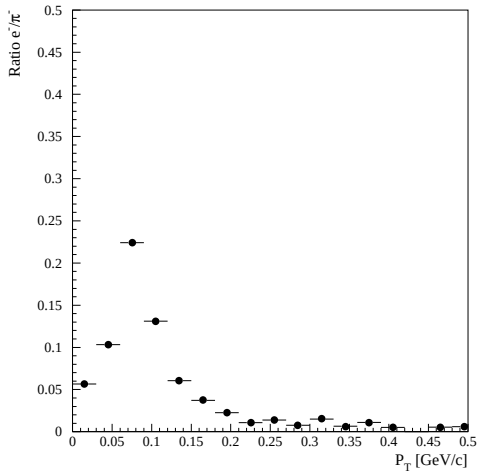

Figure 4.23: *Ratio of reconstructed electrons to pions as a function of the transverse momentum.*

It can be seen that the electrons cause a large background contribution at P_T below 0.2 GeV/c, whereas the kaons and anti-protons rise at high P_T. The pion content is smaller than 90% and has a maximum at $P_T = 0.2$

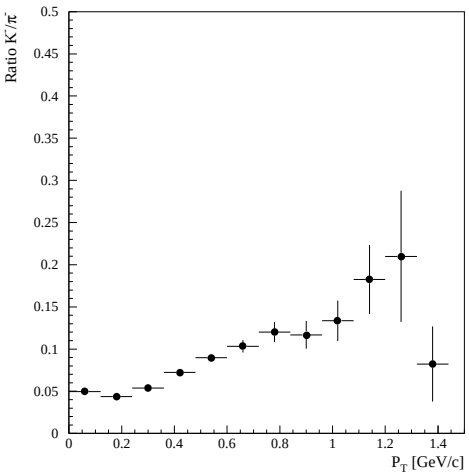

Figure 4.24: *Ratio of reconstructed kaons to pions as a function of the transverse momentum.*

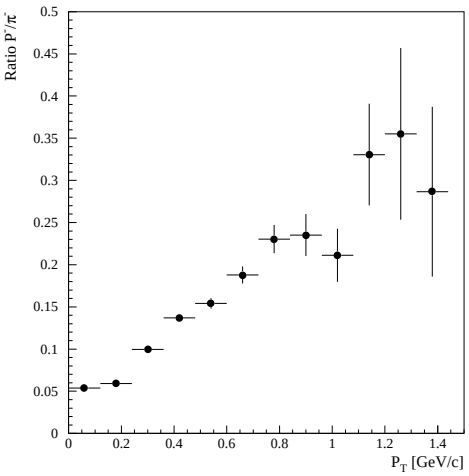

Figure 4.25: *Ratio of reconstructed antiprotons to pions as a function of the transverse momentum.*

GeV/c.

The lack of particle identification by the WA93 charged-particle spectrometer will cause a lowering of the correlation strength for the study of the two-particle correlation function, section 5.2.

4.9.2 Combinatorial Background

The large cluster multiplicities may lead to accidentally reconstructed tracks although sharp selection criteria were applied, as previously described. Calculations estimating the contribution of such random tracks use the mixed-event method. Event-wise each chamber receives clusters from the corresponding chamber, of a different event, but with a hit multiplicity equal to the current event class. Ten event classes were defined which properly describe the hit distribution function for each chamber. The results for 3-chamber tracks and 4-chamber tracks are shown in figure 4.26 and figure 4.27, respectively. The background contribution for 3-chamber tracks is less than 35 % and for 4-chamber tracks less than 8 %.

The components of the random combinatorial background for the 3- and 4-chamber tracks lead to a decrease of the correlation strength in the study of the two-particle correlation function; see section 5.2, in addition to background contributions due to the absence of particle identification; see section 4.9.1, and particles from resonance decays [19, 40]. Furthermore,

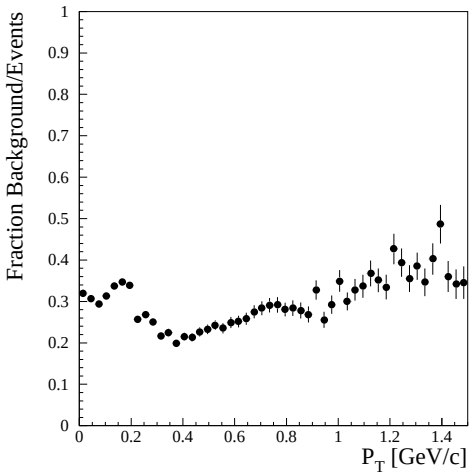

Figure 4.26: *Ratio of background- to event-tracks using 3-chamber tracks.*

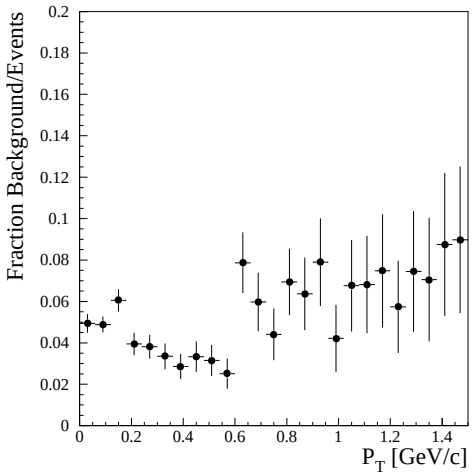

Figure 4.27: *Ratio of background- to event-tracks using 4-chamber tracks.*

the multiplicity distributions; see section 5.1.2, and transverse-momentum spectra; see section 5.1.3, need to be corrected for the random combinatorial background as it influences both the yield and the shape of these spectra.

4.10 Summary

In this chapter the analysis of the charged-particle-spectrometer data was discussed. Knowledge of the detector properties is essential for the corrections and proper understanding of produced final spectra.

The alignment of the detector system appeared to be a time-consuming but necessary procedure. It optimizes the track reconstruction and the momentum resolution. From the study of the width of the track distribution at the target for field-off data, it was decided to use clusters larger than three pixels and an ADC value of at least 19. A more relaxed constraint led to a broader track-position distribution at the target position. The increase was caused by a larger random-combinatorial-background contribution. However, for each event still a large number of clusters, not all related to tracks, remained for the respective detectors. A selection on the number of chambers to build a track was shown to decrease the random-combinatorial-background contribution from less than 35 % for 3-chamber tracks to less than 8 % for 4-chamber tracks. Furthermore, it was shown using central VENUS events and GEANT simulations that several particle

species contribute to the P_T spectrum in different regions. The electrons contribute on average less than 10 % to the P_T spectrum below P_T = 0.2 GeV/c, whereas the kaon and anti-proton content rises above P_T = 0.2 GeV/c. Knowledge of these two background contributions enables a better understanding of both the single-particle spectra, that is the multiplicity and transverse-momentum spectra, and the two-particle correlations.

A realistic GEANT simulation with central VENUS events and the full WA93 setup incorporating the relevant particle interactions and the position resolution of the MSAC's was used to obtain the momentum resolution of the charged-particle spectrometer. The relative momentum resolution, which determines the resolving power of the intensity-interferometry analysis, was about 10 MeV/c for the respective relative momentum components except for the longitudinal component which was shown to be about 20 MeV/c. These values were used as minimum binning size in the interferometry analysis. Compared to a typical half width of 50 MeV/c for the correlation function the momentum resolution was determined to be sufficient.

The local efficiency of the detectors was determined. These measured values were used as input to GEANT simulations to calculate a correction spectrum for the single-particle spectra. Furthermore, a correction spectrum was calculated for the limited geometrical acceptance.

In the next chapter 5 the above-obtained correction spectra have been used to obtain the final spectra. Furthermore, these spectra are used to explain certain observed phenomena in the interferometry analysis.

Chapter 5

Results from the Charged-Particle-Spectrometer Data

The final results from the data-analysis of the Charged-Particle Spectrometer will be presented below. In the first part single-particle spectra, like the negatively-charged-particle multiplicity and the P_T spectra, will be presented. In the second part the results from the intensity interferometry are discussed.

Both sets of results are presented for a selection of three impact parameter classes: central, semi-central and peripheral reactions. Differences in the results for these classes may then indicate interesting changes in the behaviour of hadronic matter produced in central reactions. Furthermore, in order to study the dynamic evolution of the hot reaction zone a selection on the transverse momenta of the correlated pion pairs has been made. This selection is only done for the central collisions as the limited statistics prevent from doing such an analysis for the peripheral and semi-central trigger.

The combination of single-particle and correlation spectra provides information on the freeze-out density, the freeze-out time, the temperature and flow of the hot reaction zone. The freeze-out density can be determined from a combination of both the measured transverse-energy and volume. The freeze-out time can be deduced as we will see in chapter 6 from the systematic study of the measured longitudinal radius as a function of the transverse momentum of the correlated pion-pairs. A large difference in the two transverse directions R_{Tout} and R_{Tside} related to the time-duration of emission of the pions; see section 2.8, was suggested by Pratt [91] and

Bertsch [92] as a possible signal of a quark-gluon phase transition.

A comparison of the WA93 results on single-particle spectra and intensity interferometry with the results from other experimental groups and proposed theoretical models will be made in chapter 6.

5.1 Single-Particle Spectra

Before presenting results on the single-particle spectra the phase-space coverage of the charged-particle spectrometer needs to be discussed. Reconstructed tracks are analysed up to a transverse momentum $P_T = 3.0$ GeV/c and for a rapidity range $2.2 < Y < 4.4$, see figure 5.1. Full coverage in rapidity, that is the range in rapidity for which the measured transverse momenta are not restricted by the geometrical acceptance, exists for $3.0 < Y < 3.6$. Such a region is of interest as here one will not artificially bias the measured spectra by a lack of sensitivity. The results on the single-particle spectra will be presented for this specific region.

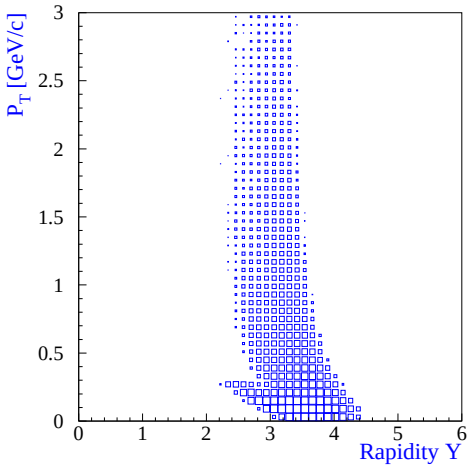

Figure 5.1: *Acceptance of the charged-particle spectrometer, expressed in the plane of transverse momentum P_T versus the rapidity Y. Tracks were constructed using 3-chamber tracks.*

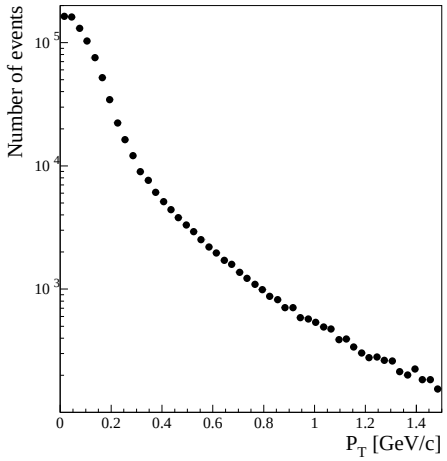

Figure 5.2: *Raw distribution of the transverse momentum of negatively-charged particles. Only the statistical error has been implemented.*

The raw distributions of the momentum components P_T, P_x, P_y, P_z and P are shown in figures 5.2-5.6, respectively. These spectra have not been

corrected for acceptance and efficiency, but show the region of sensitivity for the charged-particle spectrometer. It can be seen in figure 5.3 that also momenta in the positive x direction are measured. This effect causes the side wing at low transverse momenta in the acceptance plot, P_T versus rapidity, see figure 5.1. These are tracks which have a low enough momentum in the positive x direction to be bent by the dipole magnet, with a momentum kick of roughly 0.6 GeV/c, into the geometrical acceptance of the spectrometer. The momentum distribution in the y direction, figure 5.4, is symmetric due to the mirror symmetry in the xz-plane of the tracking system. The

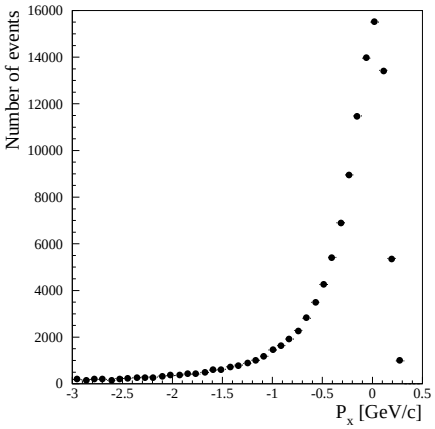

Figure 5.3: *Raw momentum distribution in the x direction. Positive values of P_x lie within the acceptance as these tracks are bent across the beam-line.*

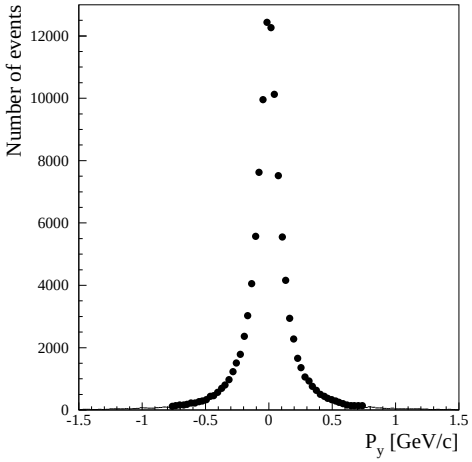

Figure 5.4: *Raw momentum distribution in the y direction. The symmetry in the distribution is related to the up-down symmetry of the acceptance in the y direction of the tracking system.*

reconstruction of the size of the momenta is limited by the geometrical acceptance and thus was restricted to the range $1.5 < P < 40$ GeV/c. In figure 5.5 and 5.6 the lower cut on $P = 1.5$ GeV/c is observed, and up to $P = 25$ GeV/c reconstructed tracks are shown. The raw distributions for the angular acceptance are presented in figures 5.7-5.10, for the dip, horizontal, ϕ, and θ angles, respectively. Again the symmetry observed in the dip angle, $-0.08 <$ dip < 0.08 rad, and the ϕ angle, $-180° < \phi < 180°$, is related to the mirror symmetry in the y direction of the chambers. The small systematic decrease for the dip angle around dip ≈ 0 rad is related to

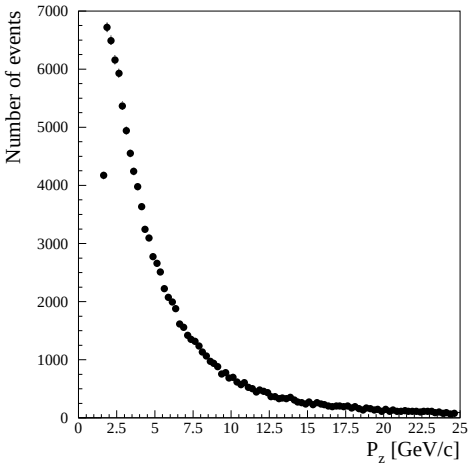

Figure 5.5: *Raw momentum distribution in the z direction. Tracks are reconstructed starting from P = 1.5 GeV/c up to 40 GeV/c.*

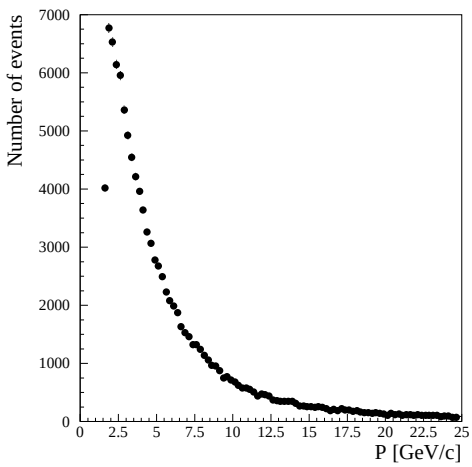

Figure 5.6: *Raw momentum distribution for the size P of the momentum. Tracks are reconstructed starting from P = 1.5 GeV/c up to 40 GeV/c.*

the Tchebysheff parameterization for this region. Also the alignment of the spacers at $y = 0$ may add to this. Note the acceptance in the θ angle up to $\theta \approx 12$ degrees. The GEANT simulations were done up to $\theta = 15$ degrees, thus fully covering the geometrical acceptance of the spectrometer in the θ angle.

5.1.1 Impact-Parameter Determination

Three centrality triggers were derived from the measured transverse energy, see figure 5.11, and are examined in detail: central (ETH), semi-central (SC) and peripheral (ETP). For these respective triggers the impact-parameter range can be calculated [93]. From the luminosity and target thickness the number of events above E_T = 35 GeV equals 67 ± 4 % of the total S+Au nuclear interaction cross-section σ_{SAu}. The total cross-section for S+Au is $\sigma_{SAu} = \pi \cdot (R_S + R_{Au})^2$ with the radius $R = A^{1/3} \cdot r_0$ fm, where $r_0 = (1.15 \pm 0.05)$ fm, so that $\sigma_{SAu} = 3359 \pm 215$ mbarn. The cross-sections and impact-parameters for the respective triggers, presented in table 5.1, are calculated by integrating the number of measured events for each trigger selection, see figure 5.11 and 5.12, and by normalizing to the cross-section for the 35 GeV threshold on transverse energy. The percentages indicated from

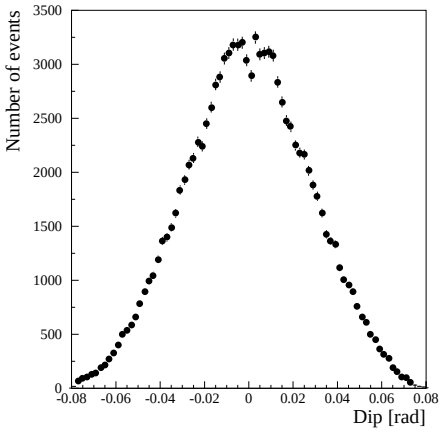

Figure 5.7: *Dip angle distribution. The symmetry is due to the acceptance in the y direction of the tracking system. Particles in the range* -0.08 *rad to* 0.08 *rad are accepted.*

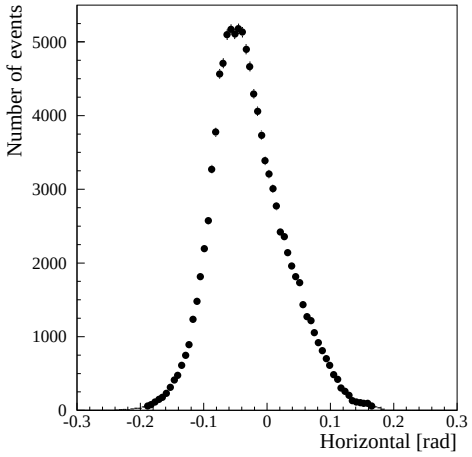

Figure 5.8: *Horizontal-angle distribution. Particles in the range* -0.2 *rad to* 0.2 *rad are accepted.*

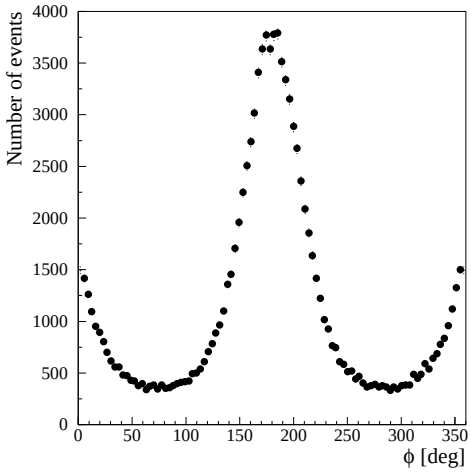

Figure 5.9: ϕ *angle distribution. The symmetry is due to the acceptance in the y direction of the tracking system. Particles in the range* $0 < \phi < 360°$ *are accepted.*

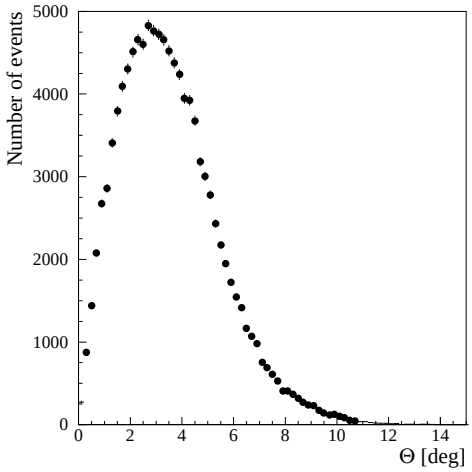

Figure 5.10: θ *angular distribution. Particles in the range* $0 < \theta < 12°$ *are accepted.*

now on in the figures refer to the fraction of the total S+Au nuclear reaction cross-section. The summed cross-section of the three respective trigger

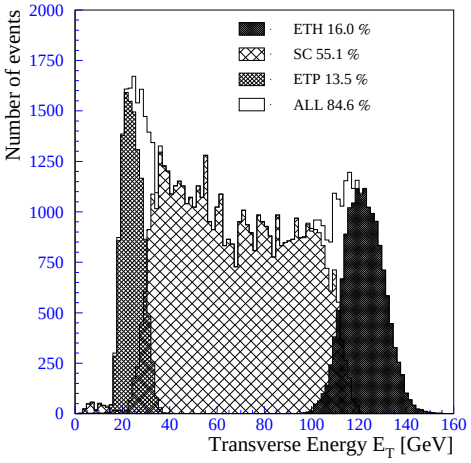

Figure 5.11: *Number of events versus transverse energy measured by the MIRAC for the Central (ETH), Semi Central (SC) and Peripheral (ETP) triggers. The cross-section is expressed in percentages of the total S+Au cross-section for each trigger selection.*

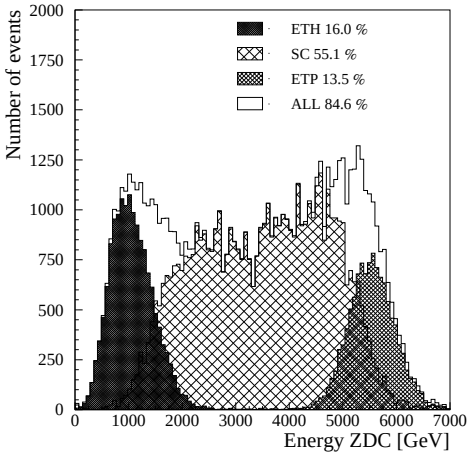

Figure 5.12: *Number of events versus the energy measured by the ZDC for the Central (ETH), Semi Central (SC) and Peripheral (ETP) triggers. The cross-section is expressed in percentages of the total S+Au cross-section for each trigger selection.*

Table 5.1: *Impact-parameters and cross-sections for the respective trigger selections.*

	b [fm]	σ [mbarn]
Central	0.-4.1 $\pm$ 0.3	537 $\pm$ 39
Semi-Central	4.1 $\pm$ 0.3 - 8.7 $\pm$ 0.5	1852 $\pm$ 133
Peripheral	8.7 $\pm$ 0.5 - 9.5 $\pm$ 0.6	455 $\pm$ 33
total	0. – 9.5 $\pm$ 0.6	2844 $\pm$ 142

selections equals 84.6 $\pm$ 6.4% of the total σ_{SAu}. The calculated impact-parameters are used as input to simulations with event generators such as

the VENUS- and FRITIOF-models.

5.1.2 Negatively-Charged-Particle Multiplicity

The negatively-charged-particle multiplicity has been investigated in the rapidity range $3.0 \leq Y \leq 3.6$ where the spectrometer covers the full P_T range. Restrictive cuts, see section 4.3, most importantly on the relative spatial distance were used to prevent distortions due to detector limitations. For the three trigger selections spectra were made both for events and random background combinatorics, figures 4.26, 4.27, 5.13, and 5.14. The spectra

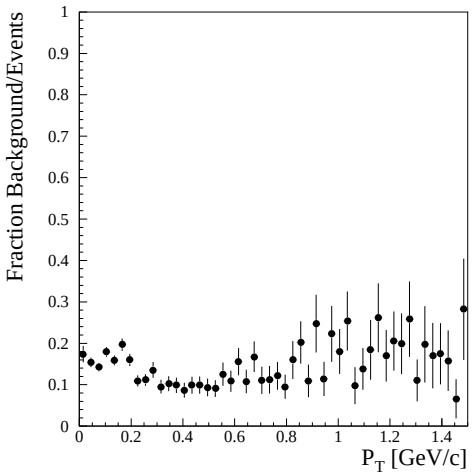

Figure 5.13: *Ratio of the number of background-to-event tracks using 3-chamber tracks for semi central events.*

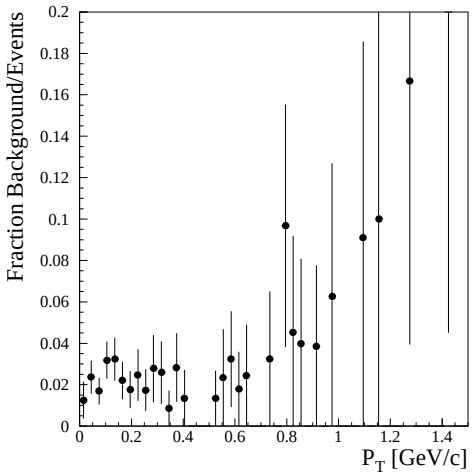

Figure 5.14: *Ratio of the number of background-to-event tracks using 3-chamber tracks for peripheral events.*

for random background combinatorics were made defining for each trigger selection 10 cluster-multiplicity classes which were used in the event-mixing as input to the tracking; see table 5.2. The high random combinatorial background for the central events; see figure 4.26, is directly related to the cluster multiplicities in the chambers for such events. The 3-chamber tracks were used for the peripheral and the semi-central triggers. For the central trigger both the case of 3-chamber tracks and the more restrictive case of 4-chamber tracks were studied. The results for these two cases are identical within the error bars, after correction for acceptance, efficiency and background, for $3.1 < Y < 3.5$. However, the 4-chamber tracks have a depleted

Table 5.2: *Average cluster multiplicities per chamber (Ch.) and track multiplicities $< N_{track} >$ per event for the respective trigger selections.*

	Ch. 1	Ch. 2	Ch. 3	Ch. 4	$< N_{track} >$
Central	45	175	120	60	9.4
Semi-Central	25	110	65	40	4.6
Peripheral	5	40	10	6	1.9

intensity of tracks at $3.0 < Y < 3.1$ and $3.5 < Y < 3.6$ related to the limited acceptance for 4-chamber tracks with respect to 3-chamber tracks. This decrease has been observed in the ratio of the rapidity spectra for these two cases. Therefore 3-chamber tracks were used to achieve the widest possible coverage $3.0 < Y < 3.6$.

In order to exclude distortions from reactions in the beam-line upstream of the target, a check was made for measured events when there was no target in the beam-line. The following upper limits for the event fraction not related to target events were calculated: peripheral ≤ 0.3 %, semi-central ≤ 0.02 % and central ≤ 0.006 %. Target-out events with tracks were only found for the peripheral trigger, the calculated values for the semi-central and central events are upper limits.

Strong restrictive cuts on the relative spatial distance of nearby tracks are made to prevent distortions of the correlation function due to the previously described satellite behaviour; see section 4.3. In case of two tracks, which are parallel within an average proximity ≤ 3 cm, only one of them is used for the single-particle spectra, yielding an average number of tracks $< N_{track} >$ per event, see table 5.2. This cut was used as it removes most of the satellite tracks; see figure 4.9 and 5.15, yielding a single-track distribution with less than 2 % satellite tracks for the central trigger. The effect of an even larger distance cut on the single-particle multiplicity spectra was investigated. A larger distance cut will remove also non-satellite tracks. The hard satellite cut for parallel tracks with an average distance smaller than 8 cm, is used for the correlation analysis. The track multiplicity for the 8 cm distance cut has been compared to the 3 cm distance cut. A reduction of the track multiplicity by ≈ 30 % for the central trigger, ≈ 18 % for the semi-central and ≈ 5% for the peripheral trigger can be concluded from figure 5.15. The reduction is largest for the central trigger due to a higher track density and thus increased probability for track removal by the average two-track distance cut. A correction for the loss of tracks due to the two-track distance

cut and a limited two-track separation is used. Therefore the measured track multiplicity values for the 3 cm cut have been extrapolated to the value at 0 cm according to a linear fit made for values above the 4 cm cut.

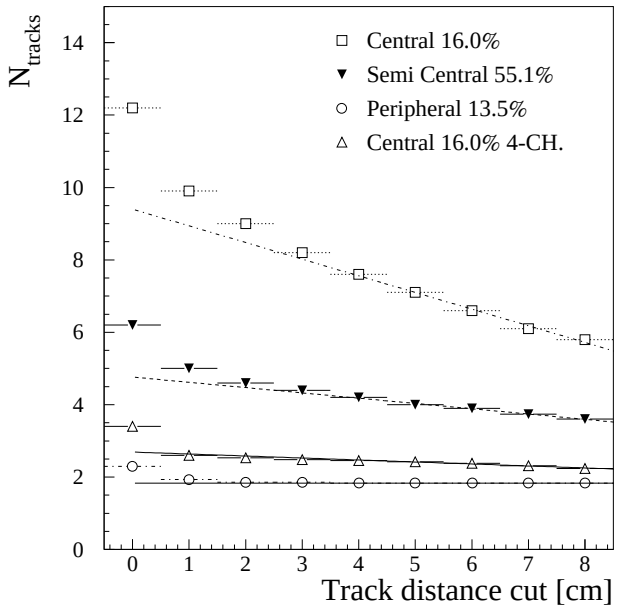

Figure 5.15: *Average number of reconstructed tracks per event versus the applied distance cut for 1000 trigger selected events. The number of 3-chamber tracks are shown for all triggers and the number of 4-chamber tracks (4-CH) for the central trigger.*

Two-dimensional spectra have been accumulated in P_T versus rapidity. From these spectra the calculated mixed-event background is subtracted. Thereafter, corrections for efficiency, using a local-efficiency table from section 4.7, and the acceptance, using GEANT calculations, are made. The GEANT-generated events had a homogeneous distribution in rapidity and transverse momentum. In addition a check was made on the acceptance and efficiency corrections using VENUS-generated events as input to the GEANT calculations; this yielded identical results within ± 1 %. The respective maximum multiplicities in the rapidity range $3.0 \leq Y \leq 3.6$ are presented in figure 5.16 and table 5.3.

An increase of the negatively-charged-particle multiplicity is observed to-

Table 5.3: *Maximum negatively-charged-particle multiplicities in the rapidity region* $3.0 \leq Y \leq 3.6$ *for the three centrality classes.*

	$\frac{dN^-}{dY}_{max}$
central	57 ± 3
semi-central	20 ± 1
peripheral	8 ± 0.5

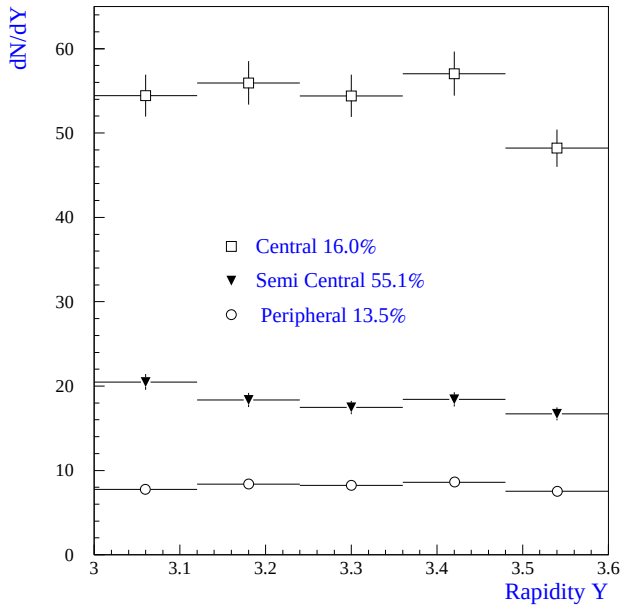

Figure 5.16: *Negatively-charged-particle multiplicity per unit of rapidity in the rapidity range* $3.0 \leq Y \leq 3.6$ *with full coverage in* P_T *for the three trigger selections: peripheral, semi-central and central.*

wards more central collisions. The predicted negative-hadron multiplicities from the event generators VENUS and FRITIOF for the respective triggers; see table 5.4, are in good agreement for the central and peripheral data and reveal a slight overestimation of the semi-central data. A comparison to other experimental data is made in section 6.1

Table 5.4: *Maximum negative-hadron multiplicities in the rapidity region* $3.0 \leq Y \leq 3.6$ *from simulations for the three centrality classes using the VENUS and FRITIOF event generators.*

	VENUS $\frac{dN^-}{dY}_{max}$	FRITIOF $\frac{dN^-}{dY}_{max}$
central	55.3 ± 0.3	57.8 ± 0.1
semi-central	25.5 ± 0.1	25.0 ± 0.04
peripheral	6.9 ± 0.1	5.3 ± 0.04

5.1.3 Transverse-Momentum Spectra

The transverse-momentum spectrum was investigated for the respective triggers, taking into account the background, efficiency ϵ_{eff} and acceptance ϵ_{acc} corrections. These spectra are calculated up to 1.5 GeV/c as above this range the contamination by spurious tracks is too large to apply the corrections. For all triggers a rather similar behaviour is observed for the transverse-momentum spectra, see figure 5.17.

The cross-section for the respective triggers was calculated according to

$$\frac{1}{P_T}\frac{d\sigma}{dP_T} = \frac{1}{P_T}\frac{\Delta N \cdot \sigma \cdot \epsilon_{eff} \cdot \epsilon_{acc}}{2 \cdot \pi \cdot M \cdot \Delta P_T \cdot \Delta Y} \tag{5.1}$$

where M is the studied number of events, ΔN is the number of entries, σ the reaction cross-section, ΔP_T the width of the bin at P_T and ΔY the rapidity width.

Since these spectra exhibit an exponential behaviour with two different slopes, a thermal distribution with two temperatures T_1 and T_2 has been compared to the data. It should be noted that the slopes might be influenced by e.g. expansion and thus will be referred to as apparent temperatures. A thermal distribution for two sources

$$\frac{1}{P_T}\frac{dN}{dP_T} = C_1 \cdot \sqrt{m_T \cdot T_1} \cdot e^{-m_T/T_1} + C_2 \cdot \sqrt{m_T \cdot T_2} \cdot e^{-m_T/T_2} \tag{5.2}$$

follows from a Boltzmann ansatz for full coverage in rapidity. Similar apparent temperatures T_2 for the respective trigger selections and only a slight increase towards central reactions is observed for the high momentum range from 0.2-1.0 GeV/c, as shown in table 5.5. A steep rise at low P_T for values smaller than 200 MeV/c, with slope fits of $T_1 \approx 23$ MeV in the range 0.-0.2 GeV/c, is observed, see table 5.5.

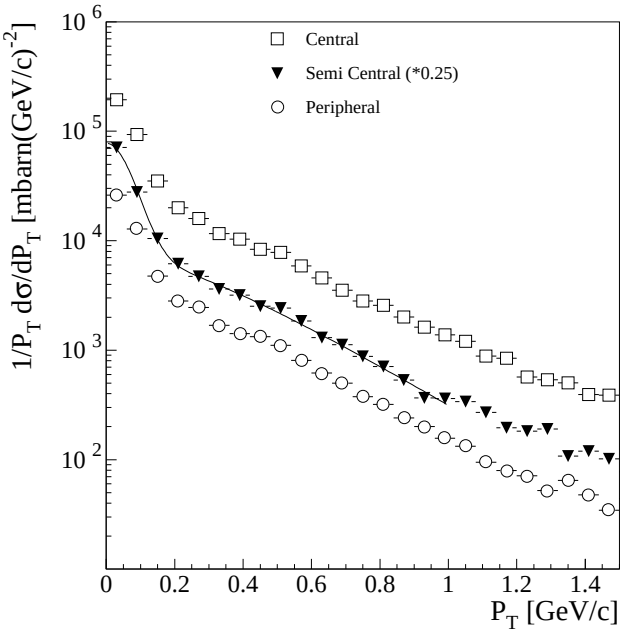

Figure 5.17: *Transverse-momentum spectra for the respective trigger selections.*

Table 5.5: *Apparent temperature values T_1 and T_2 for the respective triggers in the low, $0 \leq P_T \leq 0.2$ GeV/c, and high, $0.2 \leq P_T \leq 1.0$ GeV/c, regions.*

Trigger	P_T [GeV/c]	T_1 [MeV]	P_T [GeV/c]	T_2 [MeV]
Central	0.-0.2	22.8 ± 0.8	0.2-1.0	220.1 ± 2.8
Semi-Central	0.-0.2	23.1 ± 1.7	0.2-1.0	213.1 ± 2.8
Peripheral	0.-0.2	21.2 ± 1.4	0.2-1.0	211.8 ± 3.0

The rapidity dependence of the low P_T enhancement has been studied in figure 5.18. The enhancement is largest at mid-rapidity and decreases towards projectile rapidity. This behaviour is observed for the three trigger selections. Large stopping may cause considerable resonance production at mid-rapidity [19]. Other mechanisms have also been put forward to explain the low P_T enhancement observed by several other experimental groups. A

more extensive discussion of the low P_T enhancement is given in section 6.2.

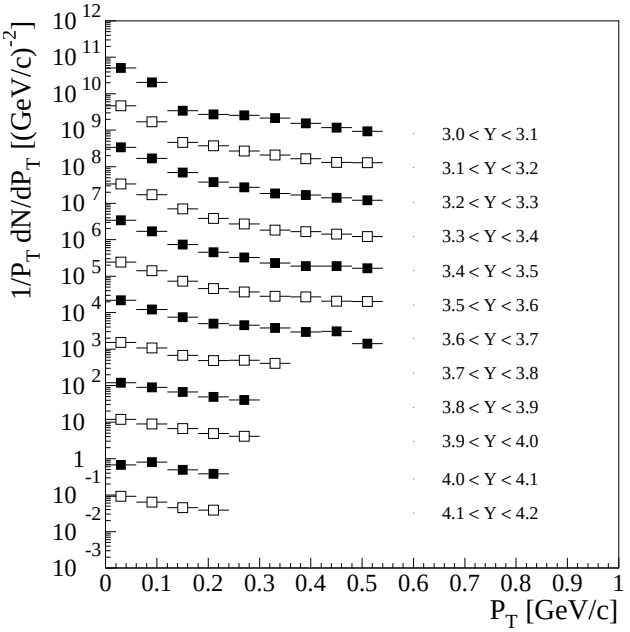

Figure 5.18: *Rapidity dependence of the low P_T enhancement for the central trigger selection. The respective yields have been scaled by factors of 10 in this presentation.*

Possible detector effects have been investigated in detail in order to ensure the low P_T rise. The stability of the local efficiency was checked by inspecting the ratios of P_T spectra for runs with different gain settings normalized to the respective number of events. This yielded a constant value of 1 as a function of P_T so that the statistics for these runs could be added. In a similar way the track multiplicity was shown to be nearly constant. In addition to the random combinatorial background calculations a check was made to verify that the low P_T tracks do not originate from a specific detector part. The transverse momenta appeared not to be related to a certain detector part. The yield of the various particle species at low P_T was investigated with central VENUS events. Ratios of accepted and reconstructed negative particles like electrons, kaons, antiprotons and pions

to the total number of accepted and reconstructed negative particles have been calculated. These are presented in figures 4.22, 4.23, 4.24 and 4.25.

The electrons could cause a background contribution at $P_T \leq 0.2$ GeV/c, whereas the kaon to pion ratio and the anti-proton to pion ratio rise at high P_T. The pion content is never larger than 90% of the total number of negative particles and has a maximum at $P_T = 0.2$ GeV/c. However, regarding the strength of the observed low P_T enhancement electron contamination can not account for this effect.

A comparison to the S+S slopes measured by the NA35 group [51] yields good agreement as slopes are quoted in the range $3.2 < Y < 4.4$ of $T \approx 210$ MeV.

5.2 Correlation Analysis

The correlation function for intensity interferometry has been derived in section 2.8.1. This function is experimentally defined as the ratio of the two-particle probability to the single-particle probabilities

$$C(p_1, p_2) = \frac{2 \cdot < N^2 >}{< N > \cdot (< N > -1)} \frac{\frac{d^2N(p_1,p_2)}{dp_1 \cdot dp_2}}{\frac{dN(p_1)}{dp_1} \cdot \frac{dN(p_2)}{dp_2}} \tag{5.3}$$

normalized to one by $2 \cdot < N^2 > /(< N > \cdot (< N > -1))$ at large relative momentum where N is the number of particle tracks in an event.

The two-particle probability in the numerator was calculated for event samples of tracks selected on an average two-track distance cut of 3 cm. Thus such event samples do not contain tracks within an average distance of 3 cm in order to exclude distortions of the single-particle and correlation spectra due to detector limitations. These event samples were used for the event correlation. All pair combinations within an event are formed, allowing on average $< N > \cdot (< N > -1)/2$ combinations per event. The relative momentum of the pairs is calculated only in case these pairs have an average distance larger than 8 cm. This 8 cm cut in the correlation analysis prevents an enhancement at small relative momenta due to the remnant satellite fraction. This fraction is estimated to be at most 2 % in the event sample for the central trigger, after the 3 cm distance cut.

The contribution of the single-particle probabilities in the denominator is accounted for by using the mixed-event technique. The tracks of the current event are correlated with tracks from a previous event with an equal track multiplicity, allowing on average $< N^2 >$ combinations per event. Again the

relative momenta are only calculated in case the average distance is larger than 8 cm.

The correlation function is calculated by averaging over many events. This was done as the track multiplicity per event, see table 5.2 and table 5.6, is too low to allow for an analysis on an event by event basis.

Table 5.6: *Number of events, event pairs and background pairs for the respective trigger conditions. Central data have been studied both for 3-chamber and 4-chamber tracks.*

	events	event pairs	background pairs
central-3ch	89.452	2026298	4591696
central-4ch	33.925	47427	135733
semi-central	32.276	197045	481775
peripheral	33.925	23112	72734

The relative momenta for the event pairs are weighted by the Gamov factor, see section 2.8.3, thus correcting for the Coulomb repulsion between the similarly charged particles.

For large relative momentum values no correlation should be present and the value of the correlation function should approach unity. In the calculation of the ratio of the Gamov-weighted event pairs to the mixed-event pairs the correlation function is normalized to unity for all analysed events. This is done by a multiplication of this ratio with the total number of mixed-event pairs divided by the total number of event pairs.

The source radii R and correlation strength λ for the respective trigger selections have been studied in one (R_{inv}), two (R_T, R_L) and three dimensions (R_{Tout},R_{Tside},R_L), see section 2.8.2. Since the statistics for the peripheral ($23 \cdot 10^3$ event pairs) and semi-central ($197 \cdot 10^3$ event pairs) data are insufficient to perform a thorough multi-dimensional analysis as a function of the transverse momentum of the pion pair, a comparison between the invariant radii for 3-chamber tracks is presented for these data. The statistics for the central trigger amount to $2000 \cdot 10^3$ event pairs. The fits are made with a 10 MeV/c binning in the ranges $0 < Q_{inv} < 500$ MeV/c, $0 < Q_T < 150$ MeV/c, $0 < Q_L < 150$ MeV/c, $0 < Q_{Tout} < 150$MeV/c and $0 < Q_{Tside} < 150$ MeV/c. These ranges were chosen according to the phase-space coverage. A gaussian source parameterization; see section 2.8, describes the data well and is used to extract the respective source radii.

The errors are calculated according to the statistics in each bin of either the one or multi-dimensional spectra. Systematical errors due to background processes, e.g. random combinatorial background and lack of particle identification, have been estimated from a comparison of results for two halves of the event sample. Such a comparison enables insight in the stability of the calculated results, but does not provide complete knowledge on the systematical error. Model dependent simulations incorporating background and acceptance contributions may provide further knowledge, but are biased due to the initial model assumptions [94].

5.2.1 One-Dimensional Interferometry

The results for the different trigger selections show an increase of the invariant radius going from peripheral to central collisions; see table 5.7. Such a behaviour is expected as the overlap of the projectile nucleus with the target nucleus increases for more central collisions as is already indicated by the increasing multiplicity; see figure 5.16. An explanation for the discrepancy between the correlation strengths for 3-chamber tracks and 4-chamber tracks may be the different random combinatorial background content for these two cases, see figure 4.26 and 4.27.

Table 5.7: *Invariant source radii and correlation strengths for the respective triggers using 3-chamber tracks and using 4-chamber tracks for the central trigger.*

	R_{inv} [fm]	λ
central 3-ch	4.54 ± 0.27	0.28 ± 0.03
central 4-ch	4.57 ± 0.81	0.45 ± 0.08
semi-central	4.21 ± 0.51	0.35 ± 0.02
peripheral	2.94 ± 0.69	0.32 ± 0.07

A typical example of the measured correlation function for a selection on the P_T of the pairs is shown in figure 5.21. The observed behaviour of the correlation function is well described by a gaussian fit. The point at the lowest Q_{inv} deviates from the gaussian parameterization. As this concerns a region of low statistics the point does not influence the outcome of the fit. However, this behaviour may be due to long-lived resonances and has been observed by other experiments [94]. All studied correlation functions

have been checked for the fit quality in order to ensure the significance of the quoted parameters. The errors indicate the statistical error and the systematic error as derived from a comparison of results for two halves of the event sample.

The central-trigger selection has been studied for both 3-chamber tracks and 4-chamber tracks as a function of P_T. This yields results with different correlation strengths. Note that the measured invariant radii without a selection in P_T are similar.

The correlation strength may directly influence the derived radii [53, 54]. Both parameters are not independent which is obvious from a Taylor expansion of the parameterization function. A correlation measurement with a lower correlation strength generally leads to a derivation of a smaller radius.

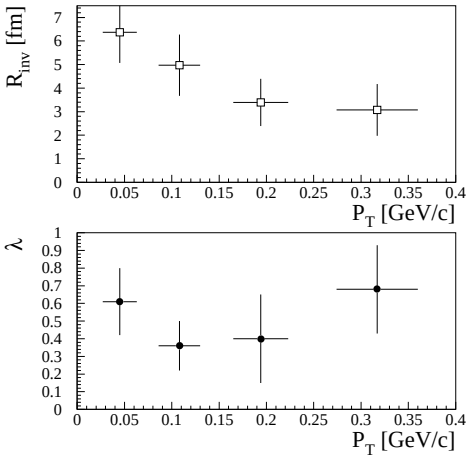

Figure 5.19: *Measured invariant source radii and correlation strengths as a function of the transverse momentum of the pion pair for the central-event trigger using 4-chamber tracks.*

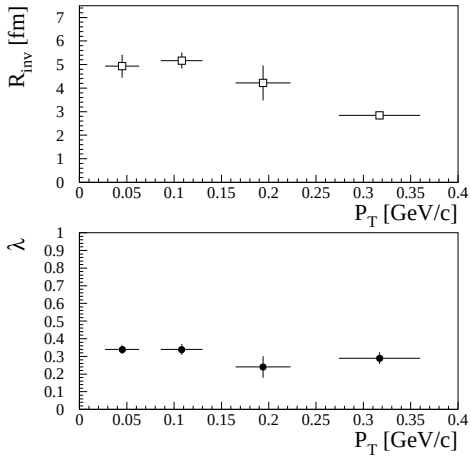

Figure 5.20: *Measured invariant source radii and correlation strengths as a function of the transverse momentum of the pion pair for the central-event trigger using 3-chamber tracks.*

A discrepancy between the invariant radii for 3-chamber tracks and 4-chamber tracks is noticed especially at low P_T; see figures 5.19 and 5.20. Note however that this effect is within the calculated errors. Thus we conclude that the 3-chamber analysis has the advantage of a finer bin-size in the P_T of the pair, due to the large amount of correlated tracks, but results

in a lower λ.

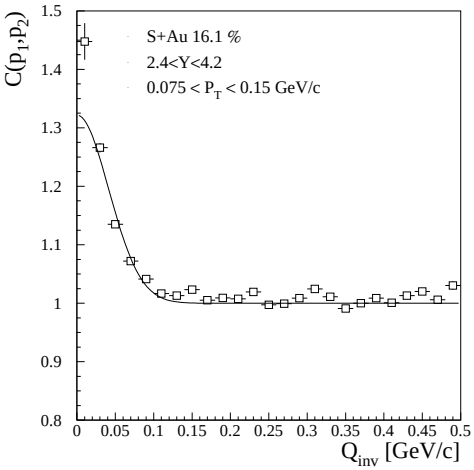

Figure 5.21: *Measured one-dimensional correlation function for a selection on the transverse momentum* $0.075 < P_T < 0.15$ *GeV/c of 3-chamber tracks from central data.*

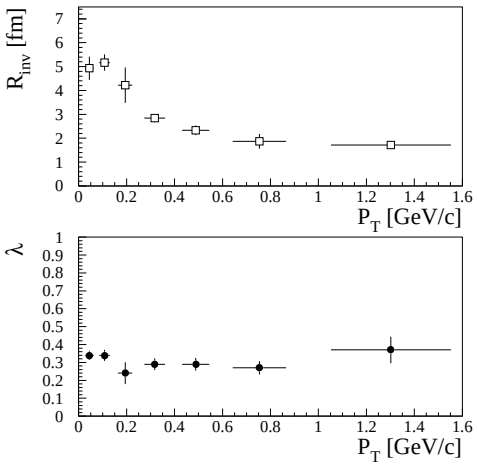

Figure 5.22: *Invariant source radii and correlation strengths as a function of the transverse momentum of the pion pair derived for the central-event trigger using 3-chamber tracks.*

A detailed analysis of the invariant radius as a function of the transverse momentum of the pion pair is presented in figure 5.22 for a more extended region in P_T than in figure 5.20. The correlation strength is nearly constant over the complete range in transverse momentum and a decrease of the invariant radius is observed for an increase in the transverse momentum of the pion pair.

5.2.2 Two- and Three-Dimensional Interferometry

To investigate the longitudinal and transverse flow of the hot collision zone the correlation function has been analysed in two and three dimensions as a function of the transverse momenta of the correlated pairs. Furthermore, a large difference in the two transverse directions, R_{Tout} and R_{Tside} related to the time-duration of emission of the pions; see section 2.8, has been suggested by Pratt [91] and Bertsch [92] as a possible signal of the quark-gluon phase transition. The transverse momentum dependence of the multi-dimensional radii has been investigated in the nucleon-nucleon center-of-mass frame with a rapidity $Y = 3.02$. This analysis has been done only for the central

collisions as peripheral and semi-central data lack statistics, see table 5.8 and 5.9.

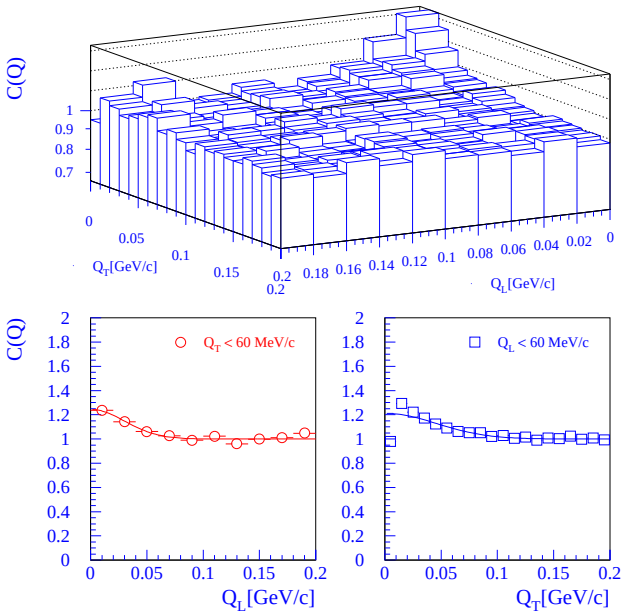

Figure 5.23: *Two-dimensional correlation study as a function of the transverse (Q_T) and the longitudinal (Q_L) relative momentum. A projection for a limited range of 60 MeV/c in either Q_L or Q_T is chosen to show the correlation effect.*

The results presented for the multi-dimensional analysis have been achieved using multi-dimensional fitting procedures. However, to show the correlation effect at small Q-values, the relative momentum of a certain component is projected for a selection on small relative momenta in the remaining components; see figures 5.23 and 5.24.

Two- and three-dimensional fits were applied for the respective trigger conditions. Limited statistics for the semi-central and peripheral trigger only allowed to achieve results for the two-dimensional fit. Again, we observe an increase of both the transverse and longitudinal radii as the centrality of the collisions increases; see tables 5.8 and 5.9.

In all cases of the multi-dimensional correlation analysis; see figure 5.25 and 5.26, a decrease of the longitudinal radii is observed as a function of the

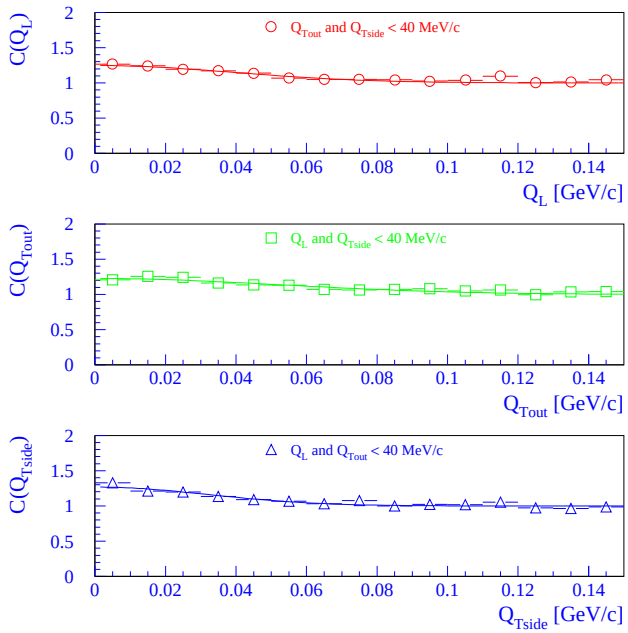

Figure 5.24: *A projection of the correlation function for a limited range of 40 MeV/c in two of the three relative momentum components is made to show the correlation effect in the remaining direction.*

Table 5.8: *Two-dimensional analysis of the transverse (R_T) and longitudinal (R_L) radius for the respective triggers using 3-chamber tracks.*

trigger condition	R_T [fm]	R_L [fm]	λ
central	4.18 ± 0.22	4.47 ± 0.19	0.23 ± 0.02
semi-central	4.03 ± 0.43	3.83 ± 0.55	0.25 ± 0.04
peripheral	2.31 ± 0.18	3.68 ± 0.33	0.24 ± 0.02

transverse momentum of the pion pair.

The limited statistics may cause the loss in correlation strength for the three-dimensional analysis. Furthermore, the larger background both due to the increased K/π and $\bar{p}/\pi$ ratios and the increase of the combinatorial background for large P_T may cause this loss in correlation strength. Note,

Table 5.9: *Three-dimensional analysis of the source radii in the transverse direction, R_{Tout} and R_{Tside}, the longitudinal direction, R_L and the correlation strength λ for the central trigger using 3-chamber tracks.*

trigger condition	R_{Tout} [fm]	R_{Tside} [fm]	R_L [fm]	λ
central	3.61 ± 0.23	2.94 ± 0.12	4.47 ± 0.54	0.26 ± 0.03

see figure 5.25, that the transverse radii for the two-dimensional analysis stay nearly constant at 4 fm whereas the longitudinal radius drops by 2 to 3 fm.

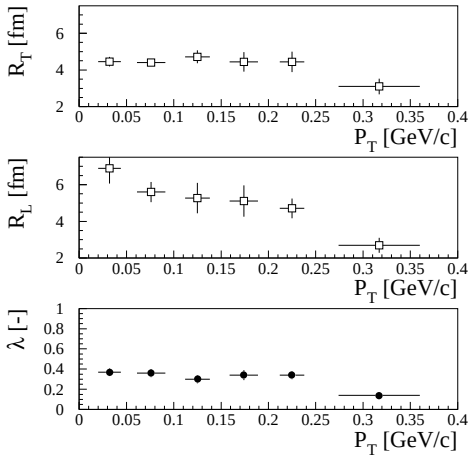

Figure 5.25: *Measured transverse and longitudinal radii and correlation strengths as a function of the transverse momentum of the pion pair for central events using 3-chamber tracks.*

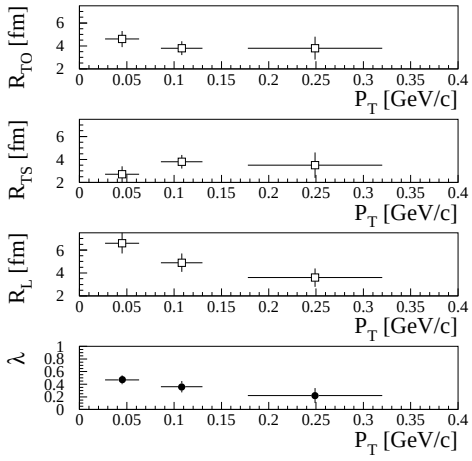

Figure 5.26: *Measured transverse-sideward, transverse-outward and longitudinal radii and correlation strengths as a function of the transverse momentum of the pion pair for central events using 3-chamber tracks.*

In conclusion, we state that a transverse-momentum dependence of both the invariant and longitudinal radius has been observed. The correlation strength tends to decrease for large momenta of the pion pairs due to increased background contributions and limited statistics for the three-dimensional analysis. The background contributions consist both of a decrease

of the π^-/h^- ratio, where h^- are the negatively-charged particles, and the increase of the combinatorial background. This may affect somewhat the decrease of the longitudinal radius. However, as the transverse radius stays rather constant as compared to the longitudinal radius, the observation of a longitudinal expansion is plausible. Furthermore, for the 4-chamber tracks the decrease of the invariant radius is observed even in combination with an increase of the correlation strength and for the 3-chamber tracks the same decrease is observed with a nearly constant correlation strength.

In chapter 6 the measured radii will be compared to other experimental results and a theoretical model based on a one-dimensional hydrodynamic expansion. The time duration of expansion and the particle emission time can thus be estimated and conclusions on the evolving system can be drawn.

Chapter 6

Comparison and Conclusions

In the previous chapters the properties and final results from the data as measured by the charged-particle spectrometer have been described in detail.

The detector limitations at small track distances were overcome by the applied proximity-cut method. In successive steps the momentum resolution, background content, efficiency, and geometrical acceptance were calculated. Thereupon final results could be obtained from single-particle spectra and intensity interferometry.

For the first time Bose-Einstein correlations were shown to be sensitive to the impact-parameter for S+Au reactions. A decrease of the longitudinal and invariant radius for higher transverse momenta of the correlated pairs for central events was observed. In addition, the charged-particle multiplicity spectra showed also an impact-parameter dependence. The transverse-momentum spectra for the respective trigger selections exhibit a similar behaviour with a strong low P_T rise and a slight increase of the apparent temperature for more central collisions. Furthermore, the low P_T rise was shown to be rapidity dependent.

In the following sections the results of the above mentioned topics will be compared to results from other experiments and theoretical models. Especially the comparison to predictions from a one-dimensional hydrodynamical model will yield information on the freeze-out time and time duration of emission of the pions. From such knowledge estimates of the initial energy density and energy density at freeze-out can be made. Then conclusions on the state of created hadronic matter in the collision zone can be drawn.

Table 6.1: *Comparison of the negatively-charged-particle multiplicities to the results from NA35. The selected percentage of the most central collisions is indicated next to the range in rapidity.*

Experiment	System	% σ most central	rapidity	$\frac{dN^-}{dY}_{max}$
WA93	S+Au	16.0	3.0-3.6	57 ± 3
NA35	S+Au	6.3	2.5-4.5	58 ± 2
NA35	S+Ag	3.2	1.8-3.4	45 ± 2
NA35	S+S	3.5	2.5-3.5	26 ± 1

6.1 Multiplicities

The negatively-charged-particle multiplicity was shown to be $dN/dY = 57 \pm 3$ for the central trigger selection. Furthermore, going from peripheral collisions, where $dN/dY = 8 \pm 0.5$, to central collisions a clear increase of the multiplicity for decreasing impact parameter was observed. Such a behaviour is obvious considering the geometrical overlap of the colliding nuclei.

The multiplicity found for the central trigger corresponds very well to the value measured by the NA35 collaboration [51], see table 6.1. The NA35 results were corrected for secondary particle interactions and electron contamination at low P_T. These contributions were shown to be at most 10 % of the total particle content. Note, however, that the WA93 multiplicity data have not been corrected for electron contamination due to lack of particle identification. The inclusion of the time-of-flight wall for particle identification in the WA98 experiment for Pb+Pb collisions is thus highly recommended and valuable. The electron background was estimated from simulations at an average value of 10 % for the transverse-momentum spectrum below $P_T = 0.2$ GeV/c. The region below $P_T = 0.2$ GeV/c contains about 35% of the total measured negative-particle yield, so that the electrons may contribute ≈ 5 % of the total particle content.

Simulations using the VENUS and FRITIOF event generators for the respective impact parameters have been made. The calculated multiplicities are close to the measured values, see table 5.4. In section 6.3 the relation between the measured correlation radii and negatively-charged-particle multiplicities will be presented.

Summarizing, the negatively-charged-particle multiplicities were shown to be both target (NA35/WA93) and impact-parameter dependent (WA93).

6.2 Transverse-Momentum Spectra

Transverse-momentum spectra have been analysed for $P_T < 1.5$ GeV/c both for the 3- and 4-chamber track selection. No significant difference was noticed for these selections after applying the proper corrections for acceptance and background. A parameterization according to the thermal distribution

$$\frac{1}{P_T}\frac{dN}{dP_T} \sim C_1 \cdot \sqrt{m_T \cdot T_1} \cdot e^{-m_T/T_1} + C_2 \cdot \sqrt{m_T \cdot T_2} \cdot e^{-m_T/T_2} \qquad (6.1)$$

with $m_T = \sqrt{m_\pi^2 + P_T^2}$ and assuming all negative particles to be pions, is valid for full coverage in rapidity and yields an inverse slope $T_2 = 220 \pm 3$ MeV for central and $T_2 = 212 \pm 3$ MeV for peripheral reactions in the range $0.2 < P_T < 1.0$ GeV/c. The high P_T slope fits can be compared to neutral pion data near mid-rapidity from the S+Au reaction measured by WA80. Here an increase, however non-significant, from $T = 176 \pm 13$ MeV for peripheral to $T = 192 \pm 5$ MeV for central collisions was observed [28]. Also for the O+Au reaction [95] an increase, however non-significant, from $T = 174 \pm 18$ for peripheral to $T = 194 \pm 22$ for central collisions was measured for neutral pions.

A strong enhancement of the cross-section at low P_T below 0.2 GeV/c is observed. This part of the hadron yield is reproduced using an apparent temperature $T_1 = 23 \pm 1$ MeV for the central and $T_1 = 21 \pm 1$ MeV for the peripheral reactions. The resulting two-slope parameterization is included for the semi-central data in figure 5.17. Furthermore, the low P_T enhancement has been studied for different rapidities. A decrease of the phenomenon towards projectile rapidity was observed; see figure 5.18, for the respective triggers.

Central VENUS events have been simulated for the actual setup using GEANT to investigate possible detector effects and contamination due to various negative particles. VENUS predicts a fraction of 90 % pions for central reactions, whereas electrons contribute in total about 10 % below 0.2 GeV/c and the kaon and anti-proton contribution becomes significant only above 0.2 GeV/c. NA35 [51] measured for $4.2 < Y < 4.4$ an electron contamination of $\approx 10\%$ in the range $0 < P_T < 0.2$ GeV/c. As was pointed out already by Schukraft [96] the identification of pions at low P_T will clarify the low P_T enhancement. The electron content may differ from experiment to experiment due to different target thicknesses. The main electron production mechanisms are γ conversion from π^0 decay and δ-ray electrons in the target and other detector material.

The low P_T rise already has been observed in other concurring experiments [5], NA34 and NA35. The NA34-experiment [96, 97] showed the effect for both π^- and negative hadrons in the target rapidity region $1.0 < Y < 1.9$ for a variety of systems.

Unfortunately the measured strength of the low P_T phenomenon is different for similar experiments. However, since due to the strong rapidity dependence observed in figure 5.18, the coverage in rapidity has to be taken into account.

Ideas to explain the phenomenon have been put forward. Several explanations for the low P_T rise are listed below:

- Coulomb attraction. The investigated particles are negatively charged. The hot reaction zone created in the collision is dominantly positively charged due to the positive charge of both nuclei. Therefore the emitted negative particles will feel a Coulomb attraction from the co-moving positive fragments and thus a shift to low P_T ensues. In ref. [98] Coulomb effects were incorporated for 1 A·GeV beam energies. The model describes the data well with a rise of $\sigma(\pi^-)/\sigma(\pi^+)$ to about 2 for $P_T < 0.2$ GeV/c. Recently a difference was observed in the comparison of the low P_T enhancement for positive and negative pions from 14.6 A·GeV Au+Au collisions [40]. This difference is likely to originate from Coulomb effects.

- Rescattering and cascading of produced particles in the target nucleus yielding additional soft pions and resonances.

- Resonances. In the collision zone many resonances, like the Δ and lower mass mesons ρ, ω, η, K^* [99], will be excited. In the decay of these resonances, e.g. Δ-decay, the produced pions will be emitted with a low transverse momentum. Note that the Δ decays in the medium as its lifetime $\tau \approx 5 \cdot 10^{-24}$ s is short.

  For example NA34 measured for S+W a soft component comprising 40% of the pion content with a momentum distribution similar to the Δ decay [5]. NA35 observed 30% for the soft component in O+Au reactions. The calculated negatively-charged-particle content below $P_T = 0.2$ GeV/c for the WA93 S+Au data is 35 % for the respective trigger selections.

  In the 14.6 A·GeV Si+Pb, Si+Al and Au+Au experiment E814 [19, 40] the low P_T enhancement for π^- and π^+ is observed for $3.1 < Y < 4.3$. The E814 experiment also observed a rapidity dependence of the low

P_T enhancement. Towards projectile rapidity the phenomenon decreases. A similar behaviour was noticed for the WA93 S+Au reaction; see figure 5.18. The E814 results are consistently described by a 33% fraction of the total number of pions from Δ-decay and a freeze-out temperature of $T_f = 140$ MeV. According to the thermodynamic weight factors $e^{-m_\Delta/T_2} \cong e^{-m_\pi/T_1} \cong e^{-1200/200} \cong e^{-140/24} \cong e^{-6}$ derived from the WA93 results we find that the Δ and π are in chemical equilibrium.

- The implementation of Bose-Einstein correlations of emitted pions in the FRITIOF event generator [100] shows a minor enhancement at low P_T of at most a factor 1.2.
- Critical scattering [39] leads to a faster production of low-momentum pions and therefore to an intermediate non-thermal distribution. The pions which escape to the detector, before thermal equilibration of the hadron gas sets in, can be observed as an enhancement at low momenta of the pion distribution.

Other exotic explanations such as creation of small plasma droplets [101], transverse flow[102], formation of the pion system out of chemical equilibrium [103] and the medium modification of the pion dispersion relation [104] may also play a role. Note that transverse-flow models have great difficulty in describing the low P_T data as they generally lead to a depletion at low P_T.

Summarizing, the low P_T enhancement was observed for the respective trigger selections and exhibited a rapidity dependence. A valid explanation for such a behaviour is large stopping and Δ-resonance production at mid-rapidity. The other described explanations may add to this, although these models have great difficulty in explaining the rapidity dependence and the absence of impact-parameter dependence.

6.3 Intensity-Interferometry

The results of one-, two- and three-dimensional intensity interferometry have been presented in sections 5.2.1 and 5.2.2, respectively.

These studies were made as a function of the transverse momentum of the correlated pairs to investigate the dynamical evolution of the source with respect to a possible first-order phase transition.

The correlation strength was in general low, $\lambda \approx 0.3$, using 3-chamber tracks. Besides the well-known effects due to non-pion tracks and pions from

low-mass meson-resonance decays [99], the combinatorial background causes an extra decrease of the correlation strength.

The measured radii showed a dependence on the impact parameter of the collision. Such a behaviour is obvious from a geometrical picture of overlapping nuclei in the collision. However, it would be interesting to verify these results by comparison with other experiments and predictions from theoretical models and event generators.

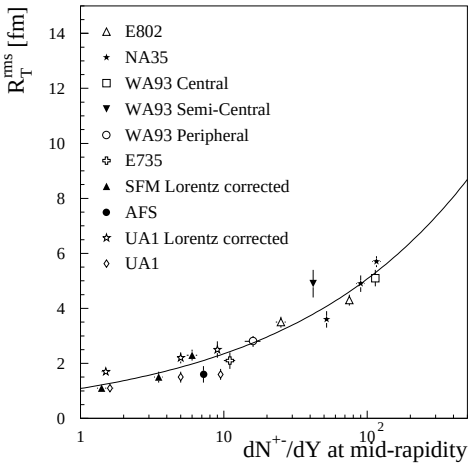

Figure 6.1: *The measured rms value for the transverse radius R_T in several experiments versus the measured maximum charged-particle multiplicity dN^{+-}/dY at mid-rapidity.*

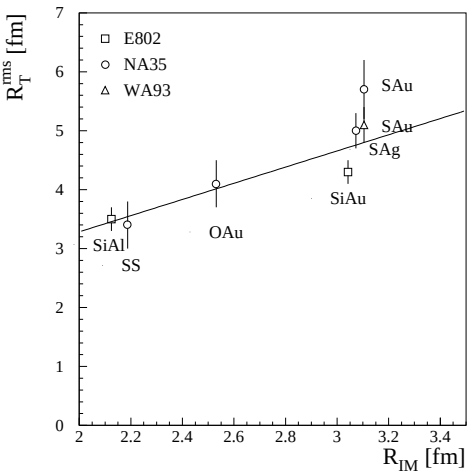

Figure 6.2: *The measured rms value for the transverse radius R_T in several experiments versus the calculated rms value of the interacting-matter radius for the colliding nuclei.*

A simple model describing the freeze-out mechanism when the mean free path of the particles equals the source radius, see section 2.7, predicts

$$R_T \sim \sqrt{\frac{dN}{dY}} \tag{6.2}$$

whereas another model with the assumption of constant freeze-out density and R_T to represent the geometrical source radius predicts

$$R_T \sim \frac{dN}{dY}^{1/3} \tag{6.3}$$

Here, the measured transverse radius R_T represents the freeze-out radius R_f at the moment of freeze-out. In figure 6.1, the WA93 data points have been

presented together with a compilation of data points from other experiments. Here, the rms radii R_T^{rms} are depicted where the relation $R_T^{rms} = \sqrt{\frac{3}{2}} \cdot R_T$ holds for the WA93 data points [105]. The R_T^{rms} radii for the three different trigger selections fit into the general trend. So there seems to be no strong dependence of the interaction volume on the centrality of the collision as expected in case of complete thermalization in central reactions. A fit according to $R_T \sim \frac{dN}{dY}^{\alpha}$ yields information on the freeze-out mechanism. The resulting $\alpha = 0.336 \pm 0.009$ is clearly in favour of a freeze-out model at constant pion density. A confirmation of the constant pion density at freeze-out was presented by NA35 in [41].

Furthermore, the measured transverse radius in central reactions can be studied as a function of the radius of the interacting matter according to a geometrical model [106], see figure 6.2. This model uses the nuclear-density functions of the target and projectile nucleus. A linear fit to the data yields $R_T^{rms} = 1.4 \cdot R_{IM}$. Explanations for the observed slope parameter > 1 may be rescattering in the spectator zone of the target nucleus or transverse expansion.

The above studies were made under the assumption of static sources. Suppose this is valid and that such a static source is moving with certain rapidity. The observed longitudinal radius would then be reference-frame dependent. Selections on the transverse momenta of the pion pairs would yield identical longitudinal radii. However, the nuclear matter in the collision zone is highly compressed in the longitudinal direction. Bjorken [16] described the evolution of the collision zone for one-dimensional longitudinal hydrodynamical expansion. In ref. [107] the consequences of one-dimensional hydrodynamical expansion for the pion interferometry were derived. The source is thought to consist of fluid elements with a flow velocity $u(x)$ at position x. The fluid elements are in local thermodynamic equilibrium at a temperature T. From the fluid elements pions are emitted with momentum p at a certain time t. The relativistic Boltzmann distribution for the pions is given by

$$f(p,x) = C \cdot e^{-p \cdot u(x)/T} \tag{6.4}$$

where the freeze-out temperature is denoted by T. In case of one-dimensional expansion the four-velocity of the expanding matter at position x is given by the scaling Bjorken expansion [16] as

$$u(x) = (t/\tau, 0, 0, r_z/\tau) = (\cosh(\eta), 0, 0, \sinh(\eta)) \tag{6.5}$$

where $\tau = \sqrt{t^2 - r_z^2}$ is the longitudinal proper time, r_z the related point along the z-axis and $\eta = 0.5 \cdot ln((t + r_z)/(t - r_z))$ the space-time rapidity.

Since the four-momentum p can be written as $p = (m_T \cdot \cosh(Y), P_T, m_T \cdot \sinh(Y))$ the relativistic Boltzmann distribution for one-dimensional expanding systems can be rewritten as

$$f(p,x) = C \cdot e^{-\frac{m_T \cdot \cosh(\eta - Y)}{T}} \tag{6.6}$$

The longitudinal radius measured by intensity interferometry in case of only longitudinal flow, as expressed by the equation above, was derived by Mahklin and Sinyukov [107, 108, 109] to be

$$R_L = \tau_f \cdot \sqrt{\frac{2T_f}{< m_T >}} \cdot \cosh(\delta Y)^{-1} \tag{6.7}$$

where δY is the rapidity of the particles with respect to the frame at mid-rapidity, $< m_T >$ the average transverse-mass, T_f the freeze-out temperature and τ_f the freeze-out time. A selection on rapidity was made by NA35 [51, 94] and showed a behaviour according to the above equation for the longitudinal radius with a plateau at mid-rapidity. The transverse radii did not show a rapidity dependence.

The consequences of the finite size of the source in space-time rapidity $\Delta\eta$, the geometrical source size, was taken into account by Csörgo [50]

$$R_L = \tau_f \cdot \sqrt{\frac{2T_f}{< m_T >}} \cdot \frac{1}{\sqrt{1 + \frac{T_f}{< m_T > \cdot \Delta\eta^2}}} \cdot \cosh(\delta Y)^{-1} \tag{6.8}$$

which approaches the derivation of Mahklin and Sinyukov for an infinite extension of the cylinder of interacting matter ($\Delta\eta \rightarrow \infty$) as assumed in the Bjorken model, see section 2.1. In case the $\sqrt{m_T}$ behaviour describes the data rather well we may conclude a relatively cold and large system [50, 109]. The so-called thermal-source radius has been measured. In case the system exhibits no m_T dependence the conclusion of a hot and small observed system with $R_L(m_T) = \sqrt{2} \cdot \tau_f \cdot \Delta\eta$ at mid-rapidity can easily be derived from equation 6.8. The geometrical source size has then been measured. Furthermore, Csörgö advocated to study the dependence of the rapidity width ΔY on the transverse momentum for the invariant single-particle distribution $d^2N/dYdm_T^2$

$$\Delta Y^2(m_T) = \Delta\eta^2 + \frac{T_f}{m_T} \tag{6.9}$$

From such an analysis the geometrical size $\Delta\eta$ and the freeze-out temperature T_f can be determined. The freeze-out time can then be determined

from the correlation analysis. The importance of wide-acceptance detectors is immediately clear from equation 6.9.

Due to the limited acceptance $3.0 < Y < 3.6$ of the WA93 spectrometer we were restricted to study the dependence of the longitudinal radius on the average transverse momentum of the pion pair. Note that the low P_T enhancement will influence the rapidity width which was not taken into account in Csörgö's derivation [50].

The maximum longitudinal radius $R_L(Y_0) \approx 5$ fm derived by NA35 in the observer frame at mid-rapidity $Y_0 = 2.5$ was shifted to the observer frame of WA93 at $Y = 3.02$ according to [109]

$$R_L^*(Y) = \frac{R_L(Y_0)}{cosh(Y - Y_0)} \cdot \frac{dN/dY(Y)}{dN/dY(Y_0)} \tag{6.10}$$

This equation is based on maintaining a constant particle density independent of the observer frame. The resulting NA35 radius is $R_L^* = 4.3 \pm 0.1$ fm which compares rather well to the WA93 value $R_L = 4.47 \pm 0.27$ fm.

A parameterization according to the longitudinal flow model has been attempted for the invariant radius, which is dominated by the behaviour of R_L in case of longitudinal flow.

$$R_{inv} = \tau_f \sqrt{\frac{2T_f}{m_T}} \tag{6.11}$$

with freeze-out time τ_f and freeze-out temperature T_f, see also equation 6.8. The fit is included in figure 6.3. A freeze-out temperature in the range between the pion mass [19] ($T_f = 140$ MeV) and an upper limit as given by the fitted apparent temperature of the pion spectrum ($T_f = 220$ MeV) leads to corresponding freeze-out times in the range from $\tau_f = 3.5 \pm 0.1$ fm/c to $\tau_f = 2.8 \pm 0.1$ fm/c. These values are short if compared to the value $\tau_f = 15$ fm/c expected for a first-order phase transition with a freeze-out temperature of 140 MeV; see section 2.1.

The multi-dimensional correlation analysis with a selection on the transverse momentum leads to the observation of a decrease of the longitudinal radius. The transverse radii stay nearly constant, see figure 6.4. The analysis according to the longitudinal hydrodynamical expansion model as given by the equation 6.8 leads to $\tau_f = 4.1 \pm 0.2$ fm/c for $T_f = 140$ MeV and $\tau_f = 3.5 \pm 0.2$ fm/c for $T_f = 220$ MeV. Again rather short expansion times are observed.

The two transverse radii measured for the three-dimensional analysis, R_{Tout} and R_{Tside}, show no large difference as a function of the transverse

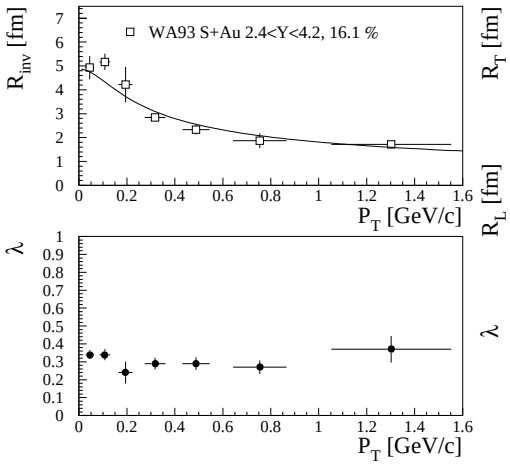

Figure 6.3: *Dependence of the invariant radius and correlation strength on the transverse momentum of the correlated pair. A decrease of the invariant radius for increasing P_T is observed. The line shows the fit to the data points.*

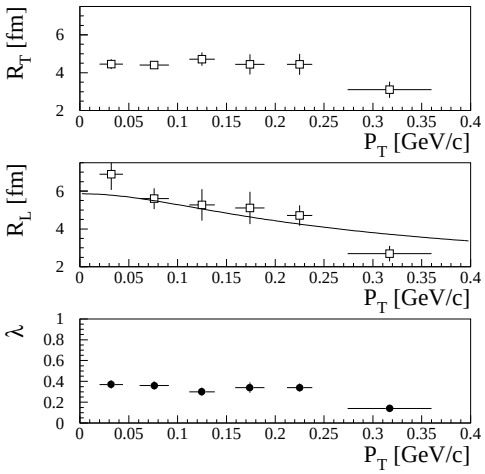

Figure 6.4: *The radius parameters R_T, R_L, and the correlation strength λ as a function of the transverse momentum of the pair.*

momentum. Similar observations have been made for other experiments, e.g. NA35 [51, 106] and NA44 [110]. The time duration of emission, see section 2.8.2, must be small, $\Delta\tau < 2$ fm/c, as the average difference in $\sqrt{R^2_{Tout} - R^2_{Tside}} < 2$ fm.

The observed transverse-momentum dependence of the longitudinal- and invariant-radius parameters indicates a scenario of a longitudinally expanding and cooling hadronic gas. The decrease of the invariant radius and longitudinal radius can be well described by a $1/\sqrt{m_T}$ dependence. The observed short freeze-out time of about 4 fm/c together with the observed behaviour of the transverse-radius components does not favour a first-order quark-gluon phase transition for 200 GeV S+Au reactions.

A rough estimate for the energy density in the Bjorken picture of the collision was presented in section 2.1. In case that only negative hadrons are measured we calculate the energy density from

$$\epsilon = \frac{3 \cdot \frac{dN}{dY}^{-} \cdot < E_T >}{\pi \cdot R_T^2 \cdot c \cdot \tau} \tag{6.12}$$

The average measured transverse momentum for the central trigger was

$< P_T >= 0.45$ GeV/c in the studied range $0 < P_T < 1.5$ GeV/c. This leads to an average transverse energy $< E_T >= 0.47$ GeV, under the assumption that all negatively-charged particles are pions. A generally observed value for the average transverse energy in these heavy-ion reactions is $E_T = 0.5$ GeV [5]. According to the measured values for $\frac{dN}{dY}^- = 60$, $< E_T >= 0.5$ GeV and $R_T = 4$ fm an estimate for the initial energy density ϵ_i based on a formation time $\tau_i = 1$ fm/c, and for the freeze-out energy density ϵ_f based on a freeze-out time $\tau_f = 4$ fm/c can be made. These values result in an initial energy density $\epsilon_i = 1.8$ GeV/fm^3 and a freeze-out energy density $\epsilon_f = 0.45$ GeV/fm^3.

A hot hadronic gas has thus been created at the limits of the phase transition and evolved to a freeze-out density at a density three times the nuclear-matter density ≈ 0.15 GeV/fm^3.

6.4 Outlook

From the first experiments with relatively light ions at the AGS at Brookhaven and the SPS at CERN up to now there has been a continuous development both on the experimental and theoretical side.

The analysed data from the Charged-Particle Spectrometer clearly show the need for particle identification. Particle identification will facilitate the study of pion correlations and also enable the study of kaon-correlations. The correlation strength will then increase and the interpretation of the correlation radii becomes less ambiguous. Furthermore, particle identification will facilitate the understanding of the measured single-particle spectra. Corrections for the electron contamination based on simulations are always model dependent. Particle identification will enable proper removal of this component. The low P_T enhancement can thus be verified for negative hadrons and studied for a selection on particle species. As kaons are less likely to originate from resonance decay the comparison of pion and kaon transverse-momentum spectra might shed light onto how strongly resonance decays influence this effect. Measurements of positive pions can test the Coulomb effect at low P_T. A remaining low P_T enhancement for π^+ would strongly favour the resonance picture. The recent observation of the low P_T enhancement at AGS energies for both negative and positive pions [40] provides already the first indication for the resonance picture.

In addition to particle identification wide acceptance detectors are strongly needed. The analysis proposed by Csörgö [50] of the rapidity width as a function of the transverse mass in addition to the pion interferometry

will clarify the interpretation of the measured source radii and the deduced expansion times.

The combinatorial background was high for 3-chamber tracks and was shown to be reduced largely for 4-chamber tracks. An extension of the tracking capabilities with more position-sensitive detectors could greatly improve upon reducing this background contribution and furthermore increase the tracking efficiency.

The newly developed prototype PAD chamber has been shown to have a very high efficiency. In addition, the lower gain at which this device can be operated decreases the sparking probability. The expected absence of satellite hits for such a detector would greatly facilitate the data analysis. The restrictive cuts on the two-track distance can then be reduced. A high number of reconstructed tracks per event would largely increase statistics and enable a more restrictive selection on very central events or high photon multiplicity events.

With the extension of the WA93 experiment to 6 MSAC tracking chambers and a time-of-flight detector and a second tracking arm for positively charged particles using PAD chambers the WA98 Pb+Pb experiment has largely fulfilled the needs mentioned above. The first data from the most recent Pb+Pb experiment in 1995 are currently being analysed and more data are expected from runs in 1995 and 1996.

In the near future Pb+Pb collisions will take place in the LHC collider at a nucleon-nucleon center of mass energy of $\sqrt{s} = 6300$ GeV. Up to several thousands of particles are expected to be measured per event. The average created energy density per event $\epsilon = 7.8$ GeV/fm^3 [111] and the improved detector resolutions may allow to catch a first glimpse of the quark-gluon plasma.

References

[1] S. Abachi et al. Observation of the Top Quark. *Phys. Rev. Lett.*, 74:2632, 1995.

[2] F. Abe et al. Observation of Top Quark Production in $\bar{p}p$ Collisions with the Collider Detector at Fermilab. *Phys. Rev. Lett.*, 74:2672, 1995.

[3] H. Satz. The limits of hadron thermodynamics. 1984. Invited Lecture, CERN, May 19, 1984.

[4] J.L. Mahler et al. Results from Cobe. *App. J. Lett.*, 354:137, 1990.

[5] H.R. Schmidt and J. Schukraft. The physics of ultra-relativistic heavy-ion collisions. *J. Phys. G.*, 19:1705–1795, 1993.

[6] C.P. Singh. Signals of quark-gluon plasma. *Phys. Lett.*, 236:147–224, 1993.

[7] L.P. Csernai. Introduction to Relativistic Heavy Ion Collisions. *John Wiley & Son, Chichester*, 1994.

[8] C. Wong. Introduction to High-Energy Heavy-Ion Collisions. *World Scientific, Singapore*, 1994.

[9] T.D. Lee. RHIC and QCD: an overview. *Nucl. Phys. A*, 590:11c–28c, 1995.

[10] B. Müller. The Physics of the Quark-Gluon Plasma. *Springer-Verlag, Berlin, Lecture Notes in Physics*, 225, 1985.

[11] A. Chodos et al. New extended model of hadrons. *Phys. Rev. D*, 9:3471–3500, 1974.

[12] R. Hanbury Brown and R.Q. Twiss. A New Type of Interferometer for Use in Radio Astronomy. *Phil. Mag.*, 45(366):663–682, 1954.

[13] G. Goldhaber et al. Pion-pion correlations in antiproton annihilation events. *Phys. Rev. Lett.*, 3(4):181–183, 1959.

[14] H. Satz. Probing the primordial state in high energy heavy-ion collisions. *CERN-TH*, 6666/92, 1992.

[15] J. Stachel and P. Braun-Munzinger. Stopping in high energy nucleus-nucleus collisions. Analysis in the Landau hydrodynamical model. *Phys. Lett. B*, 216:1–6, 1989.

[16] J.D. Bjorken. Highly relativistic nucleus-nucleus collisions: The central rapidity region. *Phys. Rev. D*, 27:140–151, 1983.

[17] R. Albrecht et al. Upper limit for thermal direct photon production in heavy-ion collisions at 60 and 200 A·GeV. *Z. Phys. C*, 51:1–10, 1991.

[18] D.K. Srivastava and B. Sinha. Single photons from S + Au collisions at the CERN Super Proton Synchrotron and the quark-hadron phase transition. *Phys. Rev. Lett.*, 73:2421–2424, 1994.

[19] J. Barrette et al. Measurement of Pion Enhancement at Low Transverse Momentum and of the Δ Resonance Abundance in Si-Nucleus Collisions at AGS Energy. *Phys. Lett. B.*, 351:93–98, 1995.

[20] M. Strickland. Thermal photons and dileptons from non-equilibrium quark-gluon plasma. *Phys. Lett. B*, 331:245–250, 1994.

[21] M. Neubert. Photon production in ultrarelativistic heavy-ion collisions at 200 GeV/n. *Z. Physik C*, 42:231–242, 1989.

[22] J. Kapusta et al. High-energy photons from quark-gluon plasma versus hot hadronic gas. *Phys. Rev. D*, 44:2774–2788, 1991.

[23] R. Baier et al. Production rate of hard thermal photons and screening of quark mass singularity. *Z. Phys. C*, 53:433–438, 1992.

[24] R.C. Hwa and K. Kajantie. Diagnosing quark matter by measuring the total entropy and the photon or dilepton emission rates. *Phys. Rev. D*, 32:1109–1118, 1985.

[25] P.V. Ruuskanen. Electromagnetic probes of quark-gluon plasma in relativistic heavy-ion collisions. *Nucl. Phys. A*, 544:169c–182c, 1992.

[26] H. Löhner. Photon and meson production in ultra-relativistic nucleus-nucleus collisions. *Perspectives in the Structure of Hadronic Systems, Plenum Press, New York*, pages 213–234, 1994.

[27] G. Clewing. Untersuchungen zur Produktion direkter Photonen in ultrarelativistischen Schwerionenreaktionen bei 200 A GeV. *PhD thesis, Univ. Münster*, 1993.

[28] G. Hölker. Produktion inklusiver Photonen und neutraler Pionen in ultrarelativistischen Schwerionenreaktionen. *PhD thesis, Univ. Münster*, 1993.

[29] T.C. Awes et al. Search for direct photon production in 200 A GeV S+Au reactions: A status report. *Nucl. Phys. A*, 590:81c–92c, 1995.

[30] R. Albrecht et al. Limits on the Production of Direct Photons in 200 A GeV ^{32}S+Au collisions. *Letter-draft, submitted to Phys. Lett. B*, 1995.

[31] A. Drees. First Results of the CERES Electron Pair Spectrometer from p+Be, p+Au and S+Au collisions. *Nucl. Phys. A*, 566:87c–94c, 1994.

[32] P. Wurm et al. New Results from NA45/CERES. *Nucl. Phys. A*, 590:103c–116c, 1995.

[33] G.E. Brown et al. Strangeness production in relativistic heavy-ion collisions. *Z. Physik A.*, Vol. 341:301–305, 1992.

[34] C. Greiner et al. Strange matter - a new domain of nuclear physics. *Nucl. Phys. A*, 566:157c–166c, 1994.

[35] H. Satz. Heavy ion physics at very high energies. *CERN-TH*, 5917, 1990.

[36] H. Satz. Hard probes of dense matter. *Nucl. Phys. A*, 590:63c–80c, 1995.

[37] M.C. Abreu et al. J/ψ and ψ' and muon pair production in p-W and S-U collisions. *Nucl. Phys. A*, 566:77c–86c, 1994.

[38] R.V. Gavai and R.M. Godbole. Sizing up the Nuclear Glue in J/ψ-production. *Nucl. Phys. A*, 566:375c–378c, 1994.

[39] J. Dolejší et al. Critical scattering at the chiral phase transition and low-P_T enhancement of mesons in ultra-relativistic heavy-ion collisions. *Phys. Lett. B*, 349:18–22, 1995.

[40] J. Barrette et al. Directed flow and particle production in Au+Au collisions from experiment E877 at the AGS. *Nucl. Phys. A*, 590:259c–270c, 1995.

[41] M. Gaździcki et al. Recent results from NA35. *Nucl. Phys. A*, 590:197c–214c, 1995.

[42] R. Hanbury Brown and R.Q. Twiss. The question of correlation between photons in coherent light rays. *Nature*, 170:1447–1450, 1956.

[43] G. Goldhaber et al. Influence of Bose-Einstein Statistics on the Anti-Proton Annihilation Process. *Phys. Rev.*, 130(1):300–312, 1960.

[44] E.V. Shuryak. Correlations of identical pions in multiple production reactions. *Sov. J. Nucl. Phys.*, 18(6):667–670, 1973.

[45] G. Cocconi. Second-Order Interference as a tool for the determination of hadron fireball dimensions. *Phys. Lett.*, 49B(5):459–461, 1974.

[46] M. Gyulassy et al. Pion interferometry of Nuclear collisions. I. Theory. *Phys. Rev. C*, 20:2267–2187, 1979.

[47] W.A. Zajc et al. Two-pion correlations in heavy-ion collisions. *Phys. Rev. C*, 29:2173–2187, 1984.

[48] Y. Schutz. The Principle of the HBT effect and its applications in Nuclear Physics. *GANIL preprint*, 22, 1990.

[49] T. Csörgö et al. Quantum statistical correlations for slowly expanding systems. *Phys. Lett. B*, 338:134–140, 1994.

[50] T. Csörgö. Bose-Einstein correlations for longitudinally expanding, finite systems. *Phys. Lett. B*, 347:354–360, 1995.

[51] G. Roland. Teilchenproduktion und Teilchenkorrelationen in der Vorwärtshemisphäre von Schwefel-Kern Stössen bei 200 GeV/Nukleon. *PhD thesis, Univ. Frankfurt*, 1992.

[52] W.A. Zajc. A pedestrians guide to interferometry. *Columbia Univ. preprint*, 1992.

[53] R.M. Weiner. Hadron Interferometry Revisited. *Phys. Lett. B*, 232:278–282, 1989.

[54] T. Peitzmann. The correlation strength in pion interferometry. *Z. Phys. C*, 55:485–489, 1992.

[55] D. Anchishkin and G. Zinovjev. Two-pion correlation behavior in a small relative momentum region. *Phys. Rev. C*, 51:2306–2309, 1995.

[56] F. Sauli et al. Proposal for a light universal detector for the study of correlations between photons and charged particles. *CERN/SPSC*, P252, 1990.

[57] P. Dönni et al. Proposal for a large acceptance hadron and photon spectrometer. *CERN/SPSLC*, P260, 1991.

[58] E. Gatti and P. Rehak. Semiconductor Drift Chamber - An application of a novel charge transport scheme. *Nucl. Instr. Meth.*, 225:608–614, 1984.

[59] G. Hall. Silicon drift chambers. *Nucl. Instr. Meth.*, 273:559–564, 1988.

[60] W. Verkerke. Charged Particle Veto in WA93. *diploma thesis, Univ. Utrecht*, 1993.

[61] M. Iźycki et al. A large multistep avalanche chamber: description and performance. *Univ. Geneva, preprint*, 10-144, 1990.

[62] A.L.S. Angelis et al. Large parallel plate avalanche chambers for multiparticle tracking. *Nucl. Phys. A*, 566:605c–610c, 1994.

[63] N. Solomey. Development and utilization of a light chamber tracking system in a heavy ion experiment performing two pion interferometry. *PhD thesis, Univ. Geneva*, 1992.

[64] S. Slegt. Momentum Distributions and Interferometry Analysis of Negatively Charged hadrons from 200 A GeV S+Au reactions. *Nucl. Phys. A*, 590:469c–472c, 1995.

[65] G. Charpak et al. The use of multiwire proportional counters to select and localize charged particles. *Nucl. Instr. Meth.*, 62:262–268, 1968.

[66] G. Charpak et al. An optical, proportional, continuously operating avalanche chamber. *Nucl. Instr. Meth.*, A258:177–184, 1987.

[67] G. Charpak. Wire chambers for exploring the elementary constituents of matter. *Europhys. News*, 23:184–186, 1992.

[68] W.R. Leo. Techniques for Nuclear and Particle Physics Experiments. *Springer Verlag, Berlin*, 1992.

[69] F. Sauli. Applications of gaseous detectors in astrophysics, medicine and biology. *Nucl. Instr. and Meth.*, A323:1–11, 1993.

[70] R. Chechik and A. Breskin. On the properties of low-pressure TMAE-filled multistep UV-photon detectors. *Nucl. Instr. Meth.*, A264:251–262, 1988.

[71] D. Sauvage et al. A systematic study of the emission of light from electron avalanches in low-pressure TEA and TMAE gas mixtures. *Nucl. Instr. Meth.*, A275:351–363, 1989.

[72] G. Charpak et al. Studies of light emission by continuously sensitive avalanche chambers. *Nucl. Instr. Meth.*, A269:142–148, 1988.

[73] V. Peskov et al. Investigation of light emission from a parallel-plate avalanche chamber filled with noble gases with TEA, TMAE, and H_2O vapours at atmospheric pressure. *Nucl. Instr. Meth.*, A277:547–556, 1989.

[74] P. Fonte et al. VUV emission and breakdown in parallel-plate chambers. *Nucl. Instr. and Meth.*, A310:140–145, 1991.

[75] S. Louw. Performance of a multistep avalanche chamber with electronic pad readout. *diploma thesis, KVI Groningen*, 1994.

[76] K. Werner. Strange particle enhancement in heavy ion collisions. *Nucl. Phys. A*, 544:593c–598c, 1992.

[77] C. d'Ambrosio et al. Optimization of central particle tracking at future hadron colliders. *Nucl. Instr. and Meth.*, A322:20–33, 1992.

[78] H. Grote and M. Metcalf. PATCHY Reference Manual. *CERN Program Library, Geneva*, 1988.

[79] R. Brun et al. HBOOK, CERN Program Library, Long Writeup Y250, Reference Manual Version 4.20.

[80] R. Brun et al. PAW, CERN Program Library, Long Writeup Q121, Version 1.14, Physics Analysis Workstation.

[81] GEANT team. GEANT 3.15 CERN user's guide.

[82] H. Sorge et al. Poincaré invariant hamiltonian dynamics modelling multi-hadronic interactions in a phase space approach. *Ann. Phys.*, 192:266–306, 1989.

[83] B. Nilsson-Almqvist et al. Interactions between hadrons and nuclei: The Lund Monte Carlo-Fritiof version 1.6. *Comp. Phys. Comm.*, 43:387–397, 1987.

[84] T.C. Awes et al. A simple method of shower localization and identification in laterally segmented calorimeters. *Nucl. Instr. Meth.*, A311:130–138, 1992.

[85] M. Gyulassy and M. Harlander. Elastic tracking and neural network algorithms for complex pattern recognition. *LBL preprint*, 29654, 1990.

[86] G. Athanasiu et al. Real time pattern recognition with artificial networks. *CERN-PPE*, 92-86, 1992.

[87] S. Garpman. Private communication, Univ. of Lund. 1995.

[88] K.E. Atkinson. An introduction to numerical analysis. *John Wiley & Sons*, 1989.

[89] W.S.C. Williams. Nuclear and Particle Physics. *Oxford Science Publications, Oxford*, 1992.

[90] K. Werner. The string model of nuclear scattering: Theoretical concepts. *Perspectives in the Structure of Hadronic Systems, Plenum Press, New York*, pages 259–286, 1994.

[91] S. Pratt. Pion interferometry of quark-gluon plasma. *Phys. Rev. D*, 33:1314–1327, 1986.

[92] G. Bertsch and G.E. Brown. Temporal development of the plasma phase transition. *Phys. Rev. C*, 40:1830–1832, 1989.

[93] W.L.T.P. Lavrijsen and B. Raeven. Determination of the impact parameter for ultra-relativistic S-S and S-Au collisions. *diploma thesis, Univ. of Utrecht*, 1995.

[94] T. Alber et al. Two-pion Bose-Einstein correlations in nuclear collisions at 200 GeV per nucleon. *Z. Phys. C*, 66:77–88, 1995.

[95] R. Albrecht et al. Transverse momentum distributions of neutral pions from central and peripheral ^{16}O+Au collisions at 200 AGeV. *Z. Phys. C.*, 47:367–375, 1990.

[96] J. Schukraft. Review of transverse-momentum distributions in ultra-relativistic nucleus-nucleus collisions. *CERN-PPE*, 91-04, 1991.

[97] T. Åkesson et al. Inclusive negative particle P_T spectra in p-nucleus and nucleus-nucleus collisions at 200 GeV per nucleon. *Z. Phys. C*, 46:361–367, 1990.

[98] Bao-An Li. Revisit of Coulomb effects on π^-/π^+ ratio in heavy ion collisions. *Phys. Lett. B*, 346:5–8, 1995.

[99] R. Lednicky and T.B. Progulova. Influence of resonances on Bose-Einstein correlations of identical pions. *Z. Phys. C*, 55:295–305, 1992.

[100] K. Kadija and P. Seyboth. The nonstatistical fluctations and low P_T phenomena caused by Bose-Einstein correlations. *Phys. Lett. B*, 287:363–367, 1992.

[101] L. Van Hove. *CERN preprint*, TH-5236/88, 1988.

[102] K. Lee et al. Search for collective transverse flow using particle transverse momentum spectra in relativistic heavy-ion collisions. *Z. Phys. C*, 48:525–541, 1990.

[103] M. Kataja and P.V. Ruuskanen. Non-zero chemical potential and the shape of the P_T distribution of hadrons in heavy-ion collisions. *Phys. Lett. B*, 243:181–184, 1990.

[104] E.V. Shuryak. Physics of the pion liquid. *Phys. Rev. D*, 42:1764–1776, 1990.

[105] B.V. Jacak et al. Recent Results from NA44 and a review of HBT. *Nucl. Phys. A*, 590:215c–232c, 1995.

[106] P. Seyboth. Recent results from experiment NA35. *Nucl. Phys. A*, A544:293c–308c, 1992.

[107] A.N. Mahklin and Yu.M. Sinyukov. The hydrodynamics of hadron matter under a pion interferometric microscope. *Z. Phys. C*, 39:69–73, 1988.

[108] Yu.M. Sinyukov. Hanbury Brown-Twiss correlations for expanding hadron and quark-gluon matter. *Nucl. Phys. A*, 498:151c–160c, 1989.

[109] B. Lörstad and Yu.M. Sinyukov. Pion interferometry testing the validity of hydrodynamical models. *Phys. Lett. B*, 265:159–166, 1991.

[110] H. Beker et al. m_T Dependence of Boson Interferometry in Heavy Ion Collisions at the CERN SPS. *Phys. Rev. Lett.*, 74:3340–3343, 1995.

[111] H. Satz. High energy nuclear collisions: Probing the states of matter in qcd. *CERN-TH*, 6216/91, 1991. Plenary talk given at the Joint International Lepton-Photon Symposium and Europhysics Conference on High Energy Physics, Geneva, Switzerland, July 25 - August 1, 1991.

Samenvatting

De fase-overgang van vrije quark-deeltjes, aanwezig kort na de oerknal in het vroege heelal, naar de toestand van gebonden quarks, welke de huidige materie in atoomkernen kenmerkt, wordt met hoog energetische kern-kern-botsingen onderzocht. De meting van de ruimte-tijd evolutie van deze "kleine oerknal"in het laboratorium met een "pion-microscoop"geeft informatie over de fase-toestand.

Op moleculair niveau zijn fase-overgangen algemeen bekend. Voorbeelden hiervan zijn het verdampen van water (vloeistof $\rightarrow$ gas) en het smelten van ijs (vast $\rightarrow$ vloeistof). Op het niveau van de materie in atoomkernen, de kernmaterie, waren soortgelijke fase-overgangen zo'n dertig jaar geleden nog onbekend.

In de loop van deze eeuw zijn door de ontwikkeling van deeltjes-versnellers steeds kleinere structuren van materie aangetoond. De atomen (10^{-10} m) bleken kernen (10^{-14} m) met electronen in banen daaromheen. De kernen zijn uit nucleonen (10^{-15} m), te weten protonen en neutronen, opgebouwd. De nucleonen op hun beurt bleken uit quark-deeltjes ($\leq 10^{-17}$ m) te bestaan.

Met de ontdekking van de quark-structuur van het nucleon in 1968 voltrok zich een revolutie op het gebied van de theorie aangaande de sterke kernkracht. Deze theorie welke uitgaat van quarks en gluonen (lijmdeeltjes) als kleinste bouwstenen van kernmaterie (hadronen) wordt de Quantum Chromo Dynamica (QCD, chromo = kleur) genoemd. Quarks hebben in deze theorie naast een electrische lading ook een kleur-lading, te weten rood, blauw of groen. De QCD voorspelt een fase-overgang van een kleurloze toestand van gebonden quarks in kernmaterie naar een toestand van vrije kleur dragende quarks, het zogenaamde Quark-Gluon Plasma (QGP), bij zowel hoge temperaturen als dichtheden. Overeenkomstig met het geleidend worden van half-geleider materialen wordt een kleur-lading-isolator een kleur-lading-geleider. Het vroege hete heelal heeft zeer waarschijnlijk een soortgelijke fase-overgang zo'n $20 \cdot 10^{-6}$ seconden na de oerknal in omgekeerde volgorde ondergaan.

Kennis omtrent de eigenschappen van deze nieuwe fase en de fase-overgang verschaft inzicht aangaande de structuur van ons heelal. Tevens is het zeer aannemelijk dat zich in het binnenste van neutron-sterren door de enorme dichtheden eveneens een koude vorm van het QGP voordoet.

Sinds 1986 wordt met ultra-relativistische kern-kern-botsingen kern-materie bij zeer hoge dichtheden (10^{15} dichter dan vaste-stof) en temperaturen (10^{12} K) onderzocht. Dit gebeurt met de AGS-versneller op het BNL te Brookhaven en de SPS-versneller op het CERN te Genève.

In het CERN-experiment, dat wordt beschreven in dit proefschrift, worden botsingen van zwavel-kernen met een energie van 200 GeV per nucleon met goud-kernen (S+Au) bestudeerd. De zwavel-kernen botsen dan met een fractie gelijk aan 0.999 van de lichtsnelheid met een goud-kern in een trefplaatje.

In het zwaartepunt-systeem van de elkaar naderende kernen, zie figuur 8.1, lijken deze samengetrokken in de richting van hun voortbeweging te zijn. Dit relativistische effect leidt er toe dat "pannekoeken"van kernmaterie elkaar in de botsing doorkruisen. In de overlappings-zone bevindt zich sterk samengedrukte en verhitte kernmaterie. Iedereen die in water een luchtbel heeft zien opstijgen weet dat deze naast zijn stijgsnelheid uitdijt alnaar gelang er overdruk heerst. Eenmaal aan het oppervlak spat de bel uiteen. De bel van kernmaterie is echter niet isotroop maar sterk in de bundelrichting samengedrukt. De kernmaterie zal hoofdzakelijk in deze richting expanderen. Tijdens de expansie koelt de bel af onder de vorming en uitzending van deeltjes. Uiteindelijk valt de afgekoelde en ijlere kernmaterie uiteen.

In de botsing kan de QGP-fase bereikt worden of een verhitte vorm van de kernmaterie, het hadron-gas. De QGP-fase heeft echter in de omzetting van zijn quark-gluon vrijheidsgraden, o.a. het mengen van kleur, naar die van de hadronen in het hadron-gas relatief veel tijd nodig. Dit zal zich uiten in een langere expansie-tijd en dus ook in een groter volume.

Door de vrijkomende deeltjes uit de botsingszone te meten kan de fasetoestand van de in de botsing gecreëerde dichte en hete materie afgeleid worden. Met name het bepalen van het volume en de expansietijd van de botsingszone is hierbij van groot belang en is het voornaamste onderwerp van dit proefschrift. Hiertoe wordt de intensiteits-interferometrie aangewend. De correlatie van de relatieve impulsen (snelheden) van identieke pion-deeltjes, welke uit twee quarks bestaan, levert de ruimte-tijds-verdeling van de deeltjes emitterende botsingszone. Door de correlatie-functie in verschillende componenten van de relatieve impuls te bestuderen kan men met deze "pion-microscoop"een meetlat in diverse richtingen van de botsingszone leggen.

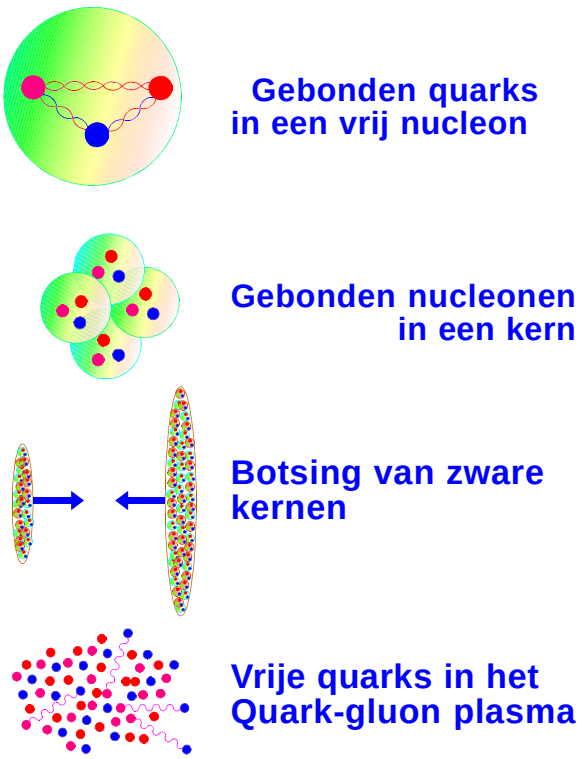

Figuur 8.1: *Vorming van het quark-gluon plasma door middel van kern-kern botsingen.*

Bij een botsing tussen twee auto's zijn het verloop en de richting waarin de brokstukken zich verspreiden eenvoudig met een camera te registreren. Voor kern-kern-botsingen met een tijdsduur in de orde van 10^{-23} seconden en een grootte van zo'n 10^{-15} meter zijn andere experimentele technieken nodig om een beeld te vormen van het gebeurde. In het WA93 experiment is hiertoe een spectrometer voor negatief geladen deeltjes geïmplementeerd. In analogie met de werking van een prisma, welke licht in zijn verschillende componenten scheidt, kunnen het aantal en de impulsen van negatief geladen deeltjes bepaald worden.

De kern-kern botsingen zijn voor de data-analyse, afhankelijk van de grootte van de overlap-zone van de botsing, in klassen verdeeld. Drie klassen zijn onderzocht: schampende botsingen (perifeer), botsingen met aan-

zienlijke overlap (semi-centraal) en botsingen waarbij alle zwavel-nucleonen betrokken zijn (centraal). Bij het vergelijken van perifere-, semi-centrale- en centrale botsingen blijken de deeltjes-multipliciteit en de gemeten stralen als functie van de centraliteit toe te nemen. Dit is in overeenstemming met een eenvoudig geometrisch model waar bij grote overlap het aantal nucleon-nucleon botsingen, en dus deeltjes productie, en het gebied van geëxciteerde kernmaterie groter wordt.

Bij het onderzoek van de transversale impulsen, dat wil zeggen snelheden loodrecht op de bundel-richting, doet zich een interessant fenomeen voor. Het aantal geproduceerde deeltjes neemt voor impulsen onder de 0.2 GeV/c voor alle drie de klassen sterk toe. Dit gedrag laat zich waarschijnlijk verklaren door het verval van nucleon en meson resonanties zoals de Δ, ω, η, etc. en duidt op een grote mate van afremming in de kern-kern-botsingen. Een dergelijke afremming is een voorwaarde voor het creëren van hete en dichte materie. Boven de 0.2 GeV/c blijkt de helling, ook wel geïnterpreteerd als de bovenlimiet van de temperatuur (T), licht toe te nemen van $T = 212 \pm 3$ MeV tot $T = 220 \pm 3$ MeV. De door de intensiteits-interferometrie methode gemeten groottes van de botsings-zones zijn ook als functie van de transversale-impulsen van de gecorreleerde pion-deeltjes onderzocht. Deze analyse verschaft informatie over de expansie van de botsings-zone. In de vroege fase zendt het systeem overwegend deeltjes met een hogere transversale impuls uit dan in een latere geëxpandeerde koelere fase. Aan de hand van een model voor longitudinale expansie leveren de metingen een expansie-tijd van zo'n $\tau = 4.0 \cdot 10^{-23}$ seconden op met een emissie-tijd $\Delta\tau \ll 2 \cdot 10^{-23}$ seconden van de negatief geladen deeltjes. Beide waarden sluiten een eerste-orde fase overgang in de S+Au botsingen uit. Echter de berekende initiële energiedichtheid $\epsilon = 1.5$ GeV/fm^3 geeft een indicatie dat een heet en dicht hadron-gas op de grens met de QGP fase is gemeten. De energie van de zwavel-kernen is blijkbaar nog niet hoog genoeg om in de kern-kern-botsing de critische energiedichtheid te overschrijden.

Toekomstige experimenten met verfijndere opstellingen en hogere bundel-energieën hebben de mogelijkheid om in het gebied van grotere energie-dichtheden te meten. De QGP fase komt dan mogelijk in zicht !

Dankwoord

Uit het gepresenteerde in dit proefschrift moge duidelijk zijn dat zulks het werk is van velen. De WA93-collaboratie bestaat uit een samenwerkingsverband van instituten afkomstig uit India (VECC Calcutta, Univ. Jammu, Univ. Panjab, Univ. Rajasthan), Polen (Warschau), Rusland (Kurchatov), Duitsland (GSI, Univ. Münster), Amerika (Oak Ridge, Univ. Tennessee), Zweden (Univ. Lund), Zwitserland (Univ. Genève, CERN) en Nederland (Univ. Utrecht, KVI Groningen).

I will treasure the nice time I had with this big "family" at CERN during the experiments. The experiences of running (night-)shifts, the working on the new PAD-chamber day and night, and the evenings in the CERN canteen (especially the food) and the old town of Geneva were great.

I especially appreciate the co-operation with my Swedish and Swiss colleagues on the "Charged Particle Spectrometer". Both my stays at the University of Lund for data-analysis and Pad-chamber development, and at the University of Geneva for building of the Pad-chamber, I regard as pleasant and fruitful.

The companionship and frankness of my Swedish colleagues, Anders Eklund, Johan Idh, Anders Oskarsson, Joakim Nystrand, Evert Stenlund, Kaj Söderstrom, Sten Garpman, Sven Lundborg, Hans-Åke Gustafsson and Ingvar Otterlund, and my Swiss colleagues, Nick Solomey, Juan Rubio, Jean-Pierre Naef, Aris Angelis, Laurent Rosselet, and Michel Martin, meant a lot to me. I hope I didn't forget to mention anyone of you !

Terug op het KVI waren de faciliteiten en ondersteuning dusdanig goed dat ik in alle rust aan de data-analyse kon werken. Hierbij dank ik tevens Nick van Eindhoven van de Universiteit Utrecht voor zijn hulp bij de analysesoftware en open discussies over de fysica.

De goede sfeer tussen de OIO's op het KVI zorgde ervoor dat ik de overgang van het "Westen"naar het "hoge Noorden"niet als een discontinuïteit ervoer. Verder zorgden de uitstekende sportvoorzieningen op de ACLO van de RUG ervoor dat zowel lichaam als geest na een dag ploeteren weer tegen

een stootje konden.

De zware-ionen groep, in het bijzonder mijn promotoren Herbert Löhner en Rolf Siemssen, dank ik voor de vele nuttige adviezen en correcties. Frequente verblijven op het CERN en de Universiteit van Lund en het bezoeken van internationale conferenties, QM'93 Borlänge Zweden, Vuosaari Finland and QM'95 Monterey USA, gaven mij een goed beeld van het voor mij nieuwe vakgebied. De overgang van het vakgebied van de NMR naar dat van de relativistische zware-ionen botsingen werd hierdoor aanzienlijk vergemakkelijkt. In het bijzonder wil ik benadrukken dat ik de computer-tips en sociale betrokkenheid van mijn "room-mate"John van Pol zeer op prijs stelde.

Mijn familie, in het bijzonder mijn ouders, mijn broer Roger en schoonzus "Juul", en mijn vrienden dank ik voor hun interesse en steun op afstand of van dichtbij. Mijn ouders kan ik daarbij niet genoeg bedanken. Jullie hebben mij de mogelijkheid en de ruimte gegeven mijn eigen weg te gaan. Menigeen kan jaloers zijn op ouders met zulk een visie. Pa en Ma bedankt !

Last but not least heb jij, Hella, mij het afgelopen jaar het geluk en het vertrouwen gegeven om samen nieuwe uitdagingen aan te gaan. Lieve Hella bedankt !

Groningen, augustus 1995, Sander